

Accepted for ApJS August 2004, v153 issue.

W49A North - Global or Local or No Collapse?

John A. Williams¹

Physics Department, Albion College, Albion, MI 49224

jwilliams@albion.edu

Hélène R. Dickey

Department of Astronomy, University of Illinois, 103 Astronomy Building, 1002 West Green Street, Urbana, IL 61801

lanie@astro.uiuc.edu

and

Lawrence H. Auer

Earth and Environmental Sciences 5, Los Alamos National Laboratory, MS-F665, Los Alamos, NM 87545

lhainnm@mindspring.com

ABSTRACT

We attempt to fit observations with 5" resolution of the J=2-1 transition of CS in the directions of H II regions A, B, and G of W49A North as well as observations with 20" resolution of the J=2-1, 3-2, 5-4, and 7-6 transitions in the directions of H II regions A and G by using radiative transfer calculations. These calculations predict the intensity profiles resulting from several spherical clouds along the line of sight. We consider three models: global collapse of a very large (5 pc radius) cloud, localized collapse from smaller (1 pc) clouds around individual H II regions, and multiple, static clouds. For all three models we can find combinations of parameters that reproduce the CS profiles reasonably

¹Department of Astronomy, University of Illinois, 103 Astronomy Building, 1002 West Green Street, Urbana, IL 61801

well provided that the component clouds have a core-envelope structure with a temperature gradient. Cores with high temperature and high molecular hydrogen density are needed to match the higher transitions (e.g. $J=7-6$) observed towards A and G. The lower temperature, low density gas needed to create the inverse P-Cygni profile seen in the CS $J=2-1$ line (with $5''$ beam) towards H II region G arises from different components in the 3 models. The infalling envelope of cloud G plus cloud B creates the absorption in global collapse, cloud B is responsible in local collapse, and a separate cloud, G', is needed in the case of many static clouds. The exact nature of the velocity field in the envelopes for the case of local collapse is not important as long as it is in the range of 1 to 5 km s^{-1} for a turbulent velocity of about 6 km s^{-1} . High resolution observations of the $J=1-0$ and $5-4$ transitions of CS and C^{34}S may distinguish between these three models. Modeling existing observations of HCO^+ and C^{18}O does not allow one to distinguish between the three models but does indicate the existence of a bipolar outflow.

Subject headings: ISM: H II regions — ISM: individual (W49A) ISM: molecules — radiative transfer

1. INTRODUCTION

W49A North is a giant H II-molecular cloud complex at a distance of 11.4 kpc (Gwinn et al. 1992)¹. One of the earliest observations and models of W49A was made by (Mufson & Liszt 1977). Although they do not distinguish between W49A North and W49A South, their figures 3 and 4 indicate the emission they observed came mainly from W49A North. With resolutions of $1'$ to $2'$, they detected an H II region in the H76 alpha line at about 8 km s^{-1} and molecular clouds in the 2 cm line of formaldehyde at 4 km s^{-1} and 12 km s^{-1} with respect to the local standard of rest. Because the formaldehyde observations indicated that the H II region is seen through the higher-velocity cloud, their picture is of an H II region between two molecular clouds with the one on the near side of the H II region moving away from us at 12 km s^{-1} and the one on the far side moving away at 4 km s^{-1} .

Welch et al. (1987) detected what appeared to be a ring of H II regions² seen obliquely in the radio continuum emission at 6 cm. Their observations with the Hat Creek mm-array of

¹Gwinn et al. refer to W49A North as W49N.

²High resolution images and nomenclature of the H II regions A through M in this “ring” of H II regions of W49A North are given by Dreher et al. (1984) and Dickel & Goss (1990) and by de Pree et al. (2000)

the $J=1-0$ transition of HCO^+ with a 7 arcsecond beam centered on the 3-mm continuum maximum showed absorption of the continuum emission on the high velocity side of the profile which they interpreted as due to collapse motion of gas toward a central mass. This was their primary argument against the earlier two-cloud interpretation of double emission peaks seen in the $J=1-0$ lines of CO (e.g. Scoville & Solomon (1973), Mufson & Liszt (1977), and Miyawaki et al. (1986)).

On the basis of observations of several transitions of CS with 12 to 20 arcsecond beams, Serabyn et al. (1993) argue that the double peaks can not be due to self-absorption because their observations of C^{34}S show the peaks in lines that should not be saturated because the terrestrial abundance of ^{34}S is 23 times smaller than the abundance of the ordinary isotope, ^{32}S . They also argue that the emission at low velocity (near 4 km s^{-1}) and absorption at high velocity (near 12 km s^{-1}) seen towards the H II region G are due to separate molecular clouds, not the collapse of one cloud as Welch et al. proposed, because the CS emission from the 12 km s^{-1} gas is seen over a large part of the field and stays at 12 km s^{-1} rather than dropping to, e.g., 8 km s^{-1} at the edges. Serabyn et al. suggest that the two clouds are colliding, and the collision has triggered enhanced O-star formation.

Dickel & Auer (1994) using a multi-level, non-LTE radiative transfer code found that a large-scale free-fall collapse reproduced the $\text{HCO}^+ J=1-0$ inverse P-Cygni profile observed with $7''$ resolution toward H II region G and the $J=3-2$ profiles observed with $24''$ resolution at locations both towards and away from G.

Keto et al. (1991), using a hydrodynamic simulation of gravitational fragmentation, concluded that Welch et al.'s “ring of H II regions” may have formed in the gravitational fragmentation of a flattened, rotating molecular cloud. In contrast to a global collapse, Keto et al. say that the double-peaked emission lines and absorption lines and even the inverse P-Cygni profiles are indicative of localized accretion flows in individual star-forming fragments.

We undertook the present study to see if we could find a way to distinguish between these competing models: multiple static clouds, global collapse, or local collapse, using the radiative transfer code of Dickel & Auer and observations with the Berkeley-Illinois-Maryland-Association (BIMA) array of the CS $J=2-1$ transition with a 5 arcsecond beam (Dickel et al. 1999, paper 1) together with the lower-resolution observations of Serabyn et al.

for their subcomponents.

2. TOOLS

We used two Fortran programs, *rt* and *mc*, to create model molecular clouds and to compare intensity profiles one would observe from them with observations. The multi-level, non-LTE radiative transfer code, *rt*, which is based on an accelerated lambda iteration method is described in the appendix of Dickel & Auer (1994). It assumes spherical symmetry in the cloud, but the variation of density, molecular abundance, velocity, and other parameters with radial distance is arbitrary. The program automatically handles regions where there is a transition to or from population inversions. The program creates files of emergent intensity and optical depth as functions of impact parameter, velocity, and transition.

These files are used by the display program, *mc*. This program (described more fully in the Appendix) assumes that the radiation from one cloud does not affect the populations of the energy levels in another cloud, so each cloud just attenuates the radiation from clouds behind it and adds its own contribution to the intensity. The validity of this assumption is discussed in the Appendix. For each cloud the user specifies the velocity with respect to the local standard of rest, the offset on the sky from some origin, and the relative position along the line of sight. The number of clouds that can be included is limited only by the size of the memory of the computer and the patience of the user. The outputs include a graphical display for the Tektronics window under X Windows, a file with a postscript version of the display, a log file with information about the display and the rms difference between the model profile and the observed profile, and a file with the computed profiles.

3. OBSERVATIONS

We used observations of several transitions of the CS molecule in the directions of H II regions A and G and in the direction of the central cloud of Serabyn et al. (1993). The data consist of observations of the $J=2-1$ transition of CS convolved to $5''$ resolution in the directions of H II regions A, B, and G with the Berkeley-Illinois-Maryland-Association (BIMA) array. Those in the directions of A and G were also convolved to $20''$ to compare with the Serabyn et al. observations. The intensities as a function of velocity for the CS emission from the $J=3-2$, $5-4$, and $7-6$ transitions of CS observed with $20''$ resolution in the directions of Serabyn et al.'s central clump and southwestern clump were read from Figure 2 of their paper. The BIMA observations are described more fully in paper 1.

There are a number of features that models of the complex should reproduce. Serabyn et al. saw an extended region of CS emission elongated from southwest to northeast with a velocity gradient which they interpreted as three partially overlapping clumps. When

convolved to the same resolution ($12''$ – $20''$), the BIMA observations of the $J=2-1$ CS line show the same features. At higher resolution ($5''$) we see inverse P-Cygni profiles at G and a “C” shape in P–V plots through G. These features are not seen at lower resolution. We consider only the southwestern and central clumps in Serabyn et al.’s model. There are a number of H II regions in the complex. We consider H II regions A, B, and G which are near the southwest and center of the complex, and attempt to reproduce the observed CS profiles and line strengths in these directions. In the high resolution CS $J=2-1$ spectra where the continuum emission has not been removed (Figure 10a of paper 1), the profiles in the directions of A, B, and G have similar intensities between 10 and 20 km s^{-1} .

We converted the observed brightness temperatures $T_B(\text{K})$ to intensities I ($\text{ergs s}^{-1} \text{cm}^{-1} \text{Hz}^{-1} \text{ster}^{-1}$) when displaying the observed and theoretical line profiles. The relationship between $T_B(\text{K})$ and $I(\text{cgs})$ is given by:

$$T_B(\text{K}) = \frac{c^2}{(2k\nu^2)} 10^{14} I(\text{cgs}) = C(\nu) 10^{14} I(\text{cgs}) \quad (1)$$

where c is the velocity of light, k is Planck’s constant, and ν is the frequency in Hz. The values of $C(\nu)$ are given in Table 1 for the observed transitions of CS and C³⁴S.

4. PROCEDURE

4.1. Overall Strategy

The overall strategy was to start with each of the three models mentioned above, multiple static clouds, global collapse, and localized collapse, using the parameters suggested by their proponents. The sizes of the H II regions came from Dreher et al. (1984). The electron densities in the H II regions were adjusted to make the continuum levels predicted by the models fit the observed levels. The cloud densities, velocities, turbulent velocities, molecular abundances, and sizes were then adjusted to fit all the observed line profiles as well as possible. The fit was judged both by eye and by the rms differences between the model profiles and the observed profiles. Then additional clouds were added as seemed indicated by the observations. Finally we relaxed the assumption of uniform conditions within the clouds.

4.2. Techniques and Insights

4.2.1. Effects of Changes in Basic Parameters

This section will summarize the effects on a spectral profile of changes in the basic parameters of a model cloud with an H II region at its center.

Section 5.3.2 of Dickel & Auer (1994) describes using the observed continuum level to fix the electron density in the central H II region of the cloud. We followed the same procedure.

For an optically thin gas which is collisionally excited, the emission should scale with the square of the volume density (particles cm^{-3}). Figure 4 and sections 6.1 and 6.2 of Dickel & Auer (1994) illustrate the effects of varying the volume density of molecular hydrogen and the relative abundance of HCO^+ for the $J=0-1$ and $3-2$ transitions. The figure shows that the strength of the line increases with increasing molecular abundance for both transitions. It also shows that the higher transition is much more sensitive to the molecular hydrogen density than is the lower transition.

As is well known, motion of the molecules due to thermal motion, turbulence, and gradients in outflows or inflows broaden the lines. We combine thermal and non-thermal turbulent motion into a microturbulent velocity. The effects of gradients in inflows and outflows is discussed in section 5.3.3 of Dickel & Auer (1994) in the case where the line of sight goes through the center of a cloud that shows a P-Cygni or inverse P-Cygni profile in one of the transitions. Their Figure 3 relates conditions in the clouds to intensities in the line profiles for velocity fields representing free-fall and homologous collapse.

Our tests show that the behavior of lines from the CS molecule is similar to the behavior of HCO^+ lines. Most of the CS transitions in our clouds are optically thin. However, the gas becomes optically thick in the $J=5-4$ and $J=7-6$ transitions for cloud A and in the gas causing the absorption in the $J=2-1$ line – which is cloud G' in the multi-cloud model, cloud B in the local collapse model, and cloud B and the envelope of cloud G in the global collapse model.

The brightness temperature of the emission is the product of the excitation temperature and $1 - e^{-\tau}$ where τ is the optical depth of the transition. As the optical depth increases, the brightness temperature approaches the excitation temperature. The excitation temperature of a transition depends on the kinetic temperature, the density of colliders (hydrogen molecules) and the energy, E_u , of the upper level. The “equivalent temperature” in kelvins is E_u/k , where k is the Boltzmann constant. When the kinetic temperature is below the equivalent temperature of a level, then only a small fraction of the collisions have enough

energy to populate the level, so very high densities are needed. The $J=2$ level of CS is easy to excite because its equivalent temperature is only 7K whereas the $J=7$ level with an equivalent temperature of 66K is much harder to excite. The “critical density” is the density for which the levels become thermalized, i.e. the excitation temperature equals the kinetic temperature (Irvine et al. 1987). For kinetic temperatures between 50K and 100K, this occurs at H_2 densities, $n(H_2)$, of $4.2 \times 10^5 \text{ cm}^{-3}$ for the $J=2-1$ transition and $2.0 \times 10^7 \text{ cm}^{-3}$ for the $J=7-6$ transition. If the levels are subthermal and the overpopulation of the upper level is small, then any variation in the background radiation field is amplified by the same factor and is relatively small, i.e. the emergent intensity is linearly proportional to the background kinetic temperature. If the populations become strongly inverted, then there is exponential amplification and comparatively small changes in the negative optical depth will result in exponentially larger variation in the emergent intensity. In the outer parts of most of our model clouds, the CS is subthermally excited, but in the central parts, the lower CS levels are thermalized and in some cases become suprathermal. For some models, there is a small range of radii where the populations of the lowest levels are inverted and weak masering occurs in the CS $J=1-0$ transition.

The emission can be further enhanced when the opacity is high enough to trap a significant fraction of the radiation. In this case photons are available to excite the molecules causing the excitation temperatures to be higher than with collisions alone. We found evidence of this radiative trapping when we put a lower density envelope around a cloud (section 5.1.2) and when we replaced a cloud with a smaller, denser core surrounded by a larger, infalling envelope (section 5.3); the results were a somewhat flatter and broader distribution of the maximum optical depths of transitions as a function of the value of J of the upper level and excitation temperatures which did not decline as steeply with J .

Increasing the kinetic temperature enhances the emission in lines from the higher-energy transitions at the expense of lower-energy transitions, similar to increases in the density, but changes in the density are more effective because the range of reasonable densities ($10^3 - 10^7 \text{ cm}^{-3}$) is much larger than the range of reasonable kinetic temperatures (10 – 100K). Because temperature is generally less effective, a constant value of 50K was used for the initial calculations. Later we relaxed this constraint because the temperatures of the interior parts of the clouds could be several hundred degrees (Doty & Neufeld 1997) and higher temperatures help the models fit the higher energy transitions, especially the $J=7-6$ transition whose upper level has a higher equivalent temperature than the 50K used in the initial calculations.

4.2.2. Effects of More than One Cloud

When more than one cloud is present along the line of sight, the combination of the contributions from the separate clouds can make it difficult to determine the characteristics of the individual clouds. For example, it is difficult to separate the effects of turbulent velocity and the relative velocities of the clouds when two (or more) clouds contribute to a line profile. The solid line in Figure 1a shows the profile of the $J=3-2$ transition of CS in the direction of H II region A that would be produced by just clouds A and G of the multi-cloud model (discussed below in section 5.1). The dashed line in that figure is the profile if the turbulent velocity in each cloud is increased by 50%, to 9.0 km s^{-1} . In Figure 1b, the solid line is the same as before, but the dashed line now shows the effect of changing the relative speed between the two clouds. The turbulent velocity remains fixed (at 6.0 km s^{-1} , same as for the solid line), but the relative speed between the two clouds has almost doubled (4.8 to 8.8 km s^{-1}). The FWHM of the two dashed curves are the same and the heights are nearly the same. The profile where the turbulent velocities have been increased is narrower at the top and broader at the base than the profile due to the moving clouds, but the differences are rather subtle.

When more than one cloud is present, it is sometimes useful to set the velocities of the clouds to very different values to see what the contribution of each cloud is to a given profile. Figure 1c shows the $5''$, CS $J=2-1$ profile in the direction of H II region B in the preliminary multi-cloud model. In this figure the velocity of the cloud at A has been subtracted from each of the cloud velocities. Figure 1d shows the effects at B of the four clouds artificially separated in velocity that contribute to the profile. In this figure the velocity of cloud A has been subtracted from each of the clouds and then 30 km s^{-1} has been added to the cloud G', 60 km s^{-1} to G, and 90 km s^{-1} to A'. It is apparent from these figures that A contributes to the right part of the profile, G to the left, G' reduces the right-hand part, and A' produces the shoulder on the right.

4.2.3. Limitations

Although the tools used for this analysis assume locally spherically symmetric flow, we can treat multiple such volumes. However, true 3-D flow, bipolar outflows, and disk rotation cannot be modeled by the these tools.

5. MODELS

5.1. Colliding Clouds → Multi-cloud Model

5.1.1. Initial Model of Two Colliding Clumps

We started with the colliding clouds model because some of the individual clouds developed for this model are used in the other models. This model evolved into a multi-cloud model. Serabyn et al. (1993) proposed a model consisting of three dense clumps. We consider their central clump near H II region G and their southwestern clump centered on H II region A. When we tried the parameters for the clumps given by Serabyn et al., the model line strengths were much larger than observed. We ran a number of cases and found a set of parameters which lead to profiles that match the line strengths and shapes of the lines rather well except the predicted strengths of the $J=7-6$ lines at $20''$ in the directions of A and G are too weak (Figure 2a, 2b), the model does not produce the absorption observed on the high-velocity side of the $J=2-1$ profile towards G in the $5''$ BIMA observations (Fig 2d), and the predicted strengths of the $J=2-1$ lines at $20''$ in the directions of A and G are too weak (Figure 2e). The $7-6$ transition will play a critical role in deciding which models are acceptable.

5.1.2. Two Dense Clumps and a Low-density Envelope Around One of Them

We tried adding a low-density envelope to the uniform cloud (clump) around H II region A. This envelope does not change the fit to the $J=2-1$ profile at A, but it does produce absorption at G, and the absorption is on the high-velocity side of the profile due to the relative motion of the clouds. However, the velocity at which the absorption appears is not high enough, and the strength of the emission in the direction of G is too low (Figure 3a, b). This model does produce a stronger $J=7-6$ line in the direction of A (Figure 3c) and line shapes that match the observed profiles of other transitions better than the models without an envelope around A. The increase in strength of the $J=7-6$ line is due to line blanketing of the envelope causing an increase in the excitation temperature for that line inside the clump.

5.1.3. Add More Clouds

We then tried a separate cloud, G' in Figure 12a, behind A (so as not to cause absorption in the profile towards A), but in front of G to produce the absorption observed on the high

velocity side of the $J=2-1$ profile at $5''$ in the direction of G. Figure 4 shows that the attempt was successful. The profiles match well except for the $J=2-1$ transition at $20''$ and the $J=7-6$ transition. To increase the $J=2-1$ emission in a $20''$ beam, we increased the sizes of the clouds at A and G and reduced the molecular abundance to compensate for the increased path length, see Figure 5. We also looked at the $J=2-1$ profile in the direction of H II region B and found that the CS emission from the clouds at A and G fully accounted for the CS emission observed at B. The final change we made at this stage was to add a cloud, A' in Figure 12a, at the relatively high velocity of 17 km s^{-1} behind the whole complex to account for the shoulder observed on the high velocity side of the profile at A, see Figure 6 and Table 2. All the model profiles match the observed ones except $J=7-6$ which are lower than observed. All of the clouds in this model are uniform. We call this model the preliminary multi-cloud model because, as we show below, clouds with non-uniform temperatures and densities give profiles that match the observations better.

5.1.4. Comparison with Other Results

We find considerably lower H_2 densities than Serabyn et al. (1993), but our $[\text{CS}]/[\text{H}_2]$ ratios are similar to those found by them and by others. Serabyn et al. found the molecular hydrogen density to be $6 \times 10^6 \text{ cm}^{-3}$ in their central clump and $3 \times 10^6 \text{ cm}^{-3}$ in the southwestern clump. We find densities a little larger than $1 \times 10^6 \text{ cm}^{-3}$ for our clouds corresponding to these clumps. Serabyn et al. use a ratio of $[\text{CS}]/[\text{H}_2]$ (per km s^{-1}) of 3.6×10^{-10} for both clumps. We find ratios of 5.1×10^{-11} for the cloud corresponding to the central clump and 2.6×10^{-10} for the southwestern one, and we find a turbulent velocity of 6 km s^{-1} . Miyawaki, et al. (1986) estimate the $[\text{CS}]/[\text{H}_2]$ ratio to be less than or equal to 5×10^{-10} .

Although the H_2 densities of our clumps are lower than Serabyn's values, the size of cloud G is larger, resulting in a much larger mass for it. Serabyn et al. find masses for the clumps of 3×10^4 to 6×10^4 solar masses and a total cloud core mass of about $1.0 \times 10^5 \text{ M}_\odot$. Miyawaki estimated the core mass as $.5 \times 10^5 \text{ M}_\odot$ to $2.5 \times 10^5 \text{ M}_\odot$. We find cloud masses of $10.2 \times 10^5 \text{ M}_\odot$ and $0.8 \times 10^5 \text{ M}_\odot$ for the two main clouds with $11.3 \times 10^5 \text{ M}_\odot$ for the total.

The discrepancy in the H_2 densities of the clumps will be partially resolved when we discuss the core-envelope structure in section 5.3. In this case, the central H_2 densities are increased to $6 \times 10^6 \text{ cm}^{-3}$.

The $V_{l\text{sr}}$ derived for cloud G agrees with the Serabyn et al. velocity. However, we find a $V_{l\text{sr}}$ of about 9 km s^{-1} rather than 11.5 km s^{-1} works best for cloud A with additional, lower-density gas at $V_{l\text{sr}}$ of 13 km s^{-1} and possibly also at 17 km s^{-1} .

5.2. Global Collapse

We next considered a model using the parameters of a cloud in free-fall collapse around H II region G from Dickel & Auer (1994). We were able to reproduce our 5" beam CS J=2–1 observations by using a $[\text{CS}]/[\text{H}_2]$ ratio of 4.5×10^{-10} . We added the cloud at A and the H II region at B from the multi-cloud model. The fit to the observed 5" J=2–1 observations is satisfactory in the directions of H II regions A, B, and G; however, the model profiles are too weak for the 20" J=5–4 and 7–6 observations. See Figure 7.

5.3. Localized Collapse

The third set of models we considered consisted of in-falling clouds around each of the H II regions. This model was proposed by Keto et al. (1991) as a result of their analysis of the fragmentation of a rotating disk. Our model went through several forms before arriving at one that matched the observations. We first considered uniform-temperature, in-falling clouds around each of the H II regions A, B, and G. This model was able to match the 5" J=2–1 emission peaks in the directions of A and G, but the absorption on the high-velocity side of the profile at G was not as deep as observed, and there was too much emission in the direction of B. The emission at 20" resolution was not as strong as observed in any of the transitions.

We next considered clouds in free-fall around each of the H II regions. The model 5" J=2–1 profiles matched the observed profiles rather well, but all the 20" profiles were much weaker than observed. We then put a uniform cloud around each H II region inside the free-falling cloud. All the model profiles matched the observed ones with three exceptions. The 5" J=2–1 profile in the direction of B was a little strong and not the right shape and the 20" J=2–1 profiles in the directions of A and G were too weak. Increasing the size of the cloud at A improved the fit of the 20" J=2–1 profiles. Increasing the size of the cloud at G did not help this fit. Adding a small, uniform, low-density cloud in front of B, cloud B' in Figure 12b, moving at almost the speed of A improves the fit with the observed profile at B by absorbing some of the emission in that direction. Physically, this material might be associated with A. The 20" J=2–1 profiles are still a little weak, but the match of the model profiles to the observed ones is good for all the rest. See Figure 8.

The local collapse model is better at matching the J=7–6 line than either the multi-cloud or global collapse models. This is most likely due to the introduction of a core-envelope structure in cloud components for A and G. These clouds in the local collapse model have an 80% smaller core with a density about 5 times higher than in the multi-cloud case and

this core is surrounded by an extensive lower density envelope. As a result of these changes, the highest optical depth in the $J=7-6$ line has increased by about 25% in both clouds. The excitation temperature of the $J=7-6$ line is about 16K throughout the clouds for the multi-cloud model and in the envelopes for the local collapse model. However, in the local collapse model, the excitation temperature rises to 35K in the center of the core for cloud A and to 70K in the center of the core for cloud G. The overall higher optical depths and excitation temperatures create the higher brightness temperatures needed to fit the observed intensity of the $J=7-6$ line.

6. MODIFICATIONS TO PRELIMINARY MODELS

6.1. The Preliminary Models and the $J=7-6$ Emission

The major deficiency of the preliminary models is the weakness of the $J=7-6$ profiles for the multi-cloud and global collapse models. Two changes come to mind that may allow these models to reproduce this transition: First, a higher kinetic temperature, perhaps with a gradient, so that there would be higher temperatures in the central regions where the density is high. Second, a core-envelope structure which seems to have done the trick for the local collapse case and which was hinted at already in the two-clump model with an envelope around clump A.

6.2. Exploration of Temperature Laws

We know from the 20 micron emission peak just north of the H II region G that there is hot dust in the central part of W49 (Ward-Thompson et al. 1992). The physical conditions in such a situation have been described in a review article (Evans 1999). The main effect for our study, is that near H II regions where the molecular hydrogen density is high, the gas temperature will be comparable to the dust temperature because of collisions. Therefore, the kinetic temperature could reach several hundred degrees in the very center but fall off further out where the dust is less opaque. Typically the temperature would decrease as $r^{-0.4}$ (Doty & Neufeld 1997; Evans 2000).

To see the effects on the profiles of variations in the temperature, we modified the preliminary models as follows: 1) changed the kinetic temperature from the constant 50K of the preliminary models to a constant 100K, 2) introduced a radial decrease in the temperature of $r^{-0.4}$ from a high of 100K at the center, and 3) same as case 2 but with T=200K at the center. For each of these temperature structures we spread out the cloud components in

velocity space (similar to what was done in section 4.2.2 Fig. 1c) to see which components contributed most to the emission along the different lines of sight. For the core-envelope infall model, we separated the dense, uniform, turbulent, hot core with no in-falling motions from the lower density, lower temperature, collapsing envelope by giving each component its own offset in velocity.

6.2.1. *multi-cloud model*

As expected, increasing the temperature from 50K to 100K increases the strength of the $J=7-6$ line so that it is a little stronger than is observed, and the profiles for the $J=2-1$ transition are unchanged. However, the $J=5-4$ line is now much too strong. With a radial gradient in the temperature from a high of 100K at the center, the $J=7-6$ and $J=5-4$ lines are too weak. They are weaker than when the temperature was a constant 50K. Increasing the central temperature to 200K with a radial gradient causes the $J=5-4$ line to match the observations, but the $J=7-6$ line is much too weak.

6.2.2. *global collapse model*

The effects on line profiles of changing the temperature structure in the global collapse model are similar to those in the multi-cloud model. While increasing the temperature to 100K strengthens the higher-level transitions, the $J=7-6$ line is still too weak. Adding a gradient in the temperature causes the $J=7-6$ and 5-4 lines to be much weaker than is observed. The $J=7-6$ line is still too weak even if the central temperature is increased to 200K with a gradient. The $J=5-4$ line is about the right strength in the direction of A, but is too weak in the direction of G. For all of these temperature structures, almost all of the emission in the higher transitions comes from the cloud around H II region A.

6.2.3. *local collapse model*

Increasing the temperature from 50K to 100K causes the $J=7-6$ and $J=5-4$ lines to be much stronger than the observed lines. Adding a gradient in the temperature reduces the strength of these lines very nearly to what is observed. Increasing the central temperature to 200K with a gradient makes the $J=7-6$ and $J=5-4$ lines too strong. They are about as strong as when the temperature was 100K without a gradient.

6.3. Core-envelope Models

In section 5.1.2 we found that adding a low-density envelope to the uniform clump around HII region A increased the strength of the $J=7-6$ emission. Serabyn et al. (1993) also commented on the likelihood of the clumps being immersed in lower-density gas. We now consider clouds having a static, turbulent core with free-fall in the surrounding volume. Adding such a core-envelope structure to the global collapse model causes it to reproduce the $J=7-6$ and $5-4$ transitions as well as the lower transitions. We get the best fit to the observations with an “inside-out” collapse model (Shu 1977; Shu et al. 1987). We tried three velocity structures for the local-collapse model with the 100K temperature gradient and core-envelope structure. The velocity structures were: 1) free-fall envelope with $v=-5$ km s^{-1} at the inner edge and decreasing as $r^{-0.5}$, 2) a constant in-fall velocity of -5 km s^{-1} , 3) no in-fall velocity, which is like our multi-cloud models but with a core-envelope structure. We find that the differences between the profiles predicted by these models are less than the noise in the observations.

We conclude that the core-envelope structure is the key to reproducing the strength of the $J=7-6$ line, and to some extent the $J=5-4$ line, while maintaining the good fits to the lower transitions. The temperature gradient can be adjusted to give a good fit. The requirement is that the highest temperatures be in the center where the densities are sufficient. The exact velocity gradient in the local collapse envelopes is not critical as long as it is in the range 0 to 5 km s^{-1} if the turbulent velocity is around 6 km s^{-1} .

6.4. Final Models

We arrived at our final models by adjusting the temperatures and structures of our preliminary models. For the multi-cloud model we gave cloud G a core-envelope structure and made the temperature of the core 100K. For the global collapse and local collapse models, we used a core-envelope structure for both clouds A and G. The temperatures of the cores are 100K with a gradient of $r^{-0.4}$ which continues through the envelope. We also included the 17 km s^{-1} cloud from the multi-cloud model behind the other clouds of the Shu global collapse and the local collapse models to account for the shoulder observed on the high velocity side of the profile at A.

The physical parameters of the final models are given in Tables 3 through 6. Table 3 gives the parameters of cloud A', which is used in all three final models, and clouds B' and B which are used in the final global collapse and local collapse models. Cloud A' was also used in the preliminary multi-cloud model. In each table the model components are listed

across the top followed by their LSR velocities. Next are the parameters of the H II regions, followed by the parameters for the components of the molecular clouds.

The profiles from the final models are displayed in Fig. 9, 10, and 11 for the multi-cloud, Shu global collapse, and local collapse models respectively. All three models reproduce the observations reasonably well except for the 20'' J=2–1 profiles in the directions of H II regions A and G. The model profiles are weaker than the observed for all three models. Figure 12 shows the clouds as they are arranged along the line of sight for the three final models.

Let us compare the similarities and differences in the excitation temperatures between the preliminary cloud models and the final core-envelope models with a temperature gradient. In both sets of models, a population inversion occurs in the lowest transition (J=1–0) in the outer parts of the cloud and the excitation temperature becomes suprathermal in the interior parts. For the other transitions, the excitation temperatures can be as low as a few degrees in the outer parts of the clouds. In the models with a temperature gradient, the kinetic temperature is 100K in the interior and declines to around 25 to 30K in the outer part of the envelope. Because of the lower kinetic temperature in the outer part of the clouds, the excitation temperatures are also lower there compared to those for the preliminary cloud models. However, both the J=2–1 and J=3–2 transitions become suprathermal in the cores with the excitation temperature exceeding 100K. For the preliminary cloud models, only in the center of cloud G does the J=2–1 transition become suprathermal (> 50K).

7. COMPARISON BETWEEN MODELS

7.1. Parameters

The parameters of the H II regions are essentially the same in the three models. The V_{lsr} for cloud A is 8 km s^{−1} for the multi-cloud model and 9 km s^{−1} for the other two. The V_{lsr} for cloud G is 4.2 km s^{−1} for all three final models. All three models have an extra cloud A' which provides emission on the high-velocity side of the 5'', J=2–1 profile in the direction of A.

The multi-cloud model has a uniform cloud for A. Cloud G has a core-envelope structure with higher temperature and density in the core, but both core and envelope are uniform. B is just an H II region, and the H II region for G is separated from the core and envelope. Cloud G' is located behind A but in front of G to provide absorption on the high-velocity side of the 5'' J=2–1 profile in the direction of G.

In the global collapse and local collapse models both clouds A and G have core-envelope structures with H II regions at their centers. The uniform cores have high temperature and density. The envelopes have lower temperatures and densities and gradients in these quantities as well as in the in-fall velocity. B has a cloud as well as an H II region. The cloud has a high CS density and gradients in the in-fall velocity, temperature, and density. Cloud B' is located behind A to absorb some of the emission in the direction of B. These models do not have cloud G'. The envelope of cloud G in the global collapse model is much larger, has a much lower density, and has a higher in-fall velocity than the envelope of cloud G in the local collapse model.

7.2. RMS Differences

Table 7 gives the ratios of the rms differences between the profiles predicted by the models and the observed profiles for the preliminary multi-cloud model and the three final models to the rms of the line-free baseline regions of the plots Figures 9 - 11. The ratios show how well the theoretical profiles match the observed compared to the observational errors. A ratio of one means that the rms of the theoretical profile is equal to the rms of the observations. Using this ratio as a figure of merit, it appears that on the average all four models fit the observations about equally well. However, there are major differences in how the errors are distributed among the transitions. All four models reproduce the $5''$ $J=2-1$ observations very well. However, the fits for the $20''$ $J=7-6$ transition are much better for the three final models than for the preliminary multi-cloud model. The poor fit for the $20''$ $J=2-1$ profiles by all three final models has already been noted; although it appears from the table that the multi-cloud and global collapse fits are better than local collapse. The fits are not very good for the $20''$ $J=3-2$ transition; however they are better for the final models than for the preliminary one. The final multi-cloud and global collapse models do a better job in the direction of G and the local collapse model does better in the direction of A for this transition. The visual impression from Figures 9-11 is that the fits for this transition are good, and in Table 7 the size of the rms differences for this transition are a little smaller than for the other transitions. The large values of the ratio are due to the rather small value of the rms of the baseline.

7.3. Deconvolutions

Figures 13, 14, and 15 show the contributions of the components of the clouds that make up the three final models to the predicted profiles. The components are separated in

velocity as in Figure 1d. The components are labeled and the velocity shifts are indicated in panels c and d of each figure. The observed profiles are also included in each panel. For each of the models, the cores of clouds A and G produce the $J=7-6$ line. The major differences come in the $5''$ $J=2-1$ profiles in the directions of G and B as described below.

First consider the contributions of the clouds to the emission and absorption observed towards G. In the multi-cloud model cloud A produces a major part of the emission with additional contributions from A' and the core and envelope of cloud G, while G' produces the absorption. In the Shu global collapse model, the core of cloud G produces the major part of the emission with contributions from A' and the core of cloud A. The envelope of cloud G and cloud B produce the absorption. In the local collapse model, the cores of clouds A and G contribute equally to the emission, and cloud A' also contributes significantly. Cloud B produces the absorption.

Now consider the contributions of the clouds to the emission and absorption observed towards B. In the multi-cloud model cloud A produces a major part of the emission with additional contributions from A' and the core and envelope of cloud G, while G' produces the absorption. In the Shu global collapse model, the core of cloud A is the major contributor to the emission with additional contributions from the core of G and A'. The absorption is produced by B' with some contribution from B and the envelope of G. In the local collapse model, the core of cloud A is the major contributor to the emission with help from G core and A'. Cloud B' does the absorbing with help from cloud B.

7.4. Position-Velocity Plots

Position-velocity plots with the continuum subtracted for the three final models are shown in Figure 16. The left-hand panels correspond to cut a of Miyawaki et al. (1994) and the right-hand panels to their cut c. Our plots are for the $J=2-1$ transition at $5''$ resolution. They also correspond to figures 8a and 8c of paper 1 which were made with our BIMA observations along the same cuts at the original resolution of $4.6'' \times 3.8''$. H II G is close to (about $1.5''$ west and $1''$ north of) the intersection of cuts a and c. The H II regions are located within their respective clouds except in the mc model where the center of cloud G (Serabyn's central cloud) is offset $3.6''$ to east and $7.4''$ to the north of H II region G.

The contours in Figure 16 are intensities, I , in cgs units whereas the corresponding plots in Figure 8 of paper 1 are given in flux densities per beam, S^3 . The conversion between S

³The units given in Figures 6 through 9 in paper 1 are in error; the correct units are $\text{Jy beam}^{-1} \text{ km s}^{-1}$

and I may be written as follows:

$$S(Jy\ beam^{-1}) = \Omega(sr) 10^{23} I(cgs) \quad (2)$$

where $\Omega(sr)$ is the solid angle of the beam in steradians. For a gaussian beam with half-power widths, $\theta_1(")$ and $\theta_2("$), $\Omega(sr)$ may be written as

$$\Omega(sr) = 1.133 \theta_1(") \theta_2(")/(42.545 10^9) = 10^{-9} \times [0.0266 \theta_1(") \theta_2(")] = 10^{-9} \times F(\theta_1("), \theta_2(")) \quad (3)$$

Substituting this expression for $\Omega(sr)$ into equation 2, we obtain

$$S(Jy\ beam^{-1}) = 10^{14} I(cgs) F(\theta_1("), \theta_2(")) \quad (4)$$

For the CS(J=2-1) data with the original beam, $F(4.6" \times 3.8") = 0.466$ and for the convolved beam, $F(5" \times 5") = 0.666$.

The plots from all three models show the same features: strong emission near H II region A with a peak at about $8\ km\ s^{-1}$, absorption between 10 and $20\ km\ s^{-1}$ near H II region G (located close to offset 0), the emission tends to extend in the direction of the cloud G (the central cloud of Serabyn et al.) with the velocity of the peak dropping to about $4\ km\ s^{-1}$. The global collapse model contours extend to greater negative velocities (about $-15\ km\ s^{-1}$) than the other models (about $-5\ km\ s^{-1}$).

The plots agree in general with the plots made from the observations. None of the plots from the models show the northeastern cloud of Serabyn et al. because that cloud was not included in any of our models. All three models show less absorption on cuts a and c than the observations do. There are more negative contours in our plots than in paper 1 because our plots use a smaller interval between contours. The emission peak on cut a due to H II region A has about the same strength, velocity, and position as in the plot of the observations in paper 1. However, for cut c the strongest maximum is further north along the cut than the intersection of cuts a and c whereas in the observations the peak is south of the intersection. In the models the north peak is between 5 and $10\ km\ s^{-1}$ whereas in the observations it is at $10\ km\ s^{-1}$. Since the P–V plots “bow out” more to negative velocity for the global collapse model than either of the other two models in agreement with the observations, the P–V plots slightly favor the global collapse model.

in Figure 6 (same as in Figure 5) but $Jy\ beam^{-1}$ (not $Jy\ beam^{-1}\ km\ s^{-1}$) in Figures 7 to 9.

7.5. Predicted Profiles for C³⁴S

We used our three final models to predict what would be observed using transitions J=3–2, 5–4, and 7–6 of the C³⁴S molecule, and compared these predictions to the observations reported in paper 1 and by Serabyn et al. (1993). The comparisons are shown in Figure 17 for the J=3–2 transition, Figure 18 for J=5–4, and Figure 19 for J=7–6. We first tried constructing models by using C³⁴S molecular data and decreasing the CS abundance by a factor of 22 (Wilson & Rood 1994), but we found that a factor of 15 for clouds A and A' and a factor of 13 for the other clouds gave better fits to the observed profiles. The strengths of the predicted lines match the observed lines in all cases except the J=7–6 transition towards A in the multi-cloud model. The weakness of the predicted line may be because this model is the only one in which cloud A does not have the core-envelope structure which we have found is important to produce strong J=7–6 lines. We did not give cloud A this structure because the C³²S J=7–6 line from this model was only a little weaker than the observed line. In all cases the model profiles are symmetrical while some of the observed profiles show asymmetrical or double-peaked lines. These variations in the observed profiles may be due to noise, or they may indicate that the models need to include additional processes such as outflows, rotation, and clumps within an overall collapsing cloud.

7.6. The Intensity of CS Emission away from H II Regions

Figure 6 of paper 1 shows that the integrated intensity of the CS J=2–1 emission is elongated along a major axis which runs from the northeast to the southwest. The overall width of the CS emission perpendicular to the major axis at the 25% level is about 4' and the width of the CS emission for the southwestern clump near H II region A at the 50% level is 2'. Except for the very low-density envelope of cloud G in the global collapse model which extends to 3', the overlapping clouds in our various models extend to 1' or less. Therefore, it is not surprising that predicted profiles for the J=2–1 transition (with 5" beam) for positions away from G and A fall short of the observed strength of the CS emission. Generally, lines-of-sight beyond the edge of a core but within the envelope of the nearest model cloud, A or G, are located within the 25% to 50% contours of the observed integrated intensity. The intensities of the predicted J=2–1 CS profiles at such positions are 40% to 50% of the observed values. An exception is towards H II H whose projected position is just within the core of the G cloud and whose predicted intensity is 60% of the observed intensity.

We are obviously missing some components in our modeling such as any molecular gas around other H II regions (besides A, B, G), Serabyn et al.'s northeastern clump, and perhaps an extensive region of low density gas into which the envelopes of the clouds merge.

7.7. High Resolution Observations

7.7.1. CS $J=1-0$

We used the three final models to predict the profiles that would be observed in the directions of H II regions A and G in the $J=1-0$ transition at resolutions of $2''$ and $5''$. The $2''$ profiles are shown in Figure 20 and are deconvolved in Figure 21. The $5''$ profiles show the same features as the $2''$ ones. The main difference between the predictions of the three models is the depth and width of the absorption in the direction of H II region G. The absorption is much wider and deeper for the Shu global collapse model than for the other two. The absorption for the multi-cloud model is about 50% deeper than for the local collapse model. There are subtle differences in the shape of the profile in the direction of H II region A. All the models predict a peak about 17 km s^{-1} . Figure 21 indicates that this peak is due to cloud A'. The profiles also show a peak about 10 km s^{-1} which is due to cloud A in the multi-cloud model and due to cloud B' in the other two models. The predicted strength of this peak is greater than the one at 17 km s^{-1} for the Shu global collapse and local collapse models, but the peaks are about the same strength for the multi-cloud model.

7.7.2. CS $J=5-4$

We also used the models to predict the profiles in the $J=5-4$ transition of CS at $2''$ and $5''$ resolution. The $2''$ profiles are shown in Figure 22, and the profiles at $5''$ are similar. At either resolution the peak in the direction of H II region A for the multi-cloud model is only about 60% as high as for the other two models. The shapes of the profiles predicted by all three models are symmetrical and are nearly the same. Cloud A' does not contribute significantly to any of the profiles.

8. APPLICATION TO OTHER MOLECULES

Radiative transfer modeling of several transitions of CS did not allow us to clearly distinguish between the three models: multiple, static clouds; global collapse; or local collapse. Parameters could be found for each of these models such that the theoretical profiles gave a reasonable match to the observed ones. Following the referee's suggestion, we applied the final cloud models to other molecules, namely, HCO^+ and C^{18}O , to see whether either molecule could be used to discriminate between the different models. The observations of HCO^+ are from (Dickel & Auer 1994), and the observations of C^{18}O are from Dickel et al.

1999.

In applying the CS modeling results to these other molecules, the only parameter allowed to vary is the relative abundance of the target molecule; all other parameters remain fixed as given in Tables 3 to 6.

8.1. HCO^+

We first applied the radiative transfer calculations to HCO^+ because the initial conditions for the global collapse model for CS came from the earlier modeling of HCO^+ (Dickel & Auer 1994). Aside from the different relative abundance for the two molecules, the main differences between the initial and final values of the cloud parameters in the CS modeling were the higher H_2 density in the core and the lower H_2 density in the envelope of cloud G, the higher kinetic temperatures in its core, and the additional cloud around H II region A.

For these new calculations, we used the parameters of the clouds determined from CS and an initial relative abundance for HCO^+ taken from the paper by Dickel & Auer. Once a relative abundance was chosen, that value was fixed – both between clouds and throughout a given cloud. We varied this value until we got the best compromise in matching the theoretical and observed profiles for HCO^+ for the $J=1-0$ transition at $7''$ resolution towards the H II regions A and G and for the $J=3-2$ transition at $24''$ resolution towards the H II region G. The relative abundance of $[\text{HCO}^+]/[\text{H}_2]$ is low – about 10^{-13} to 10^{-12} .

Unfortunately, the predicted intensity for the $J=3-2$ transition was too high while that of the $J=1-0$ transition was too low for all of the relative abundances considered. One way to remedy this situation would be to lower the H_2 density in the core and raise it in the envelope of G, i.e. closer to what was used in the modeling by Dickel & Auer but that was not allowed in this exercise. Therefore, instead, we decreased $n(\text{HCO}^+)$ in the high density core and increased it in the low density envelope, but this change was inadequate as shown for best fit obtained for HCO^+ for the two collapse models in Figure 23 and the multi-cloud model in Figure 24 (left side).

We next considered the possibility of an error in the adopted dipole moment for HCO^+ , $\mu = 3.9$ D (Botschwina 1989). Earlier ab initio calculations by Woods et al. (1975) gave a range between 3.3 D and 4.3 D. For optically thin lines, an increase in μ from 3.9 D to 4.3 D or a factor, f , of 1.1 would increase the Einstein A transition probabilities, optical depths, and critical densities by $f^2 = 1.2$. Such an increase in the critical density for the $J=3-2$ transition would make it more difficult to excite and thus might lower its intensity while having little effect on the lower transitions. However, there was no perceptible difference between the

theoretical profiles calculated using $\mu = 4.3$ D and those run with $\mu = 3.9$ D. Lowering μ to 3.0 D lowered the intensities a little for both transitions. We conclude that changing the value of the dipole moment within reasonable limits does not improve the theoretical fits to the HCO^+ profiles.

At this point we considered what other differences between HCO^+ and CS might explain the poorer fit to the HCO^+ observations compared to the results of Dickel & Auer – for example, differences in excitation and/or where the molecules are located spatially. One such difference would be the presence of a bipolar outflow because the abundance and hence intensity of HCO^+ is often enhanced therein relative to CS. Indications that bipolar outflows may be associated with H II regions A and G1&G2 in the W 49 A North region are the fact that their continuum spectra are inverted and their recombination lines are very broad (de Pree et al. 2000) .

To investigate the effect of such an outflow on the resultant HCO^+ profiles, we added an outflow behind most of the other cloud components. Because our code is not fully three-dimensional, we attempted three approximations to the outflow: 1. an expanding molecular shell, 2. several “bullet” clouds along the line of sight towards G with velocities mimicking an outflow, and 3. a similar series of bullets centered between H II regions A and G and extending to both A and G but with the outflow at an angle to the line of sight. However, for any of these to be successful, it is necessary to lower $n(\text{HCO}^+)$ in the other cloud components by another factor of three. All these approximations to an outflow yield similar results. After expanding the calculations to C^{18}O (next section), we further modified the properties of outflow case 3. Figure 24 (right side) shows the resulting improvement in the match in the multi-cloud model when such an outflow is added. The results for the two collapse models are nearly identical to those of the multi-cloud model due to the fact that HCO^+ is so depleted in the clouds ($[\text{HCO}^+]/[\text{H}_2] \leq 10^{-13} \text{ to } 10^{-12}$) that the outflow dominates in producing the emission. We conclude that HCO^+ is no better than CS in distinguishing between multiple, static clouds and either of the collapse models.

The flexibility and ease of use of the mc program was important in being able to create a model outflow using small clouds as building blocks and varying their location both along the line of sight and in the plane of the sky.

8.2. C^{18}O

We applied the same procedure to C^{18}O and tried to fit the line profile of $J=2-1$ observed with 12'' resolution by Dickel et al. (1999) toward H II regions A and G. The intensities

and line widths are reproduced with a relative abundance, $[C^{18}O]/[H_2]$ of about 3×10^{-9} to 8 which is equivalent to $[CO]/[H_2] \approx 10^{-5}$ and $[CO]/[C^{18}O]$ between 300 and 3000. The results are shown in Figure 25 for the three models – multi-cloud, global collapse, and local collapse. Although the overall fit is good, the details of the line shape are not reproduced.

The emission from CO is prominent in outflows so we assume that $C^{18}O$ is also present there. By reducing the relative abundance of $C^{18}O$ by two-thirds in clouds A and G and then adding an outflow (above case 3 for HCO^+), we end up with a surprisingly good match to the detailed shape of the $C^{18}O$ profiles seen towards both H II regions A and G as shown in Figure 26 for all three models. The only exception is towards G in the global collapse case. These results strongly suggest that some kind of outflow is present in the region.

8.3. Nature of the possible outflow

The concocted outflow is only intended to be an approximation; more accurate modeling is obviously warranted. Nonetheless, this simple approximation both improves the HCO^+ fits and gives very good matches to the $C^{18}O$ profiles. For this outflow, we used four blobs, and each blob is about one-half the size of the core of cloud G. The other parameters of the blobs are similar to those found for the core of cloud G in the HCO^+ paper, e.g. the H_2 density is closer to 10^5 cm^{-3} rather than the $5 \times 10^6 \text{ cm}^{-3}$ found in the CS modeling. There are no velocity gradients within a blob but rather the outflow is mimicked by spreading the blobs between H II regions A and G with the least positive velocity ($+3 \text{ km s}^{-1}$) just east of G and most positive ($+13 \text{ km s}^{-1}$) towards A in the case of $C^{18}O$. The best parameters of the outflow for HCO^+ differ slightly from those for the best outflow for $C^{18}O$ in that HCO^+ requires a bit more turbulence in the blobs, and the outflow is shifted spatially and in velocity. There is additional HCO^+ in the outflow at $+1 \text{ km s}^{-1}$ somewhat further to the east of G and very little HCO^+ in the outflow at $+13 \text{ km s}^{-1}$ in the direction of A.

For HCO^+ the outflow emission dominates that from the other cloud components; whereas for $C^{18}O$ the outflow plays a less prominent role. For $C^{18}O$ the outflow may be the cause of the asymmetry in the line profiles as it explains the shift in velocity of the peak of the emission profile between the directions of the H II regions A and G.

9. ADDITIONAL STRUCTURAL INFORMATION

For our radiative transfer modeling of W49A North, we concentrated on three competing dynamical models and modified the initial parameters of the constituent clouds to get the

best fit to the CS observations. Since this investigation began, new observations have become available, mainly concerning the embedded ultracompact H II regions which 1) show that the ring of H II regions is not rotating, and 2) tend to favor a picture of dense clumps embedded in an overall collapsing cloud. The evidence is as follows:

VLA observations of NH₃ emission and absorption by Jackson & Kraemer (1994) and our BIMA observations of CS (J=2–1) (Dickel et al. 1999), both at 4'' resolution, show the “C” shape in the position-velocity diagrams which is indicative of infalling motions. A hydrogen recombination study by de Pree et al. (1997) indicates that the H II systemic velocities fall into several groupings, similar to the molecular clumps of Serabyn et al. (1993). One of their major new findings is that the systemic velocity of H II region B is more likely to be 16.5 km s^{−1} (from H52 α) rather than the earlier value of 2.5 km s^{−1} (from H92 α); note that we arrived at a systemic velocity of 15 km s^{−1} for cloud B by trial and error to obtain the best fits of CS profiles towards B. Wilner et al. (2001) observed emission from dust and from CH₃CN at 1.3 mm with the BIMA array and found both to be associated with some of the H II regions, in particular B, and the western part of G. From their analysis of very high resolution (0.045'') VLA images of the ultracompact H II regions, de Pree et al. (2000) conclude that to confine them, the H II regions must be surrounded by very high density molecular gas ($\sim 10^8$ cm^{−3}) and/or by turbulent gas. A further complexity in any modeling will be dealing with the possibility of ionized as well as bipolar outflows associated with H II regions whose continuum has an inverted spectrum (i.e. the flux density is increasing rather than decreasing with frequency) and whose recombination lines are very broad (≥ 45 km s^{−1}); the prime candidates being H II regions A, and G1 & G2.

We tend to agree with de Pree et al. (1997) who concluded from the above information that the ultracompact H II regions may be associated with and embedded within individual clumps that have fragmented within a collapsing cloud, but we must await further observations and modeling to confirm this emerging picture.

10. CONCLUSIONS

We started by trying to fit the observed 5'' J=2–1 and 20'' J=2–1, 3–2, 5–4, and 7–6 CS profiles in the direction of W49A North using three different models: colliding clouds, global collapse, and localized collapse. We modified the parameters of these models until we got the best fits we could from each model.

It is possible to find combinations of parameters for all three models that will reproduce the observations available to us except for the 20'' J=2–1 profiles observed in the direction

of H II regions A and G. The final models do not predict as much emission in these profiles as is observed. There may be an extended region of emitting gas that is not modelled by our spherical clouds.

The observations at our disposal do not constrain the models sufficiently to yield a unique solution. However, there are some features that any successful model must have: 1) H II regions at the observed locations. 2) CS in emission towards H II regions G and A. 3) CS in absorption in front of H II region G and moving towards it at the proper speed to produce the absorption seen on the high-velocity side of the profile. The absorption indicates an excitation temperature in the CS $J=2-1$ transition that is lower than the brightness temperature of the H II continuum background. This lower excitation temperature can be achieved by low H₂ density in the foreground gas. This absorption is not in front of A. The gas doing the absorbing may be in a collapsing cloud centered on H II region G or in a separate cloud moving towards H II region G. 4) Sufficient density and high temperature in the molecular clouds to give the observed strengths of the higher transitions of CS. We found that a core-envelope structure is an effective way to get the high-density region needed to reproduce higher transitions and the regions of lower density and temperature needed to reproduce lower transitions.

Our models indicate that high-resolution observations of the $J=1-0$ and $5-4$ transitions of CS may distinguish between the models. The width and depth of the absorption in $J=1-0$ towards H II region G should distinguish between the Shu global collapse model and the other two. The presence of an emission peak or bump at 17 km s⁻¹ in the profile for this transition towards A would confirm the existence of cloud A'. The relative strengths of the peaks at about 10 km s⁻¹ and 17 km s⁻¹ in the $J=1-0$ transition in the direction of A may distinguish between the multi-cloud and local collapse model and confirm the presence of cloud B'. The strength of the line towards A in the $J=5-4$ transition could distinguish between the multi-cloud model and the other two.

Our models match the intensity but not the shape of the C³⁴S profiles at 20" resolution for the $J=3-2$, $5-4$, $7-6$ transitions. The apparent asymmetry in the observed line profiles gradually shifts in velocity from the $J=3-2$ to the $J=7-6$ transition. When higher resolution observations of these optically thin transitions become possible with adequate sensitivity, they may better reveal the overall density structure in the W49A North region including whether the molecular density is enhanced around each of the H II regions. Such information would provide additional constraints for future modeling although one would still have some flexibility in adjusting the relative abundance of CS and C³⁴S.

In expanding our modeling to include the molecules HCO⁺ and C¹⁸O, the only parameter (relative to the CS modeling) that we allowed to vary was the relative abundance of the

target molecule. Good fits to the C¹⁸O profiles were obtained, but no values of the HCO⁺ abundance could be found that would fit satisfactorily both the J=1–0 and J=3–2 lines.

While the additional modeling of HCO⁺ and C¹⁸O provided no clear indication as to which of the three models is the closest to reality, it did result in our adding a bipolar outflow which improves the fit to the HCO⁺ profiles and nicely explains the changes in the asymmetries in the C¹⁸O profiles as a function of position. The poorer fit for C¹⁸O towards G for the global collapse model with or without an outflow gives a slight preference to either the multi-cloud model or the local collapse model over the global collapse model.

The expanded modeling also highlighted the flexibility and usefulness of the “mc” program (described in the appendix) in exploring possible spatial configurations.

Observations to test the local-collapse model include high-resolution observations of sub-millimeter dust emission to determine whether there are individual clumps around the H II regions. At present, the results are inconclusive; there is indirect evidence for dense molecular gas around the HII regions in order to confine them, and dust emission has been observed associated with ultracompact H II regions B and G1 & G2. If the individual clumps around the H II regions are confirmed, then the velocity field could be probed with high-resolution observations of a molecular line which is both a high-density tracer and an optically thin transition. The parameters of our final models could be used as input to a two-dimensional radiative transfer code so that possible rotation of the system of clouds and bipolar outflows could be realistically investigated. The parameters we found could be used with a full three-dimensional radiative transfer code to properly treat multiple clouds embedded in a low-density envelope.

J. A. Williams gratefully acknowledges sabbatical leaves in 1990 and 1997. He also gratefully acknowledges the hospitality extended by the University of Illinois Astronomy Department and the use of BIMA computers for data reduction and modeling during those sabbaticals and during numerous shorter visits to work on this project. J. A. Williams and H. R. Dickel gratefully acknowledge partial support from the Laboratory for Astronomical Imaging which is operated with funds provided by the Berkeley-Illinois-Maryland Association. The BIMA research was partially supported by the National Science Foundation through grants AST 90-24603, 93-20239, and 96-13999 to the University of Illinois. This work was also partially supported by a grant from the Hewlett-Mellon Fund for Faculty Development at Albion College, Albion, MI, and by the Office of Academic Affairs at Albion College. The J=3–2 HCO⁺ data were obtained with the 12 m telescope which at the time was operated by the National Radio Astronomy Observatory, a facility of the National Science Foundation operated under cooperative agreement by Associated Universities, Inc. The

authors thank Dr. N. J. Evans for illuminating discussions regarding infrared emission from star-forming regions and its possible effects on molecular excitation. Although it meant more work to follow through on the anonymous referee's suggestion to model HCO^+ and C^{18}O , the results were well worth the work and the delay in publishing the paper.

A. DESCRIPTION OF THE PROGRAM MC

Mc is a Fortran program which runs under X Windows to plot the output intensities from the cloud models made by the rt program. The purpose of mc is to permit the user to investigate interactively the effect that changes in the assumed physical structure of the region have on the predicted outgoing radiation. Mc is based on a plotting program written by L. H. Auer. Its inputs are the output files of rt, namely files of emergent intensity and optical depth as a function of impact parameter, velocity, and transition for a given molecule. Mc also reads a user-created file which gives the number of clouds, the distance of the complex, the names of files containing observed profiles, and for each cloud in the model the names of the intensity and optical depth files from rt and the velocity and position offset of that cloud from the origin. The user interactively specifies the kind of plot: intensity versus position along a cut, intensity versus velocity, or intensity as a function of position and velocity. The user also specifies the beam size, the impact parameters for the profile or the position of the cut, the transitions to plot, and whether or not the continuum should be subtracted. For line profiles the user also specifies which observed profiles should appear in the plot. After the plot is produced, the user is given the option of making more plots with the same input files. While the program is running the user has the option of changing the velocity and/or position offset of any of the clouds.

The outputs consist of the plot in the X Windows Tektronics window and in a postscript file which could be sent to a laser printer, a log file with the information from the user-created input file and the user's interactive inputs, and a file that contains the intensity versus velocity profiles that were computed to create the plot. For line-profile plots the rms difference between the model profile and the observed profile and some parameters describing the model profile are displayed in the X Windows VT window and written to the log file.

B. NUMERICAL DETAILS

B.1. Intensity Along a Line of Sight

The display program, mc, computes the intensity along a given line of sight for a given velocity and transition as

$$i = \sum i_{out} + i_{in}e^{-\tau} \quad (B1)$$

The sum is over the clouds in the line of sight from the most distant cloud to the closest. The i_{in} is the intensity that has accumulated so far. For the first cloud it is the 3K background. τ is the opacity of the cloud along that line of sight for the given velocity and transition, and i_{out} is the emergent intensity given by the program rt. The rt program correctly handles the effects of radiation on the populations of the energy levels in any one cloud, and the mc program assumes that the radiation from one cloud does not affect the populations of the energy levels of other clouds.

B.2. Justification for Ignoring the Effects of Radiation from One Cloud on Another

This assumption is true only when the relative velocities of the clouds are large enough that the line profiles do not overlap. However, even when the profiles do overlap, radiation from locations within a particular cloud probably has more effect on the populations of the molecular energy levels within that cloud than radiation from an external cloud. This larger effect is because the solid angle subtended by the external cloud will usually be much less than that subtended by the cloud that the particular point is in. One can see from Figure 27 that

$$\sin \theta_0 = r_2/(r_1 + r_2), \quad (B2)$$

or if $r = r_2/r_1$, then

$$\theta_0 = \arcsin(r/(1+r)). \quad (B3)$$

Integrating over the portion of a unit sphere with polar angle θ gives the solid angle, Ω , of the external cloud.

$$\Omega = \int_0^{\theta_0} 2\pi \sin \theta d\theta = 2\pi(1 - \cos \theta_0) \quad (B4)$$

There are 4π steradians in a full sphere, so the percentage of the celestial sphere at A covered by the external cloud is just $50(1 - \cos \theta_0)$. Table 8 gives some sample values.

B.3. Convolution

For beam widths larger than zero, a gaussian-weighted sum is formed of the intensities at grid points on the sky within 1.5 beam widths of the desired position. The spacing of the grid points is one twentieth of the beam width.

REFERENCES

Botschwina, P. 1989, in Ion and Cluster Spectroscopy and structure, ed. J.P.O. Maier (New York: Elsevier), 59

de Pree, C.G., Mehringer, D.M., Goss, W.M. 1997, ApJ, 482, 307

de Pree, C.G., Wilner, D.J., Goss, W.M., Welch, W.J., McGrath, E. 2000, ApJ, 540, 308

Dickel, H. R., & Auer, L. H. 1994, ApJ, 437, 222

Dickel, H. R., & Goss, W. M. 1990, ApJ, 351, 189

Dickel, H. R., Williams, J. A., Upham, D. E., Welch, W. J., Wright, M.C. H., Wilson, T. L., & Mauersberger, R. 1999, ApJS, 125, 413 (paper1)

Doty, S. D., & Neufeld, D. A. 1997, ApJ, 489, 122

Dreher, J. W., Johnston, K. J., Welch, W. J., & Walker, R. C. 1984, ApJ, 283, 632

Evans, N. J. 1999, ARA&A, 37, 311

Evans, N. J. 2000, private communication

Gwinn, C. R., Moran, J. M., & Reid, M. J. 1992, ApJ, 393, 149

Jackson, J.M. & Kraemer, K. E. 1994, ApJ, 429, L37

Irvine, W. M., Goldsmith, P. F., & Hjalmarson, A. 1987, in Interstellar Processes, eds. D. J. Hollenbach & H. A. Thronson, Jr., Astrophysics & Space Science Library, 134, 566

Keto, E. R., Lattanzio, J. C., & Monaghan, J. J. 1991, ApJ, 383, 639

Miyawaki, R., Hayashi, M., & Hasegawa, T. 1986, ApJ, 305, 353

Miyawaki, R., Hayashi, M., & Hasegawa, T. 1994, in Astronomy with Millimeter and Sub-millimeter Wave Interferometry, eds. M. Ishiguro & Wm. J. Welch, ASP Conf. Ser. 59, 251 (and unpublished poster figures)

Mufson, S. L., & Liszt, H. S. 1977, *ApJ*, 212, 664

Scoville, N. Z., & Solomon, P. M. 1973, *ApJ*, 180, 31

Serabyn, E., Güsten, R., & Schulz, A. 1993, *ApJ*, 413, 571

Shu, F. H. 1977, *ApJ*, 214, 488

Shu, F. H., Adams, F. C. & Lizano, S. 1987, *ARA&A*, 25, 23

Ward-Thompson, D., Berry, D. S., & Robson, E. I. 1992, *MNRAS*, 257, 180

Welch, Wm. J., Dreher, J. W., Jackson, J. M., Terebey, S., & Vogel, S. N. 1987, *Science*, 238, 1550

Wilner, D.J., de Pree, C.G., Welch, W.J., Goss, W.M., 2001 *ApJ*, 550 L82

Wilson, T. L., & Rood, R. T. 1994, *Ann. Rev. Astron. Aph*, 32, 191

Woods, R.C., Dixon, T.A., Saykally, R.J., & Szanto, P.G. 1975, *Phys. Rev. Lett.* 35, 1269

Fig. 1.— Model spectra (a) The effect on a profile from two clouds of changing only the turbulent velocity. (b) The effect on a profile of changing only the relative speed of two clouds in the line of sight. (c) The profile in the direction of H II region B from the preliminary multi-cloud model. The zero of the velocity scale has been set to the velocity of cloud A. (d) To show the contributions of the individual clouds to the profile in (c), multiples of 30 km s^{-1} have been added to the velocities of the individual clouds. The clouds are designated by the letters used in Table 1 and the short vertical lines indicate the velocity offsets.

Fig. 2.— Comparison of CS spectra from the final two-clump model with observations in the directions of H II regions A and G. The histograms are the observed profiles, and the smooth curves are the model profiles. (a) and (b) The predicted strengths of the $J=7-6$ lines are less than observed. (c) The predicted line towards H II region A matches the BIMA observations. (d) The predicted line towards H II region G does not have the absorption on the high velocity side of the profile that is evident in the BIMA observations. (e) The predicted strengths of the $J=2-1$ transition with 20" beam in the directions of A and G are less than observed.

Fig. 3.— Two-clump model with envelope around clump A. (a) Profile for CS $J=2-1$ in the direction of H II region A with a 5" beam. (b) Profile for $J=2-1$ in the direction of H II region G with a 5" beam. (c) Profiles for other transitions in the direction of A with a 20" beam.

Fig. 4.— Results for the initial multi-cloud model. The panels of the rest of the figures showing results of models (Figs. 5–11 follow this same pattern of presentation). (a) Observed and predicted profiles for higher transitions of CS in the direction of H II region A with a 20" beam. (b) Observed and predicted profiles for higher transitions of CS in the direction of H II region G with a 20" beam. (c) Observed and predicted profiles for the $J=2-1$ transition of CS in the direction of A with a 5" beam. (d) Observed and predicted profiles for the $J=2-1$ transition of CS in the direction of G with a 5" beam. (e) Observed and predicted profiles for the $J=2-1$ transition of CS in the directions of A and G with a 20" beam.

Fig. 5.— Results for the intermediate multi-cloud model. The radii of the clouds at A and G have been increased to better represent the CS $J=2-1$ transition in a 20" beam. (f) Observed and predicted profiles for the $J=2-1$ transition of CS in the direction of H II region B.

Fig. 6.— Results for the preliminary multi-cloud model which now includes an additional 17 km s^{-1} cloud at the rear. The predicted emission in the $J=7-6$ transition in the directions of A and G is less than observed.

Fig. 7.— Results for the preliminary global collapse model where H II region A and a cloud surrounding it have been added. There is not enough emission in the higher transitions especially in the direction of G. There is not enough emission in the $J=2-1$ transition with a $20''$ beam, especially in the direction of G.

Fig. 8.— Results for the preliminary local collapse model with uniform, static cores surrounded in the case of A and G by envelopes in free fall. A small, low- H_2 density cloud (component B', which may be an extension of cloud A) has been added in front of H II region B. Now the higher transitions and the emission in the direction of B fit well, but the emission from the $J=2-1$ transition with a $20''$ beam is still weak.

Fig. 9.— Results for the final multi-cloud model. The predicted emission from the $J=7-6$ transition in the direction of A and from the $J=2-1$ transition with $20''$ beam in the direction of G are weaker than observed.

Fig. 10.— Results for the final Shu global collapse model. The predicted emission from the $J=2-1$ transition with $20''$ beam is weaker than observed especially in the direction of G.

Fig. 11.— Results for the final local collapse model. The predicted emission from the $J=2-1$ transition with $20''$ beam is weaker than observed.

Fig. 12.— Relative sizes and locations of clouds along the line of sight. The shaded circles are H II regions. The observer is at the bottom of each panel. The horizontal displacement is in the E-W (RA) direction on the plane of the sky with the scale indicated at the bottom. (a) Multi-cloud model. The circles around G H II and B are dashed to indicate that the CS abundance has been set so low that these clouds are essentially H II regions. (b) Local collapse model. The dashed circles in clouds A and G represent the boundaries between the inner uniform, static cores and the outer free-falling envelopes. (c) Global collapse model.

Fig. 13.— Deconvolved profiles from the final multi-cloud model. The plots are similar to Figure 1d except the velocity of cloud A has not been subtracted from the velocity of each cloud before shifting it along the velocity axis. The vertical lines with the labels mark the location of the cloud components; the shorter vertical line to the left of each label gives the location of 0.0 km s^{-1} for that component (and thus indicates the amount of the velocity shift). The observed profiles are also included in the plots. Cloud A and the core of cloud G are the major contributors to the $J=7-6$ line. Cloud A produces a major part of the emission in the $5''$ $J=2-1$ profile in the direction of G, and G' produces the absorption observed on the high velocity side of that profile.

Fig. 14.— Deconvolved profiles from the final global collapse model (similar to Figure 13). The cores of clouds A and G are the major contributors to the $J=7-6$ lines. The core of cloud G produces the major part of the emission in the $5''$ $J=2-1$ profile in the direction of G, and cloud B and the envelope of cloud G produce the absorption observed on the high velocity side of that profile.

Fig. 15.— Deconvolved profiles from the final local collapse model (similar to Figure 13). The cores of clouds A and G are the major contributors to the $J=7-6$ lines. The cores of clouds A and G contribute equally to the $5''$ $J=2-1$ profile in the direction of G. Cloud A' also contributes significantly. Cloud B produces the absorption observed on the high velocity side of that profile.

Fig. 16.— Position-velocity plots from the three final models along the a and c cuts used by Miyawaki et al. (1994). Cut a is parallel to the main axis of the molecular cloud with values increasing to the east; cut c is perpendicular to the main axis with values increasing to the north. Offsets are measured from the intersection of cuts a and c which is close to H II G. The H II regions are located within their respective clouds except in the mc model where cloud G (Serabyn's central cloud) has a projected offset from H II region G of $\sim 7''$ along cut a and $\sim 7''$ along cut c. The velocity and offset position (of the projection) of a cloud component along the two cuts are labeled with its letter. The contours are in units of 10^{-14} $\text{erg s}^{-1} \text{cm}^{-2} \text{Hz}^{-1} \text{sr}^{-1}$. For cut a, the intensities go from -0.585 to 4.23 in steps of 0.535 which is equivalent to -0.27 to 2.0 Jy beam^{-1} in steps of 0.25; this range is similar to that in Figure 8 of paper 1 except they used an interval of 0.5 ($= 2\sigma$) rather than 0.25. For cut c, the intensities go from -1.16 to 2.54 in steps of 0.37 which corresponds to -0.52 to 1.2 Jy beam^{-1} in steps of 0.17.

Fig. 17.— Observed and predicted profiles for the $J=3-2$ transition of C^{34}S towards A and G for a $20''$ beam for the three final models. The profiles towards H II region A are on the left and those towards G are on the right. Profiles from the multi-cloud model are in the first row, from the global collapse model are in the second and from the local collapse model are in the third. The panels in Figures 18 – 23 follow the same arrangement.

Fig. 18.— Observed and predicted profiles for the $J=5-4$ transition of C^{34}S towards A and G for a $20''$ beam for the three final models.

Fig. 19.— Observed and predicted profiles for the $J=7-6$ transition of C^{34}S towards A and G for a $20''$ beam for the three final models.

Fig. 20.— Predicted profiles for the $J=1-0$ transition of CS towards A and G with a $2''$ beam for the three final models.

Fig. 21.— Deconvolved profiles for the $J=1-0$ transition of CS towards A and G with a $2''$ beam for the three final models.

Fig. 22.— Predicted profiles for the $J=5-4$ transition of CS towards A and G with a $2''$ beam for the three final models.

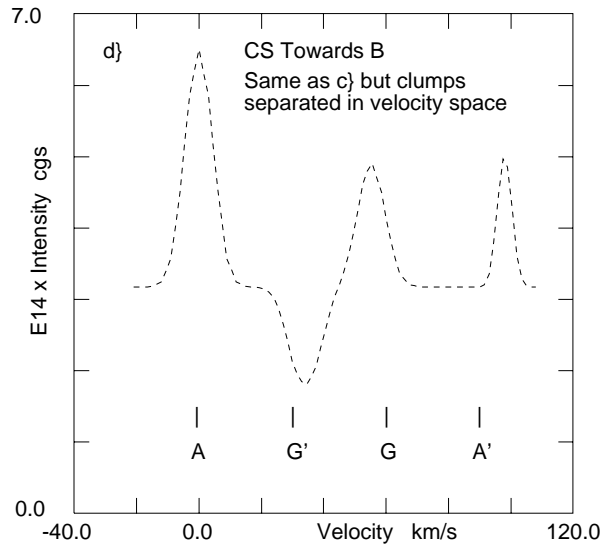
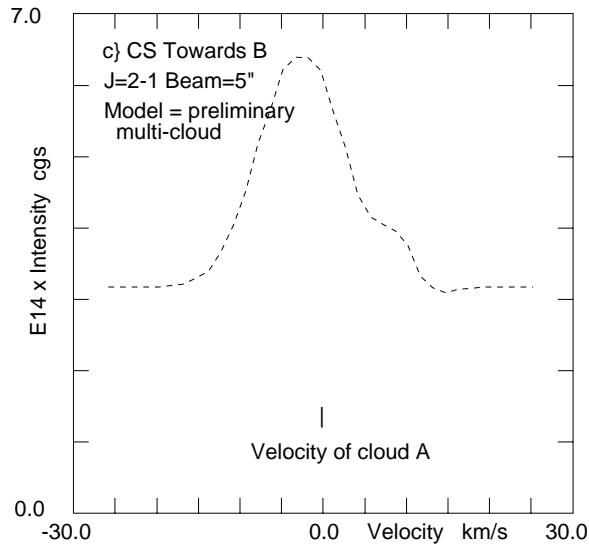
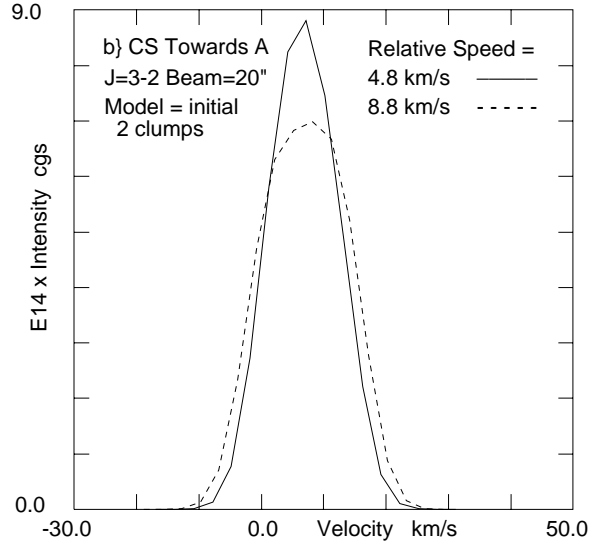
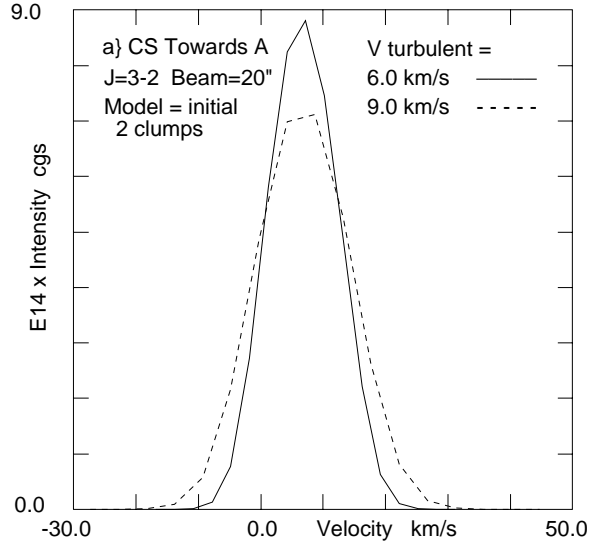
Fig. 23.— Observed and predicted profiles for HCO^+ for the $J=1-0$ transition towards A and G for a $7''$ beam and for the $J=3-2$ transition towards G for a $24''$ beam : left side is for the final global collapse model and right side is for the final local collapse model. Note how the predicted intensities for the $J=1-0$ transition are too weak while those for $J=3-2$ are too strong.

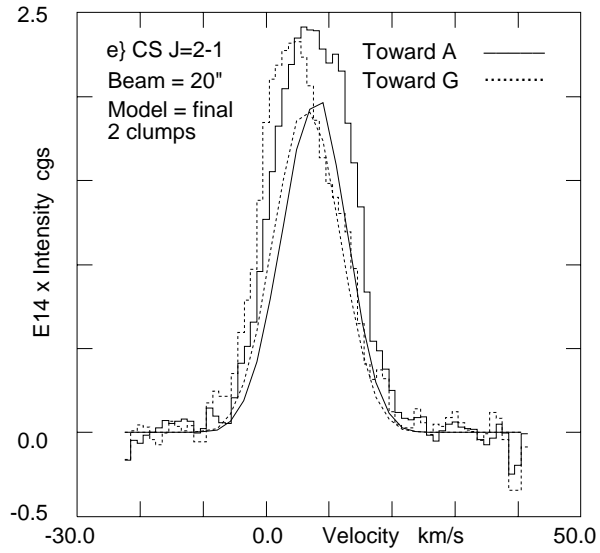
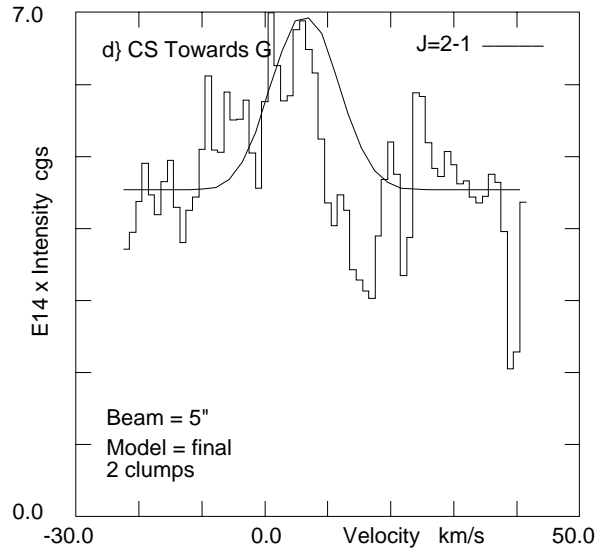
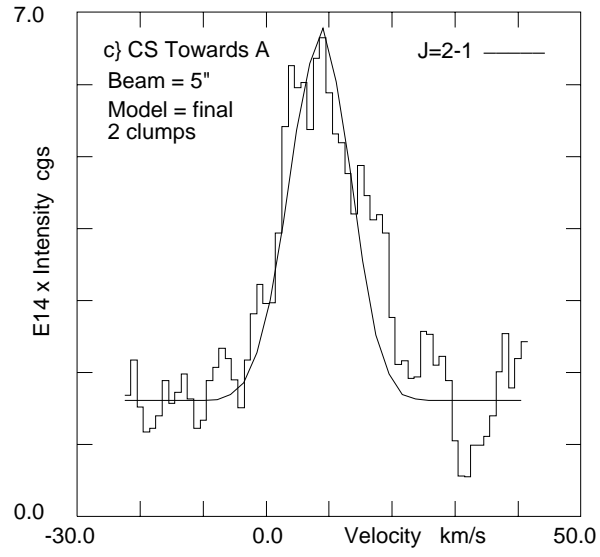
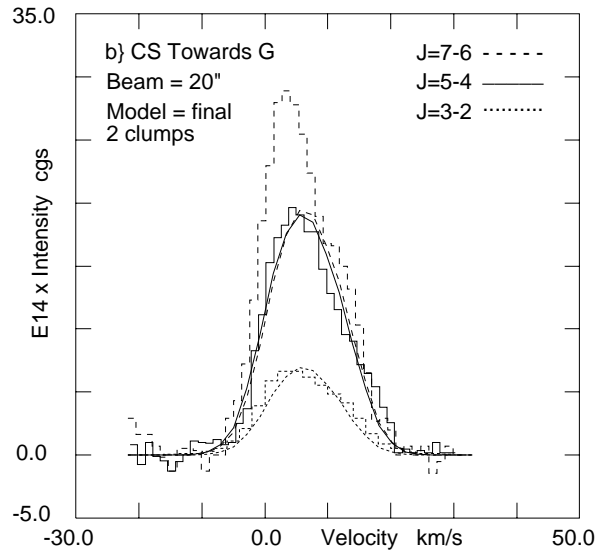
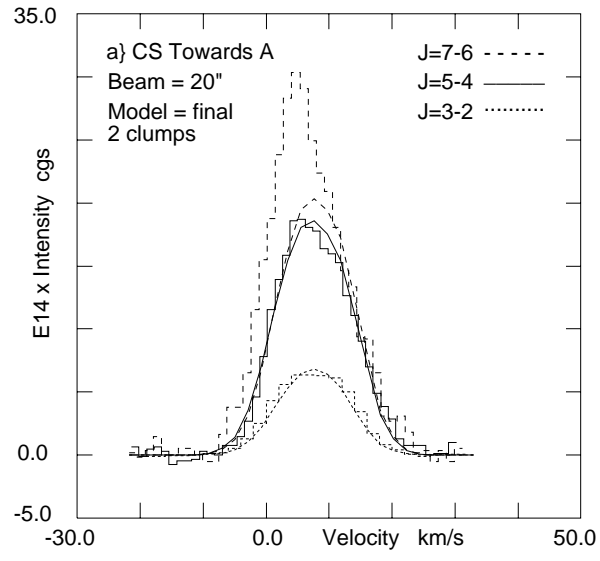
Fig. 24.— Observed and predicted profiles for HCO^+ for the final multi-cloud model for the $J=1-0$ transition towards A and G for a $7''$ beam and for the $J=3-2$ transition towards G for a $24''$ beam: left side without an outflow and right side with the addition of an outflow. The outflow provides the needed increase in the intensity of the $J=1-0$ emission without exceeding the observed line strength for $J=3-2$.

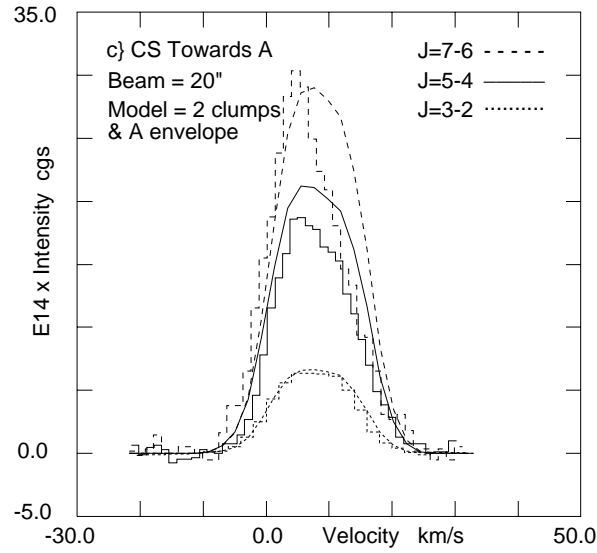
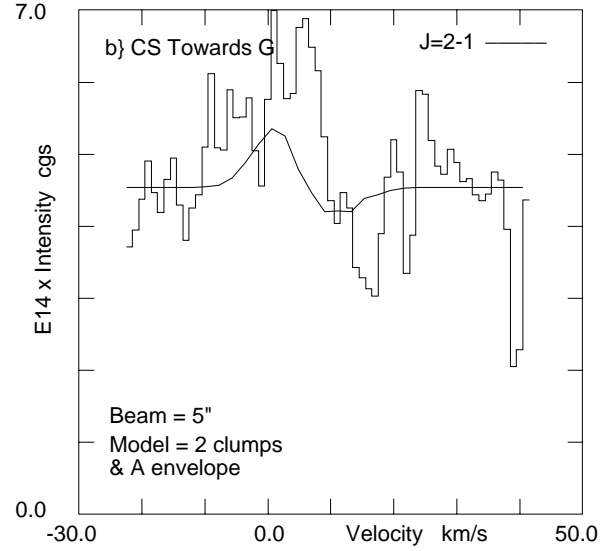
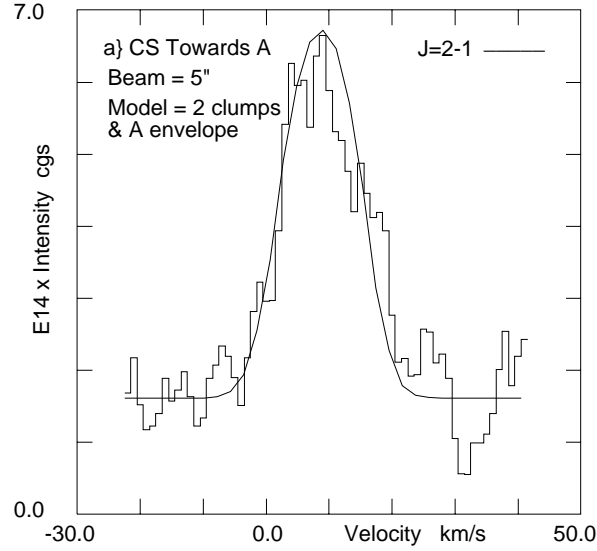
Fig. 25.— Observed and predicted profiles for the $J=2-1$ transition of C^{18}O for a $12''$ beam for the three final models: left side towards A and right side towards G. The overall fit is generally good but the asymmetries at the peak of the emission are not matched.

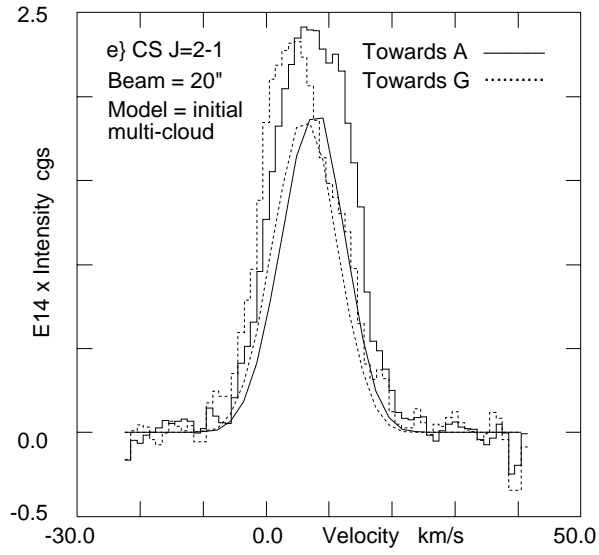
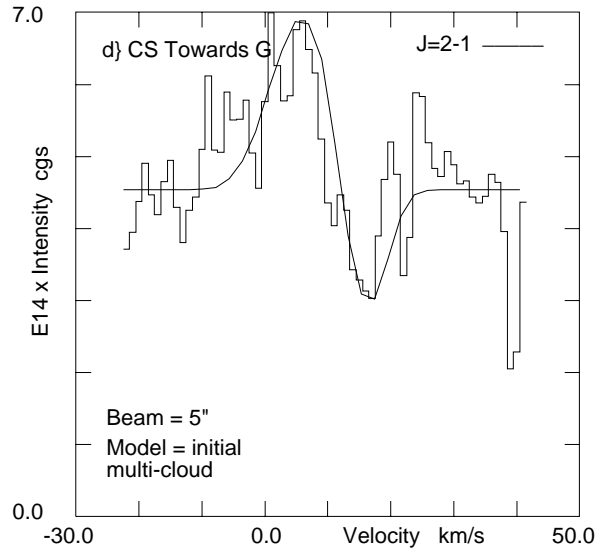
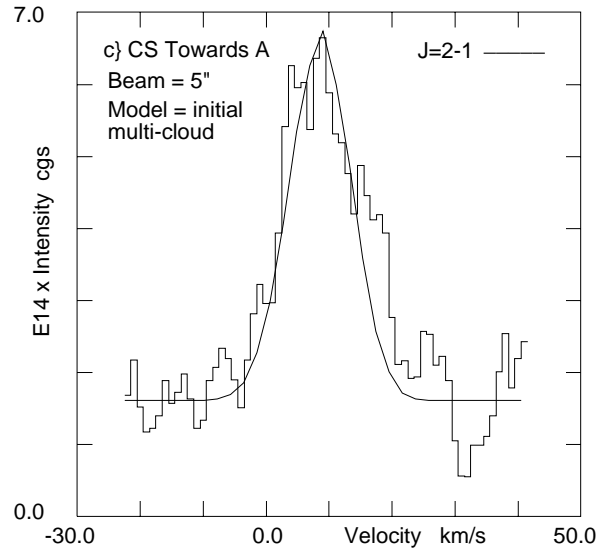
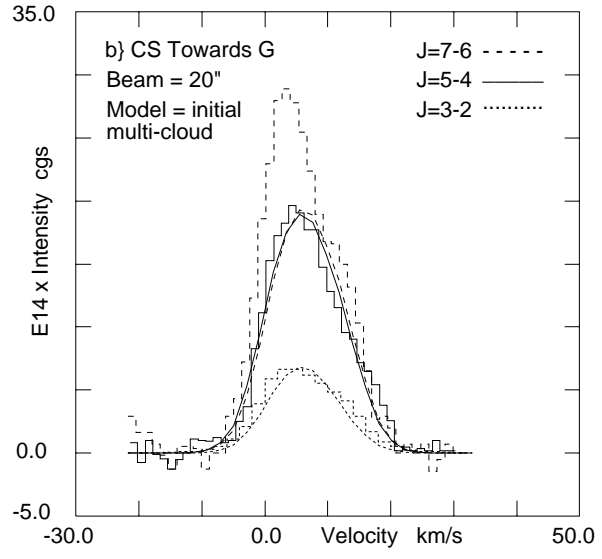
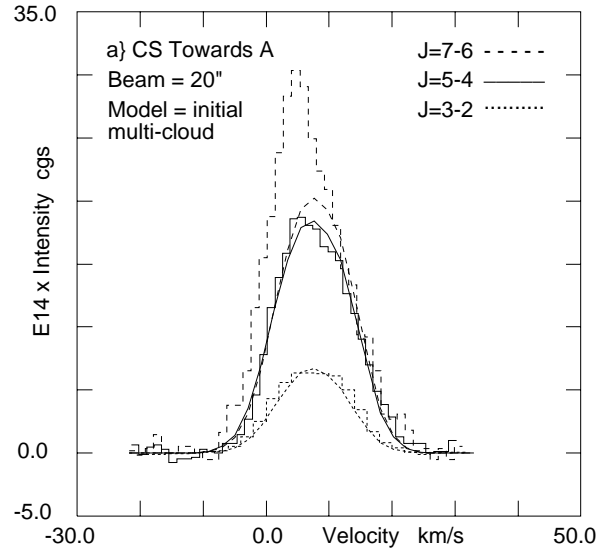
Fig. 26.— Observed and predicted profiles for the $J=2-1$ transition of C^{18}O for a $12''$ beam for the three final models but with the addition of an outflow: left side towards A and right side towards G. The addition of an outflow allows the asymmetric nature of the profiles to be matched better except towards G in the global collapse model.

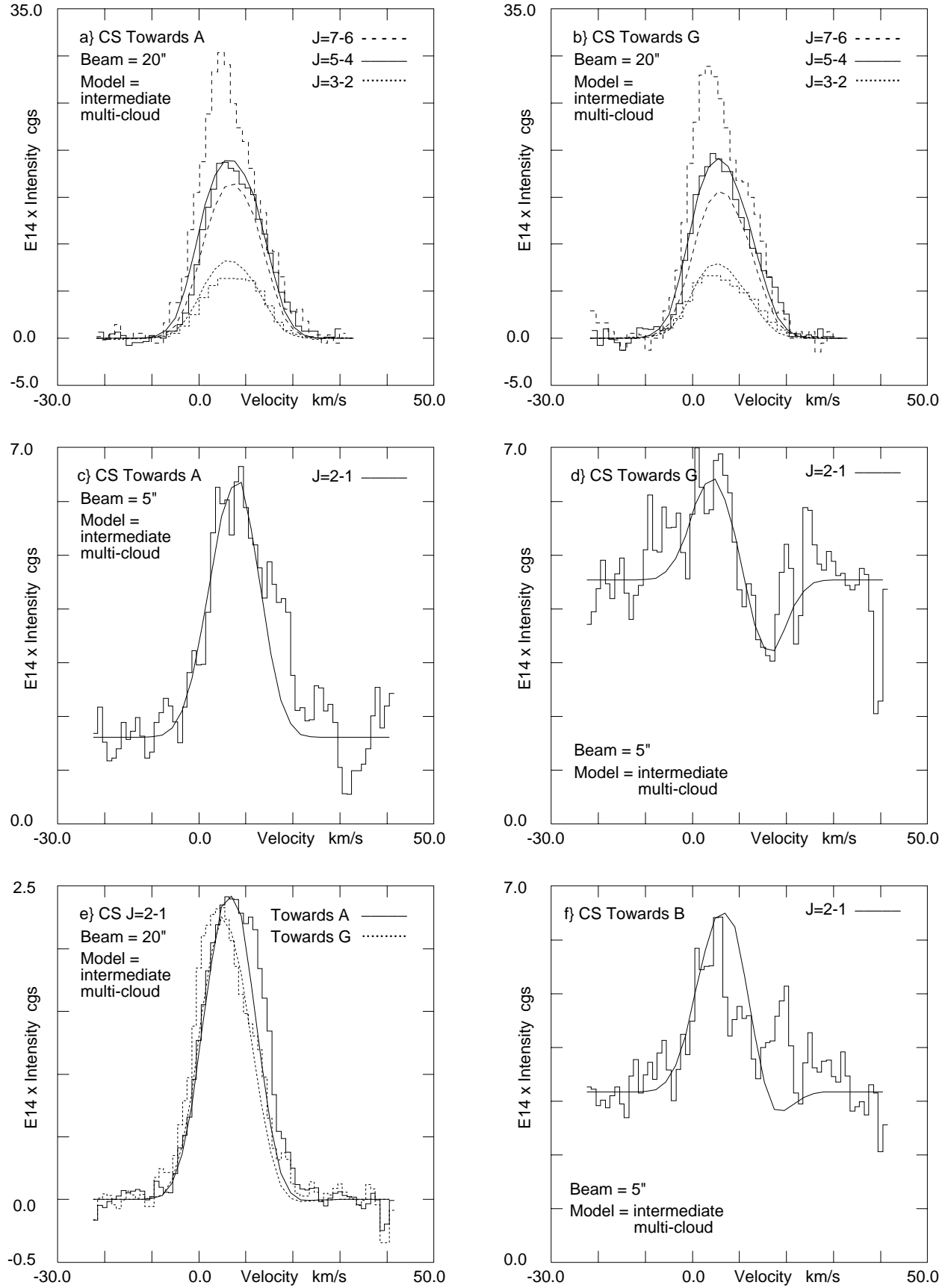
Fig. 27.— Diagram of the angle subtended by the radius of a spherical cloud seen from a point outside the cloud. The percentage of the celestial sphere covered by the cloud as seen from A is $50(1 - \cos(\theta_0))$.

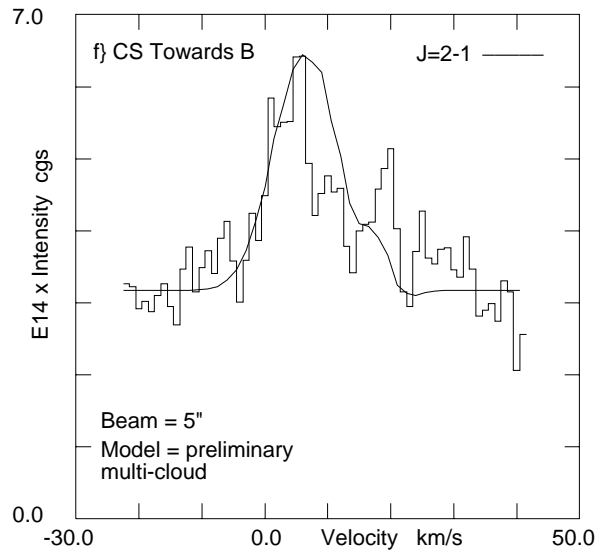
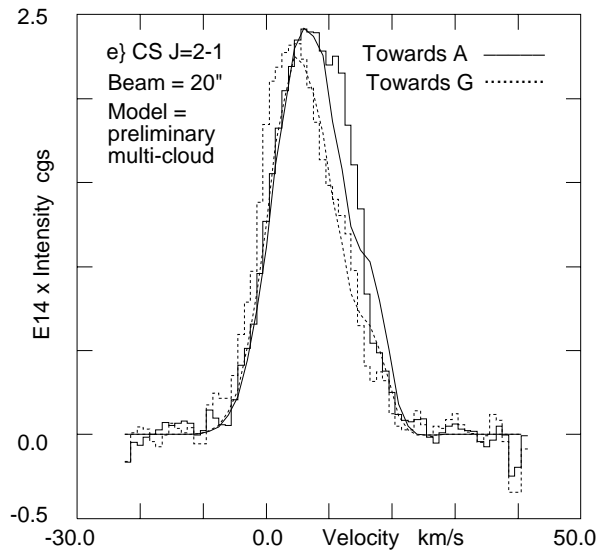
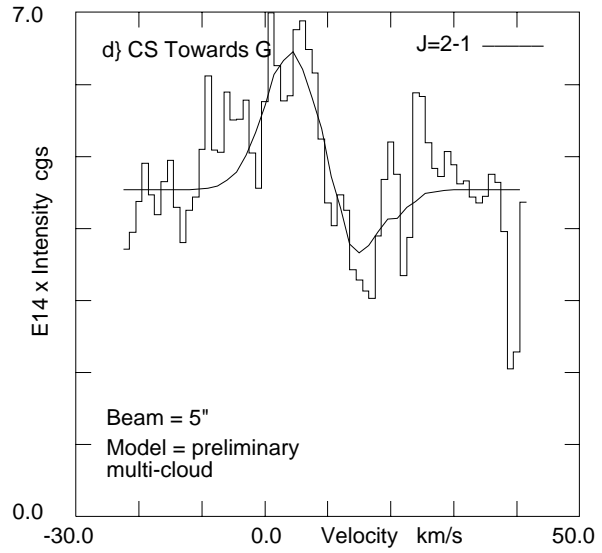
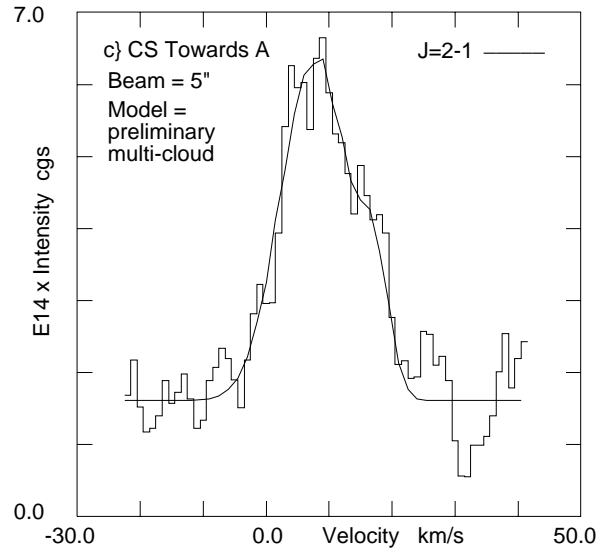
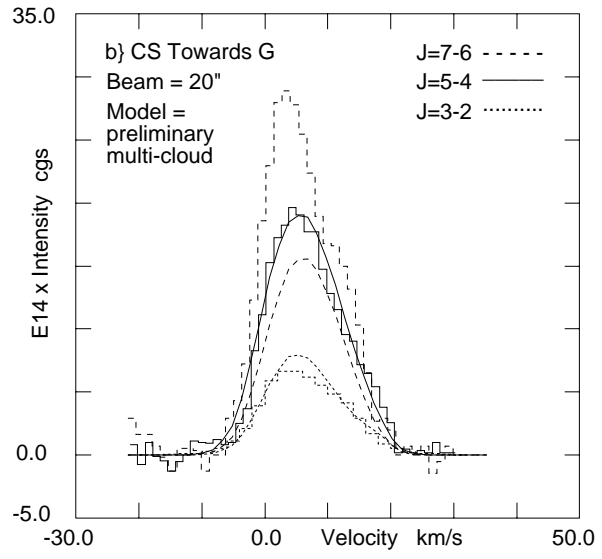
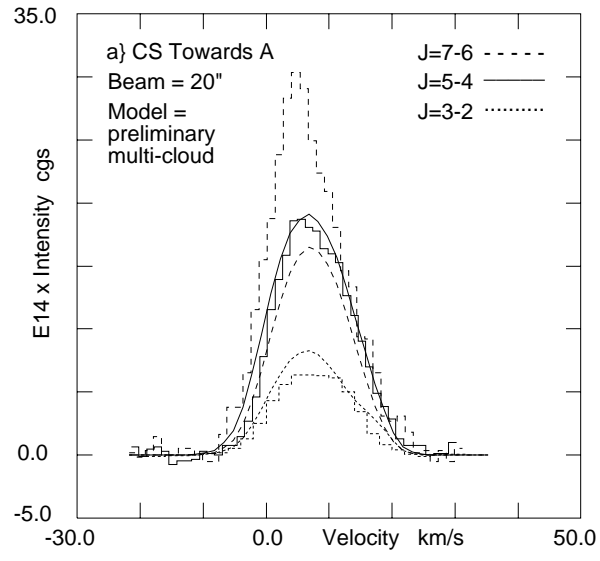


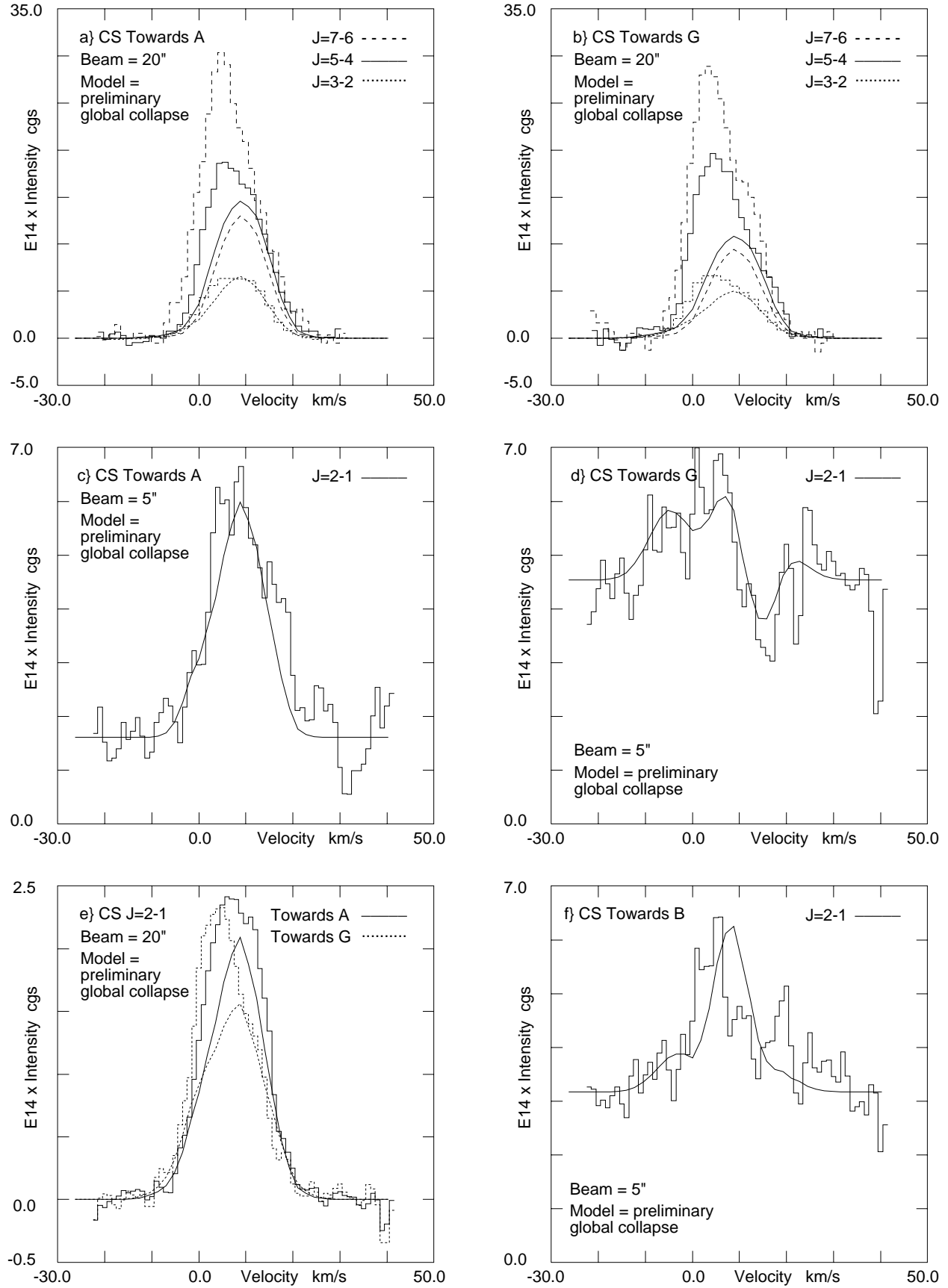


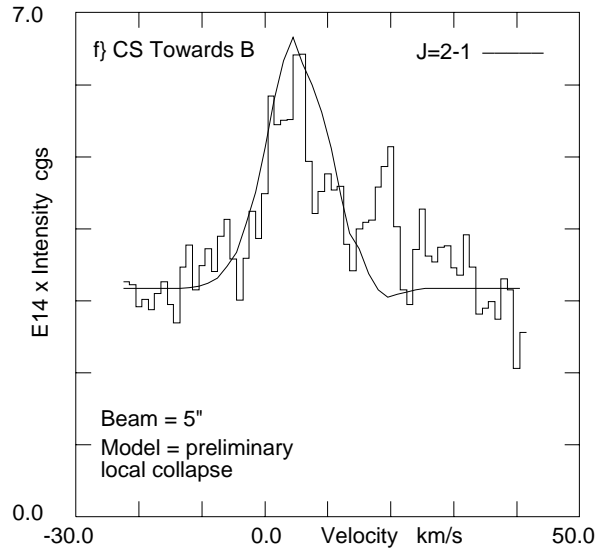
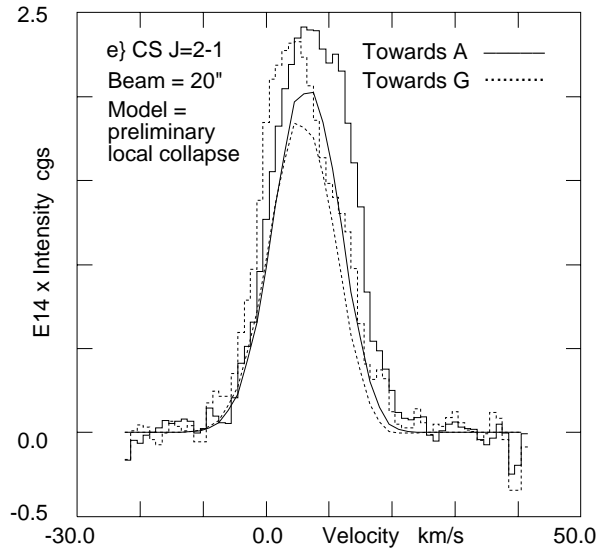
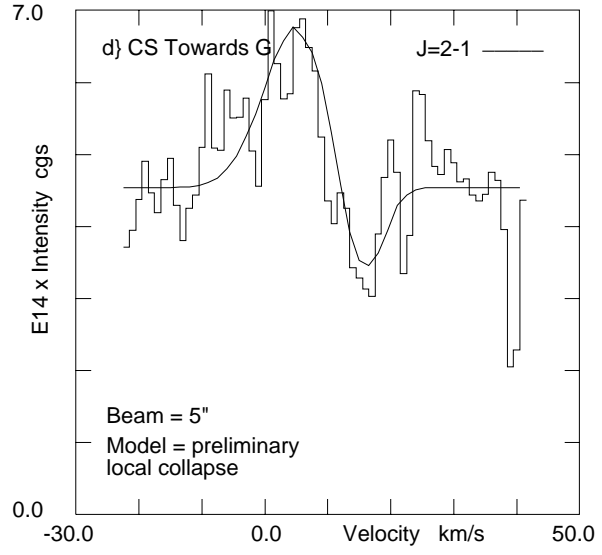
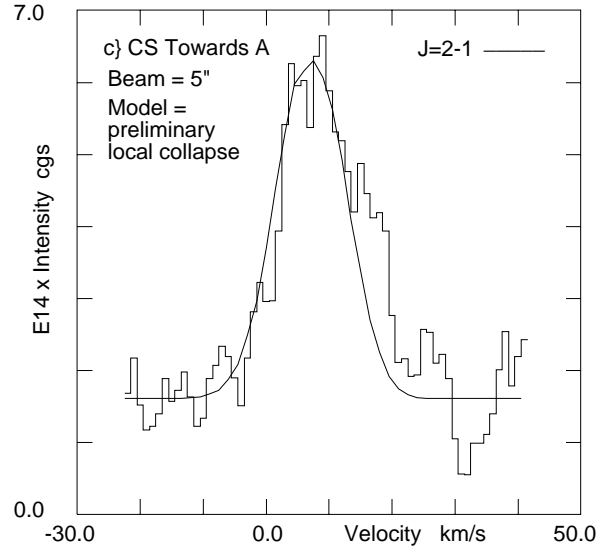
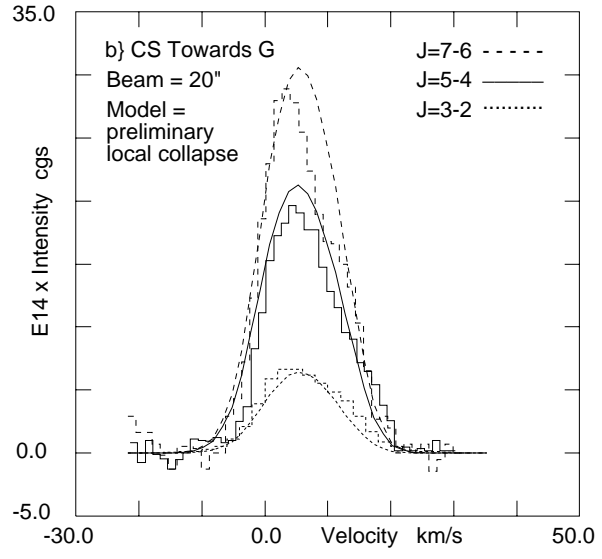
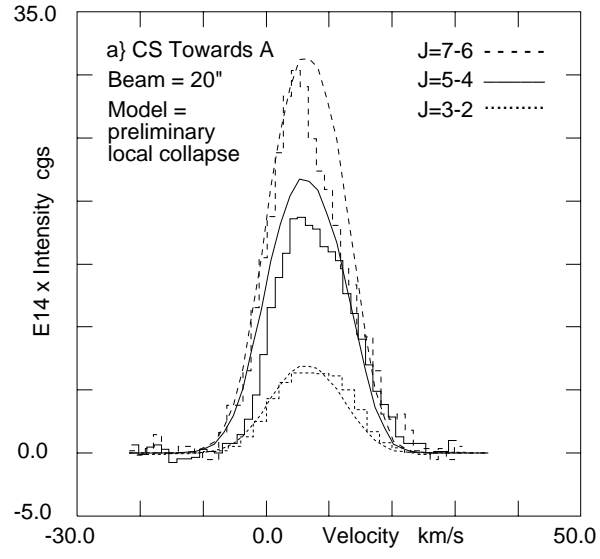


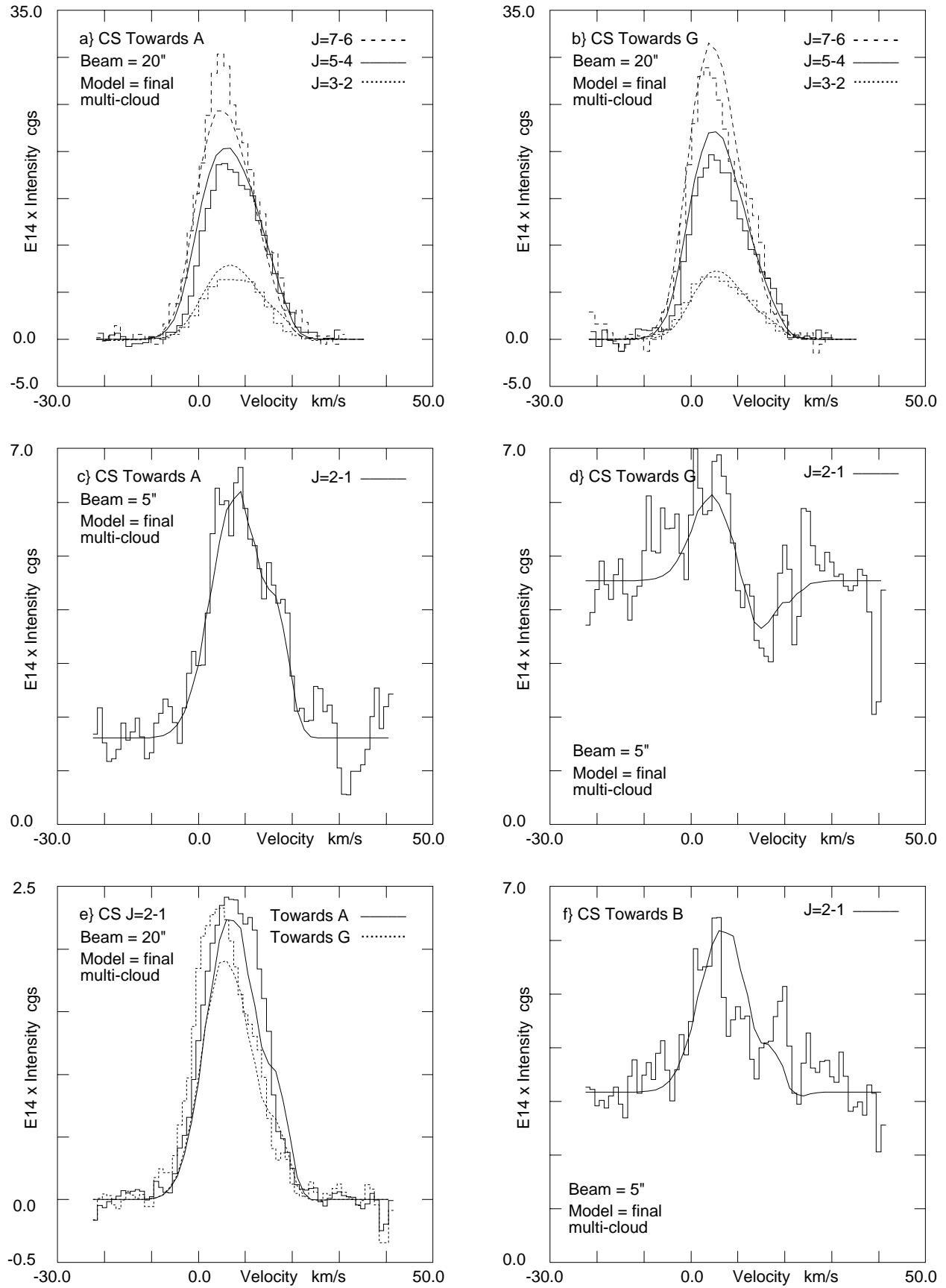


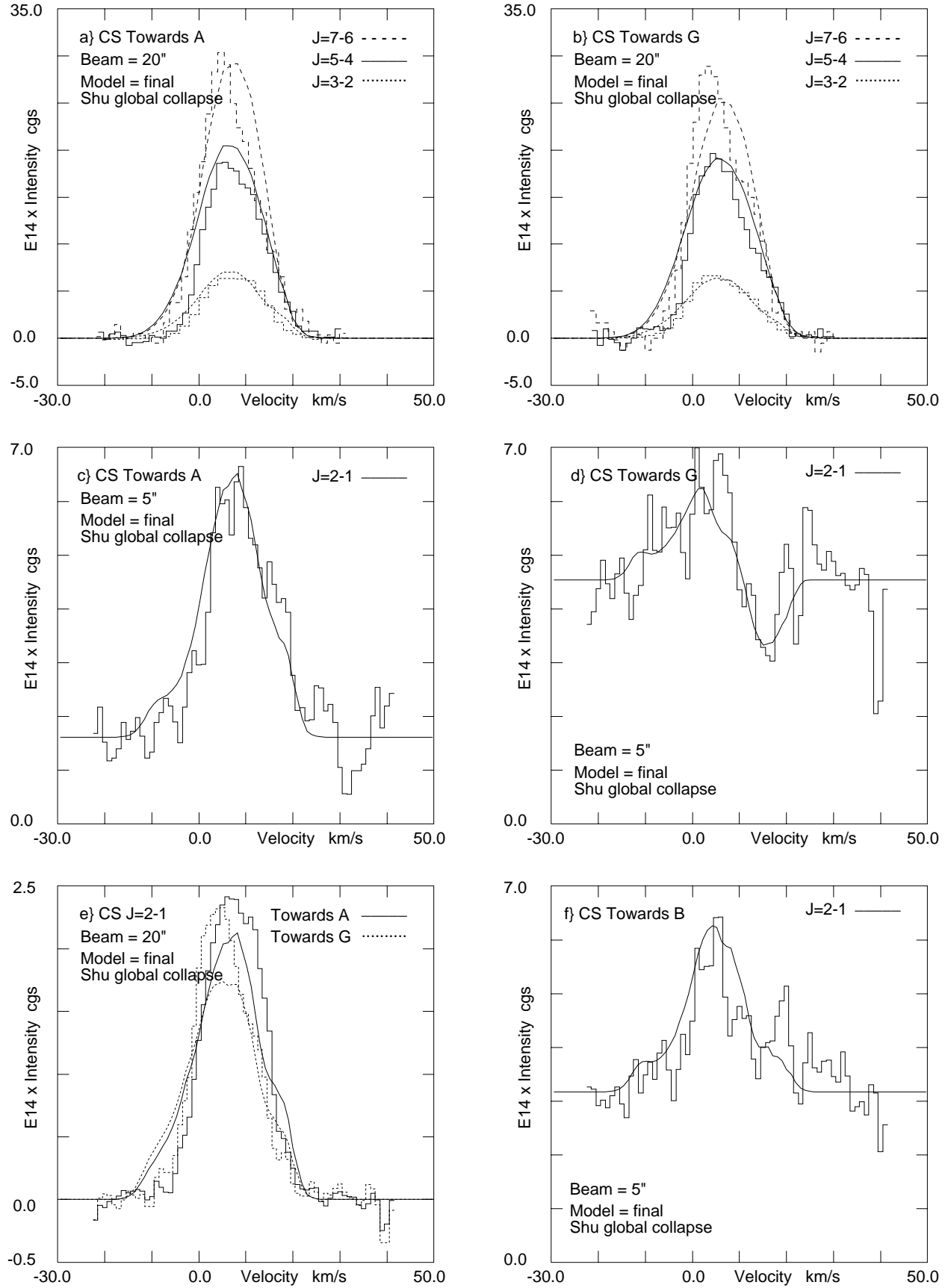


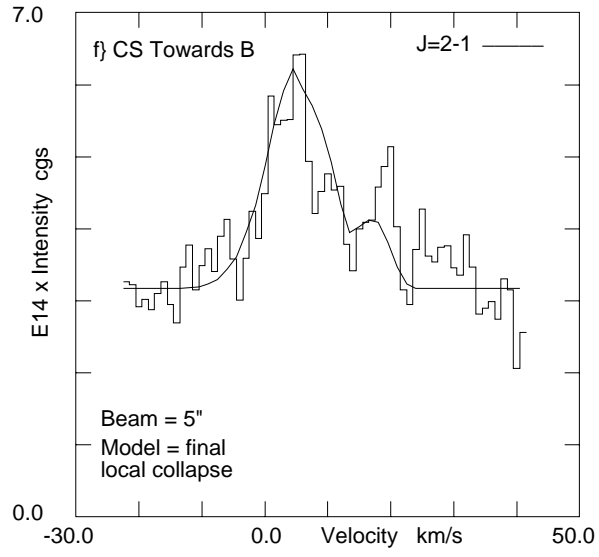
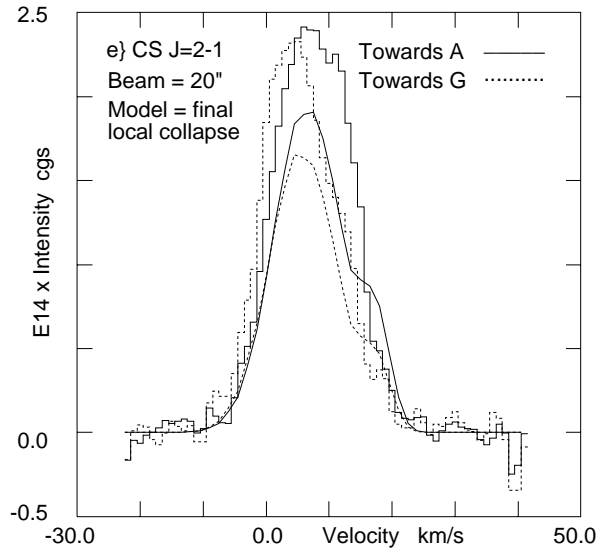
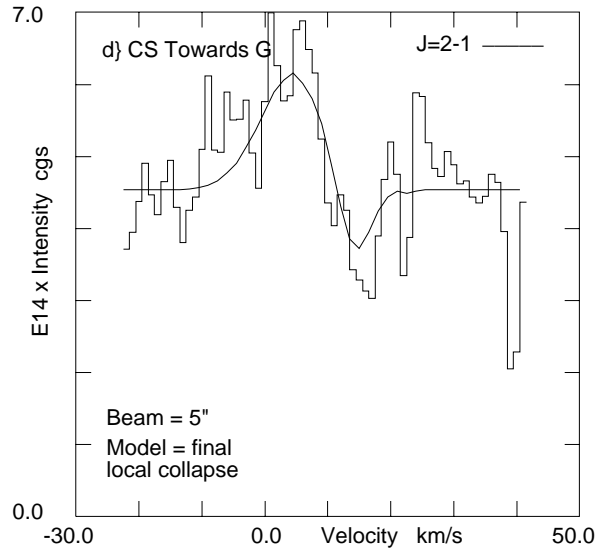
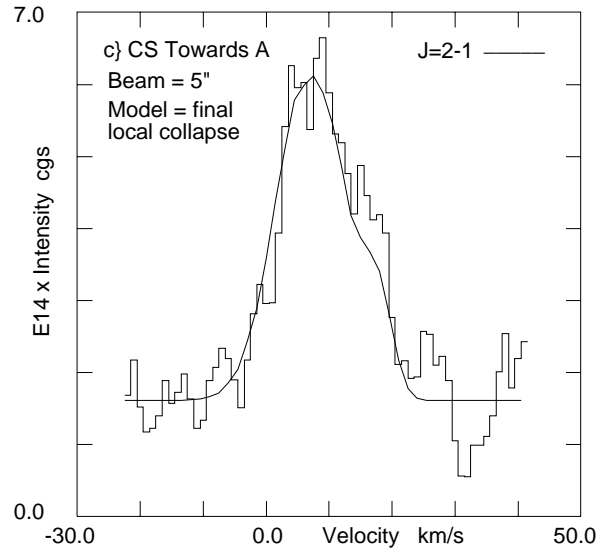
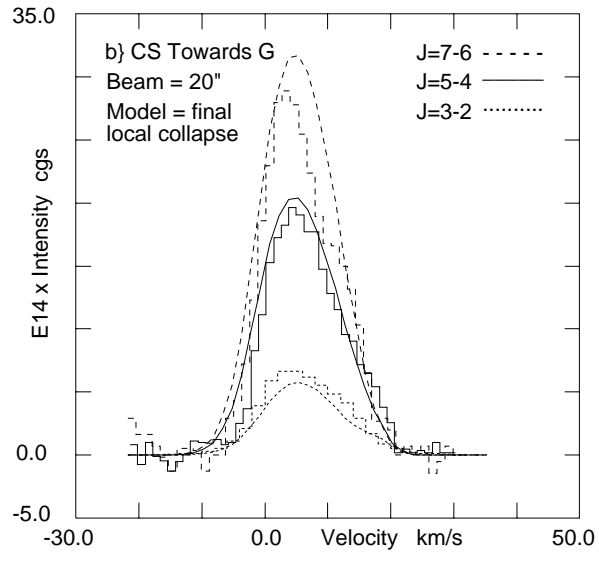
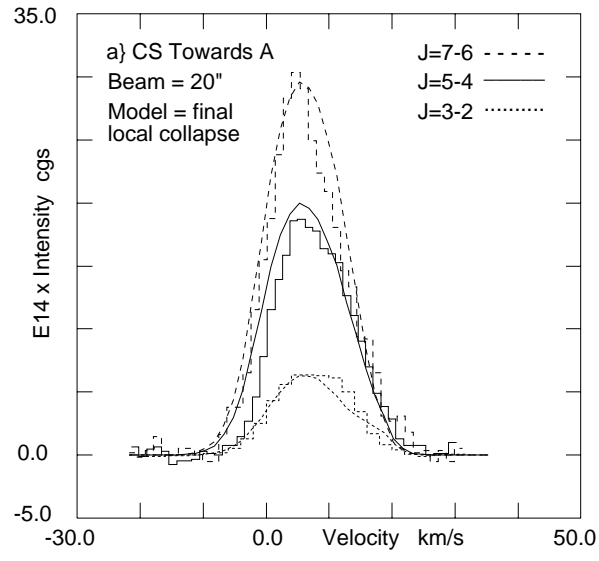






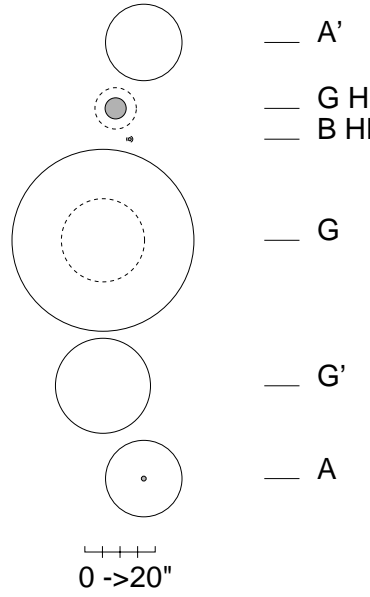




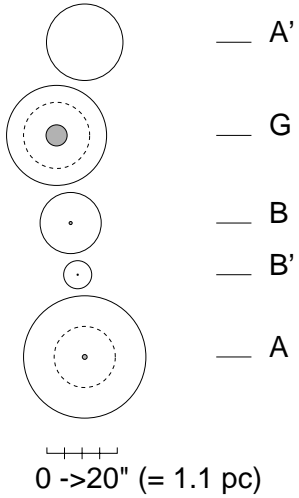


FINAL MODELS -- VIEW ALONG LINE OF SIGHT

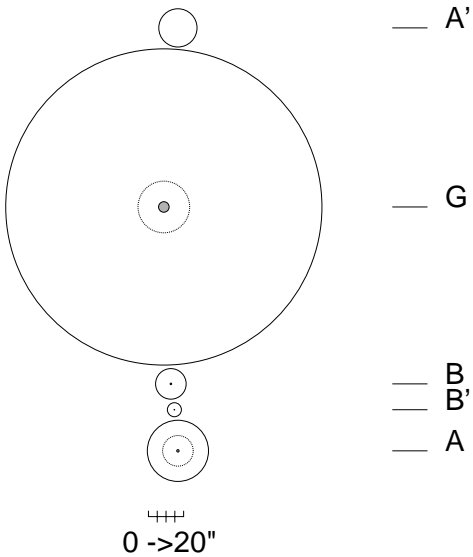
a} Multi-cloud

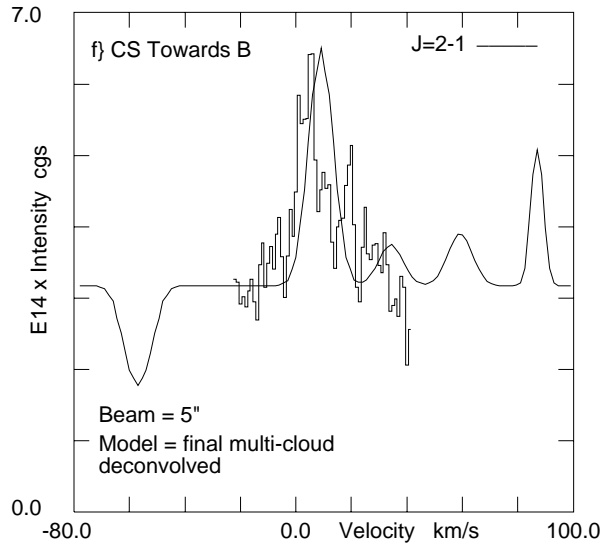
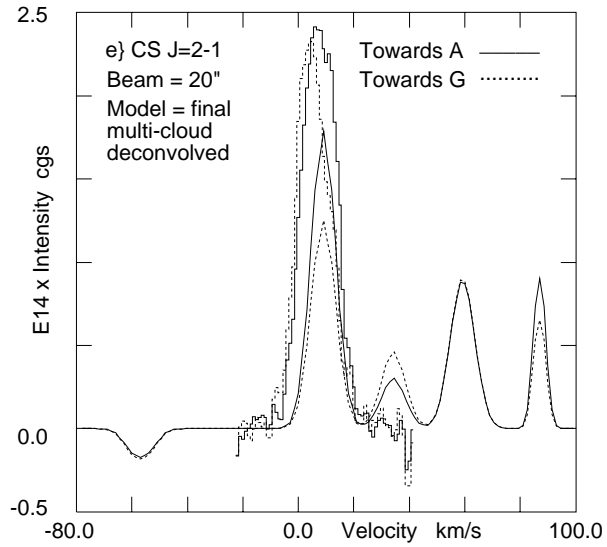
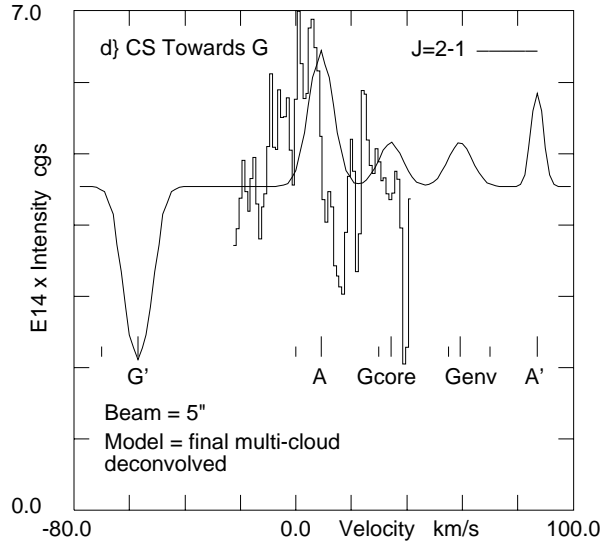
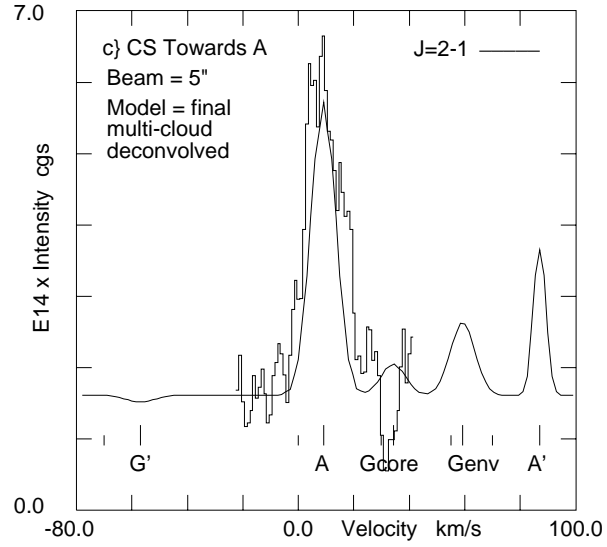
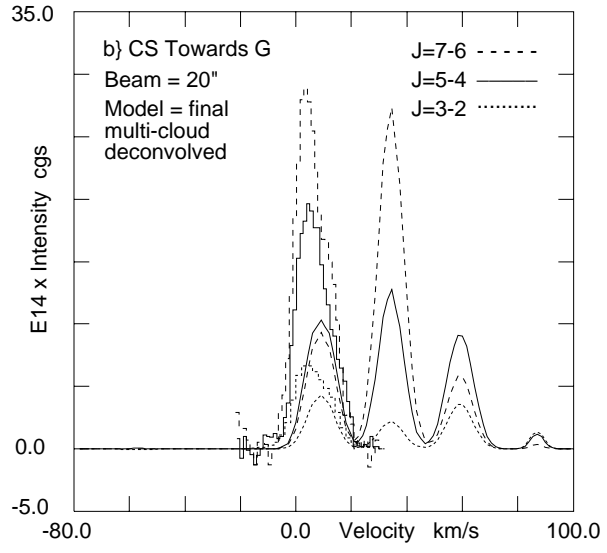
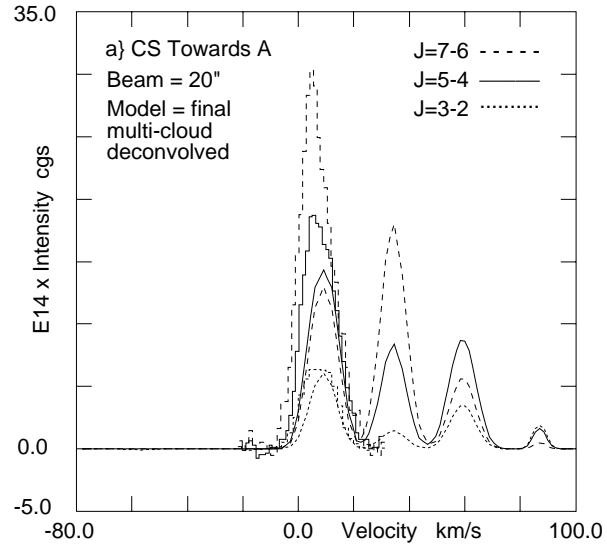


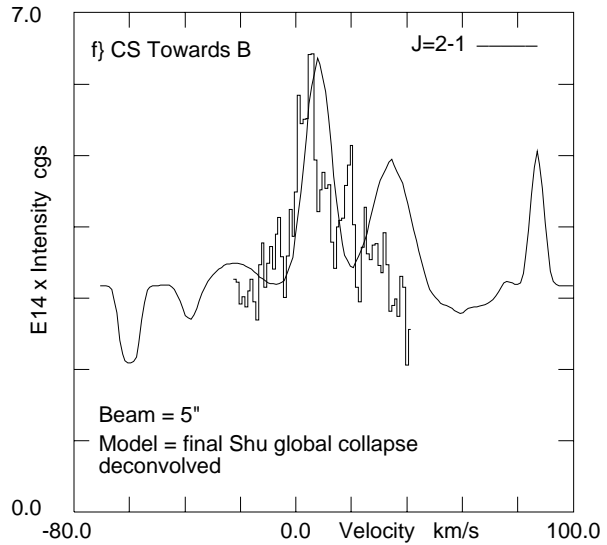
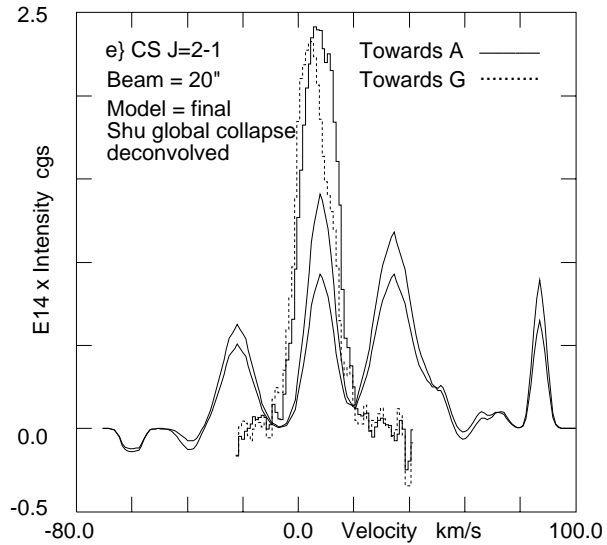
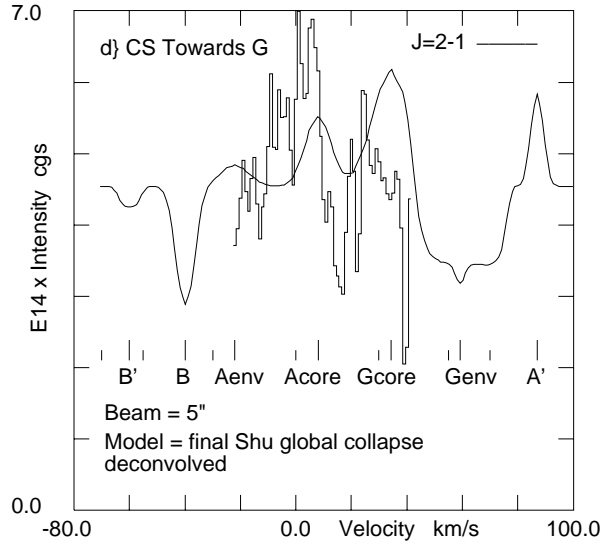
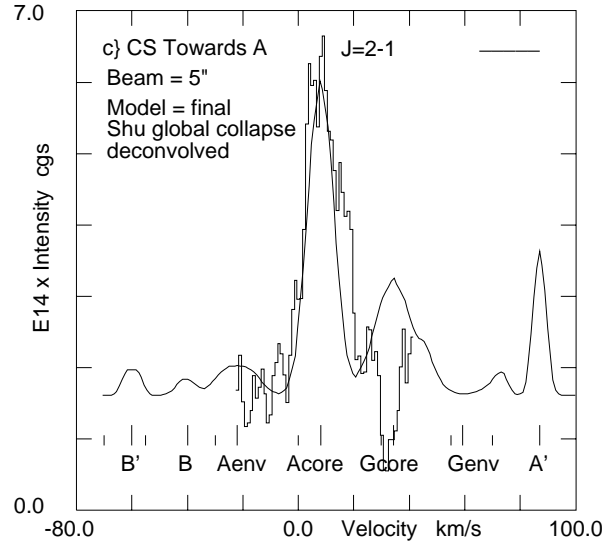
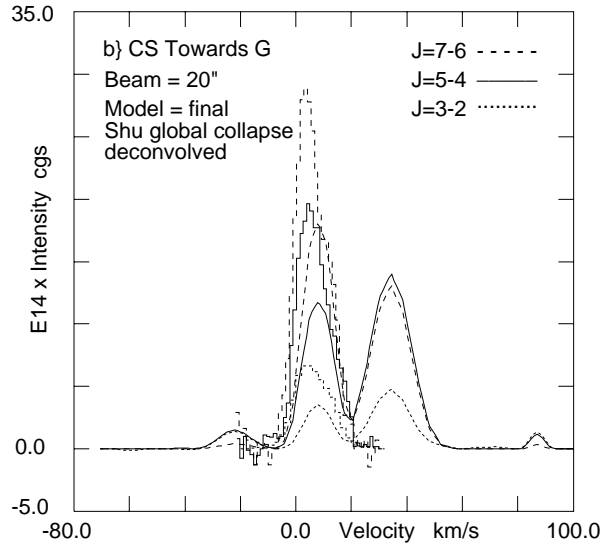
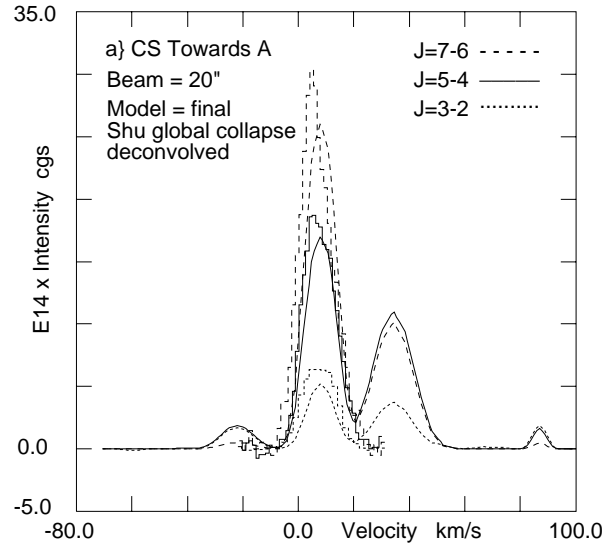
b} Local collapse

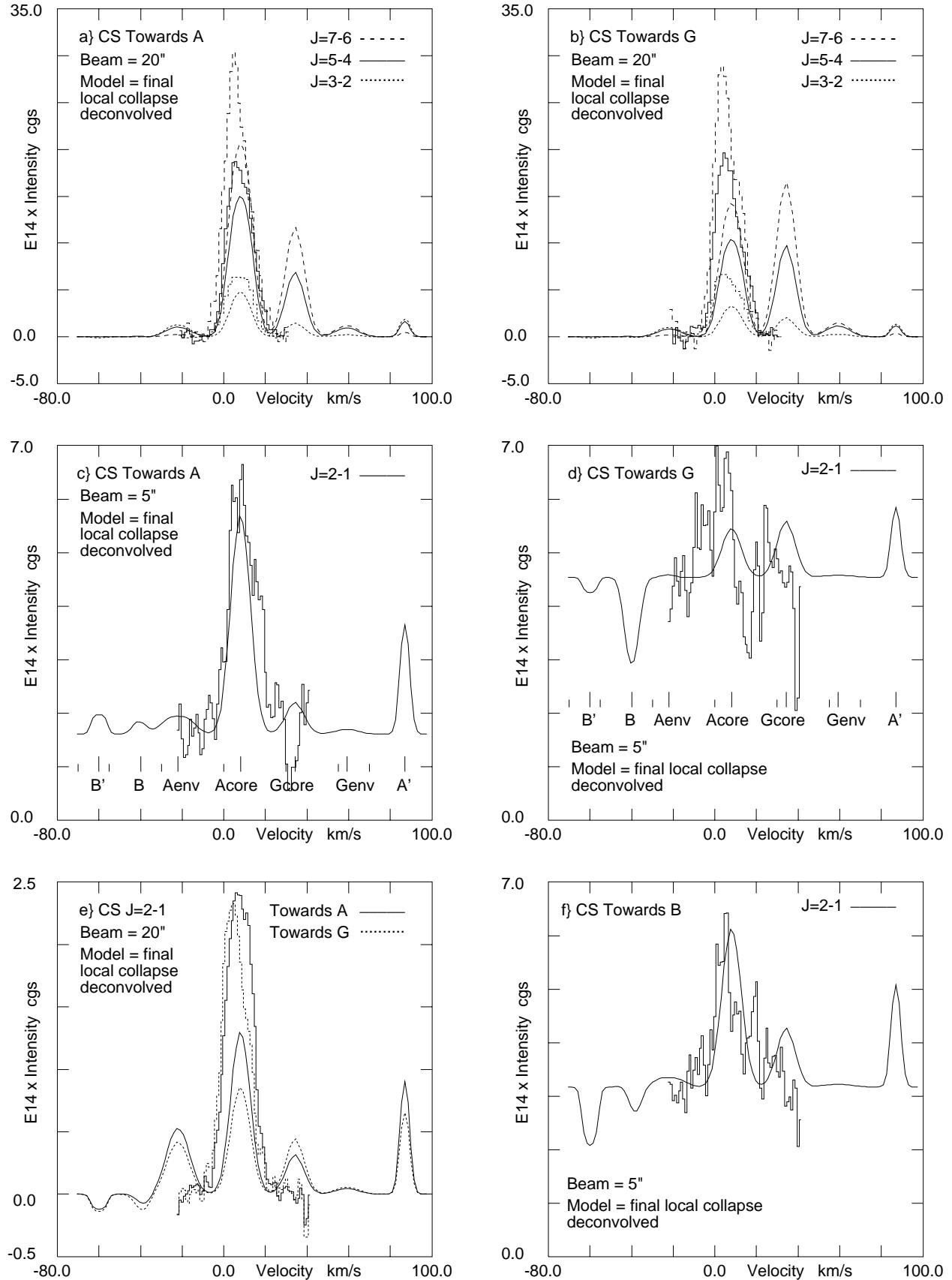


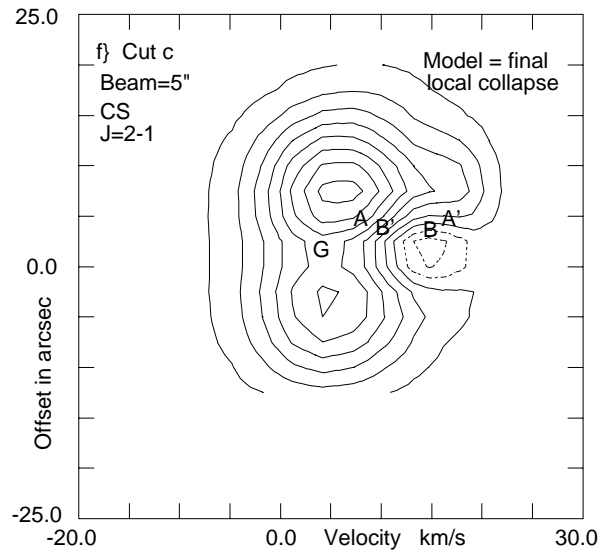
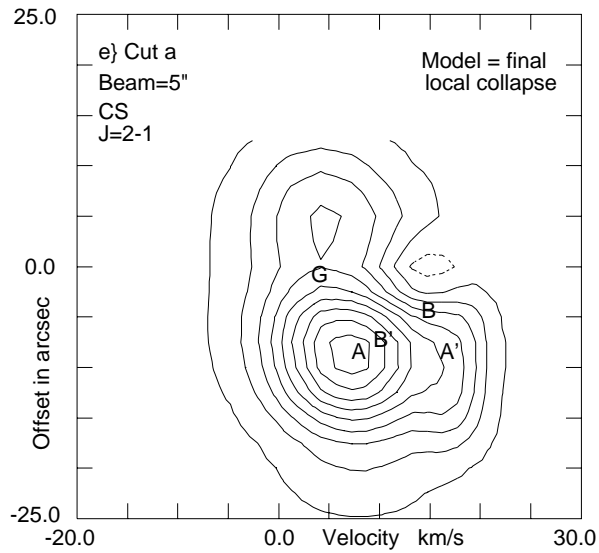
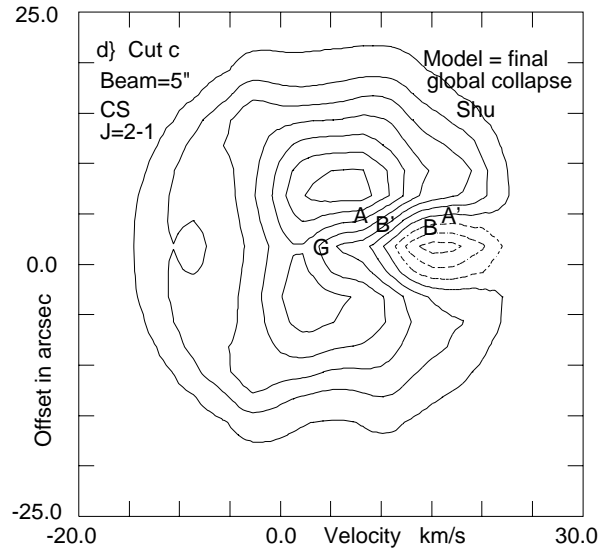
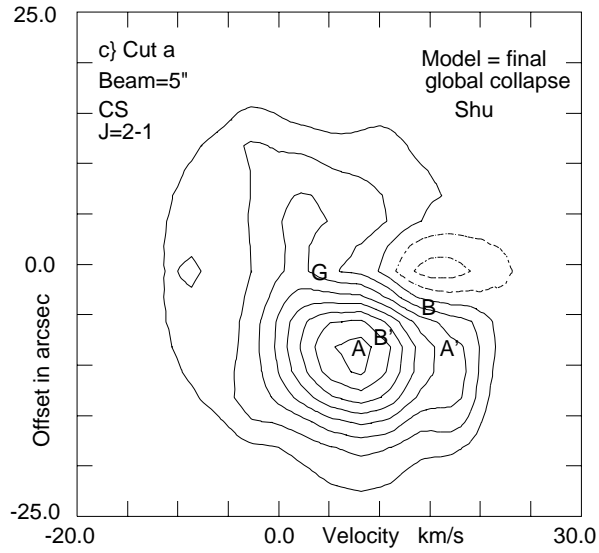
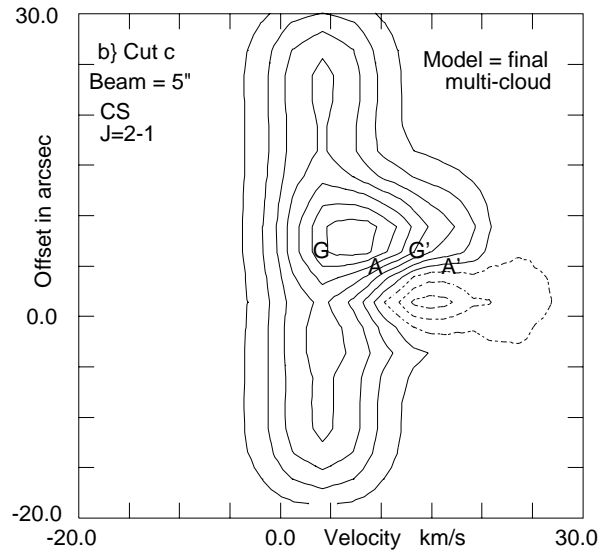
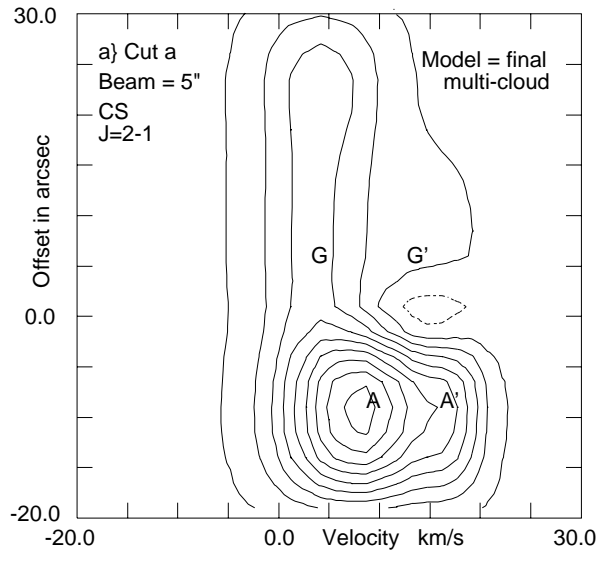
c} Shu Global collapse

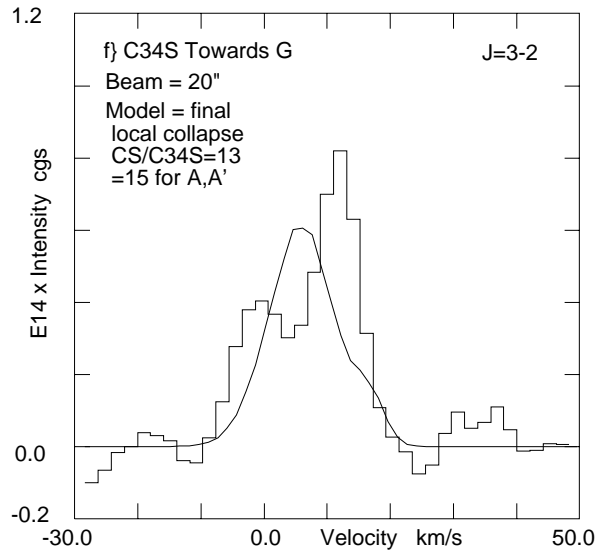
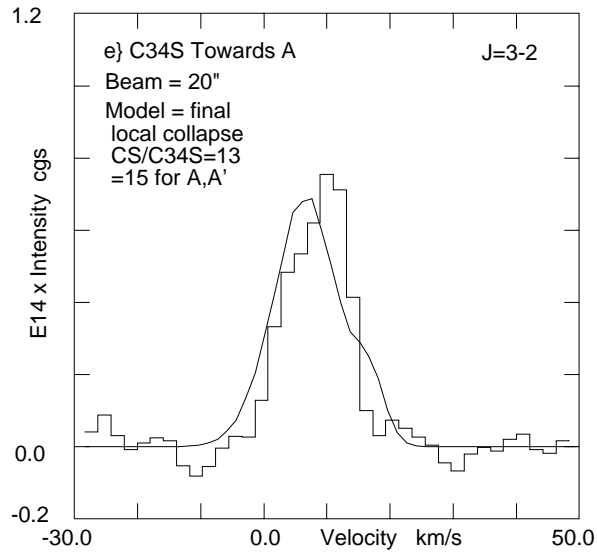
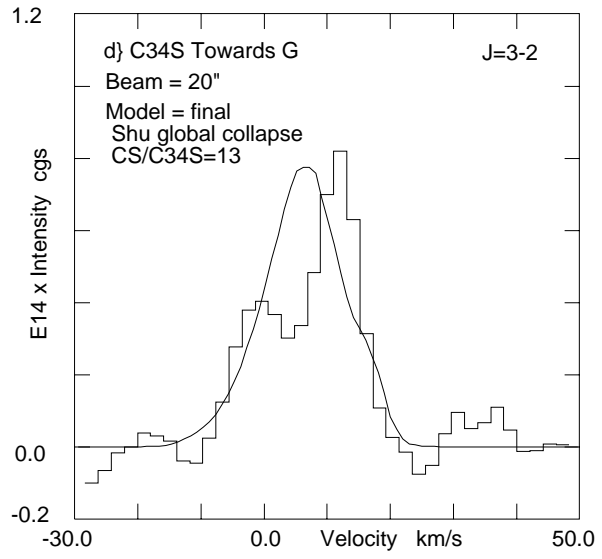
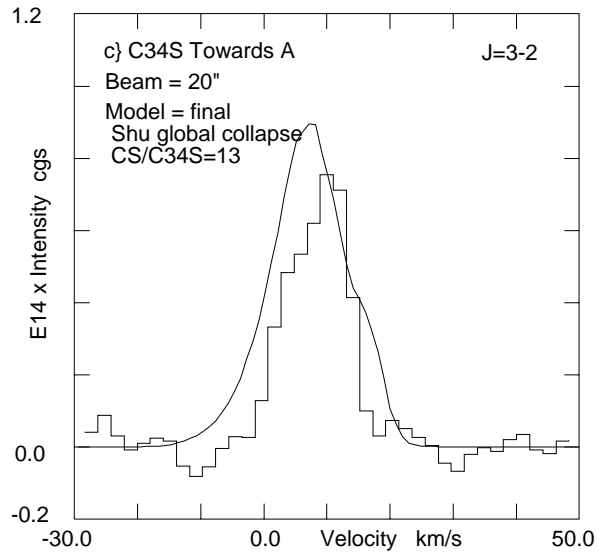
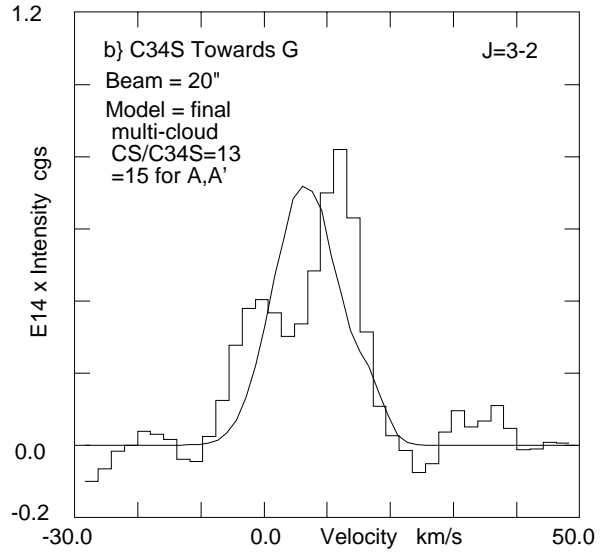
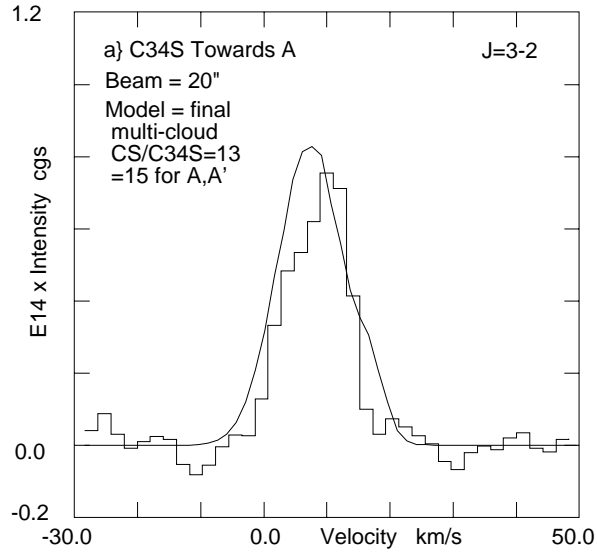


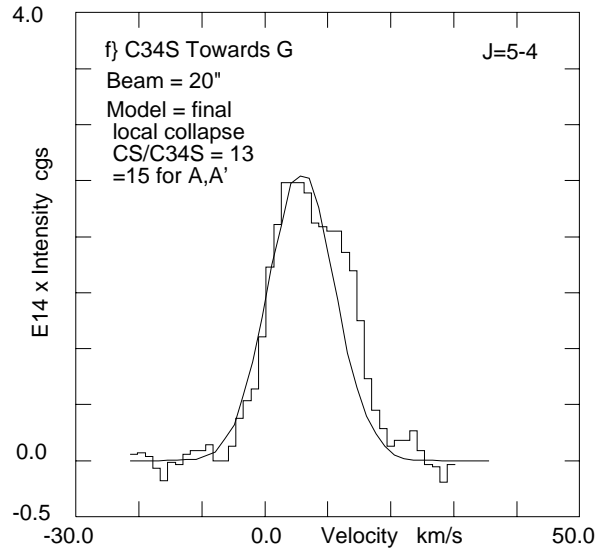
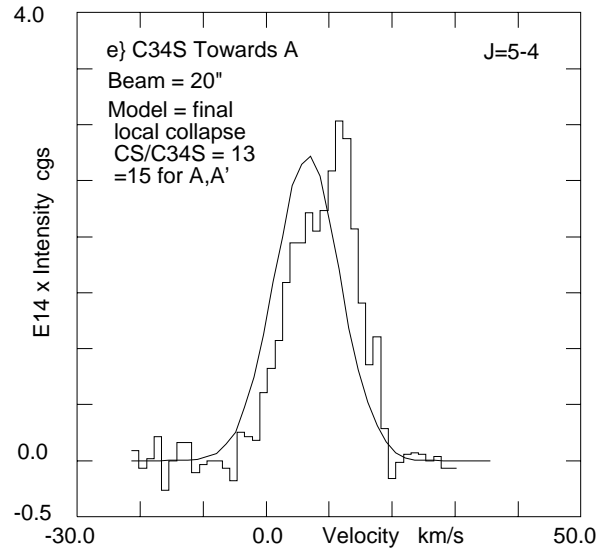
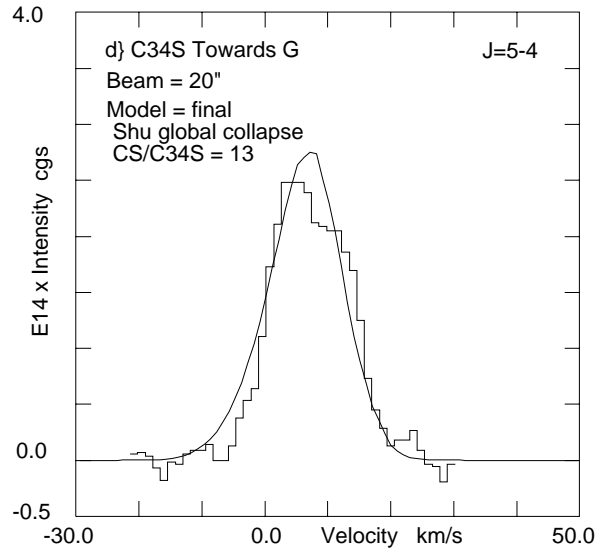
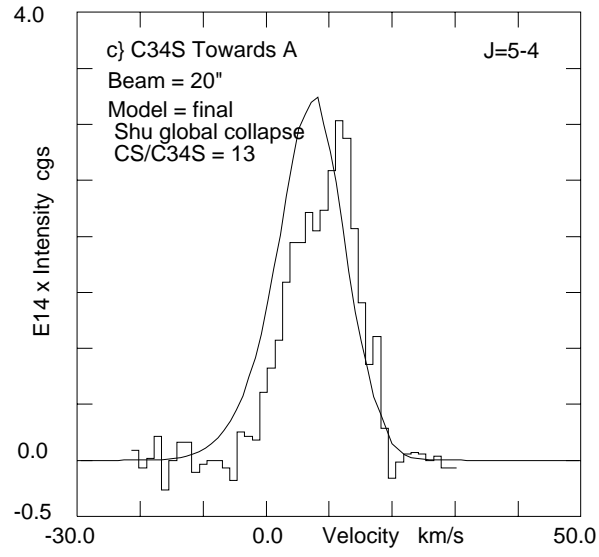
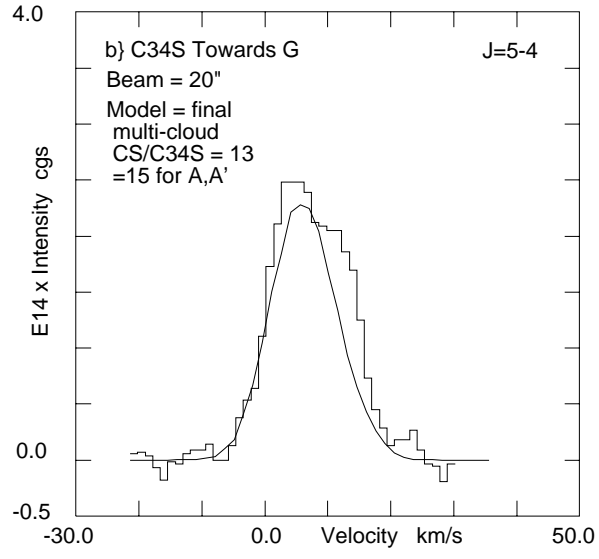
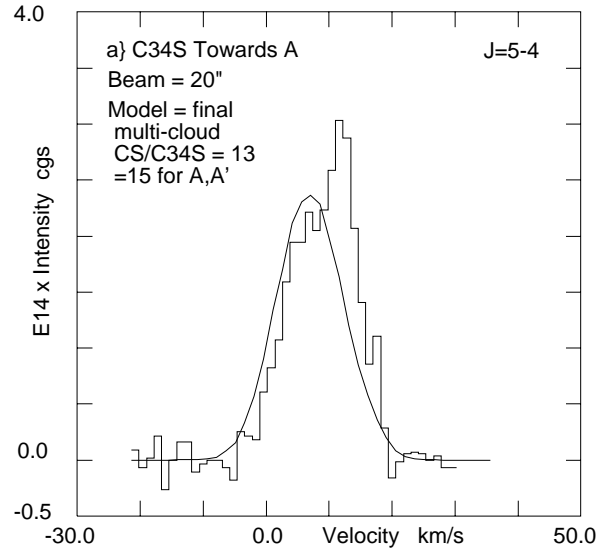


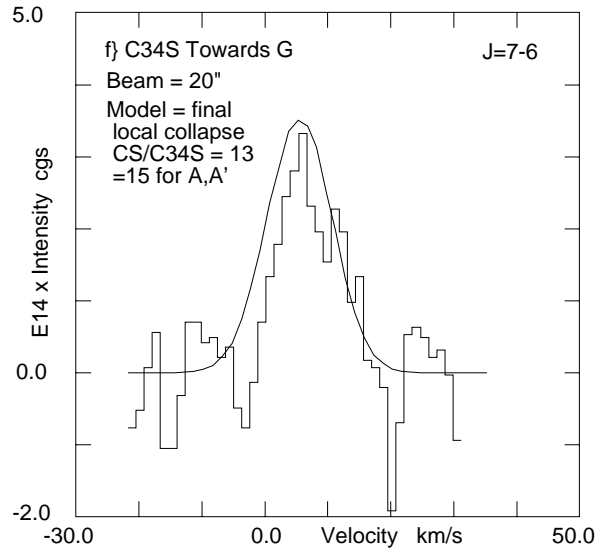
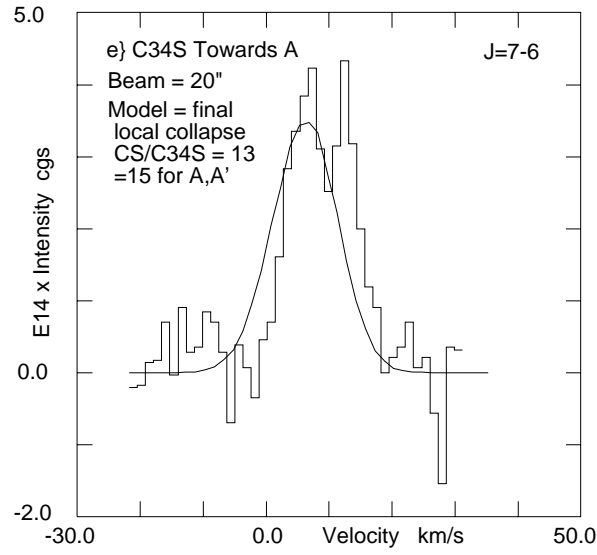
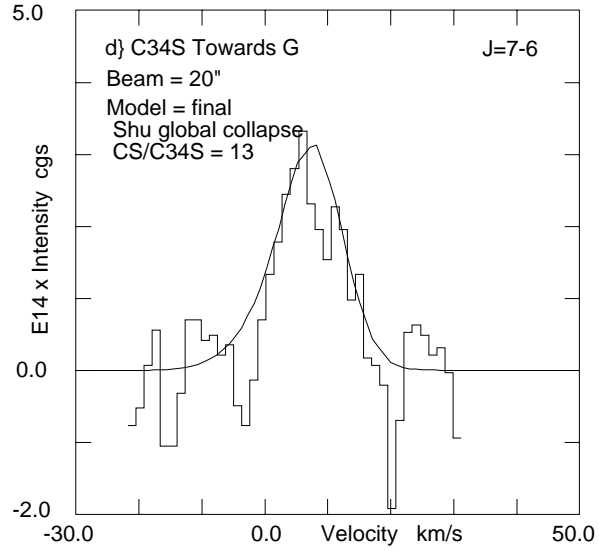
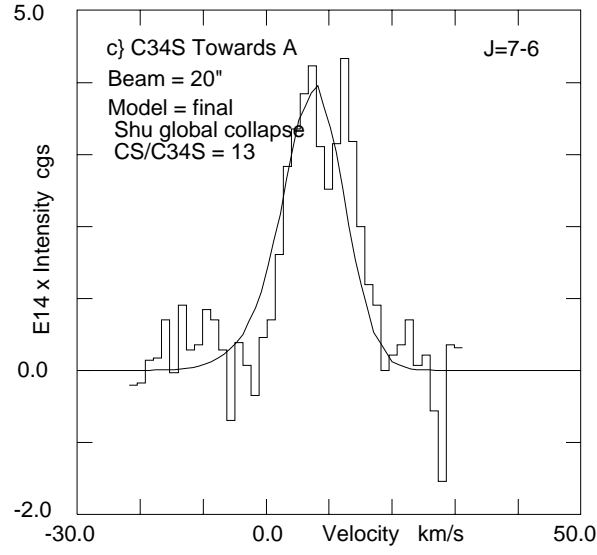
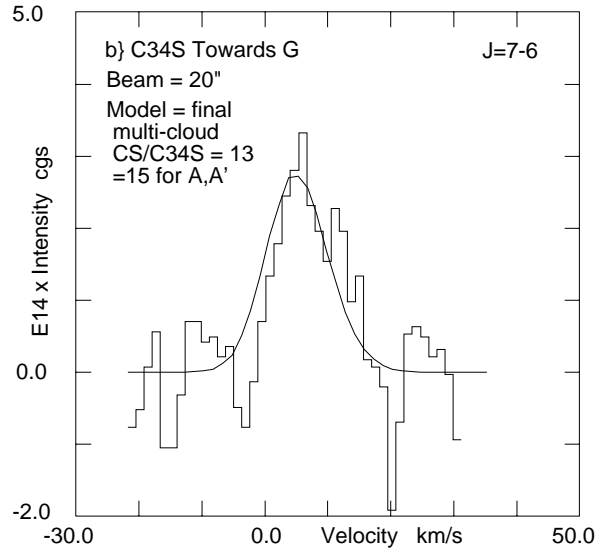
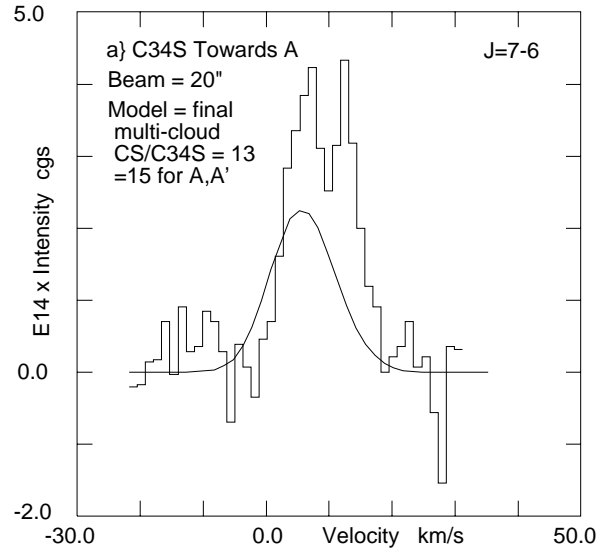


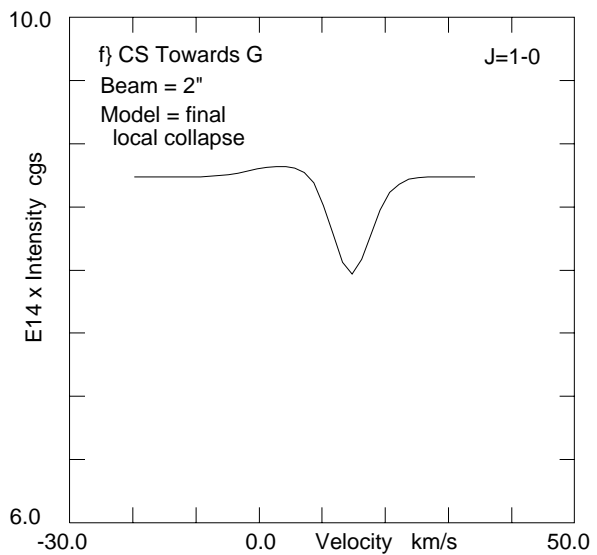
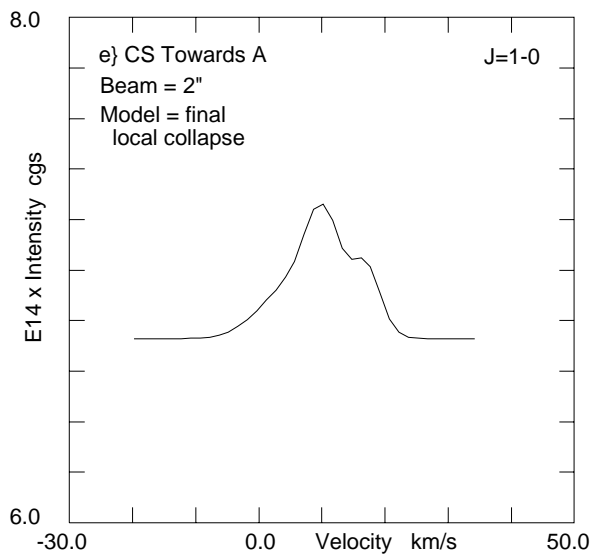
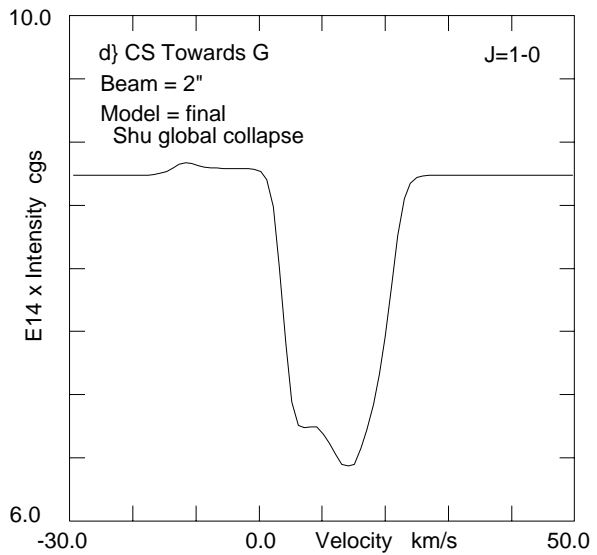
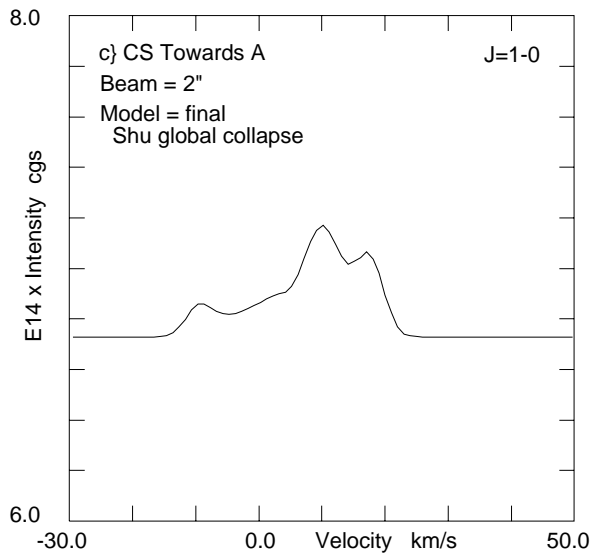
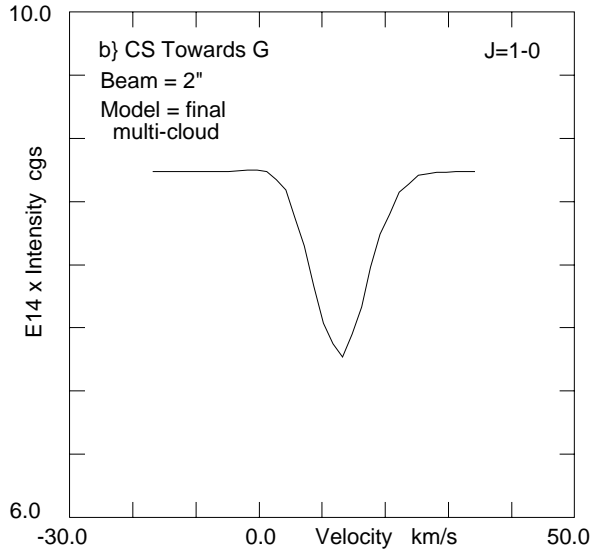
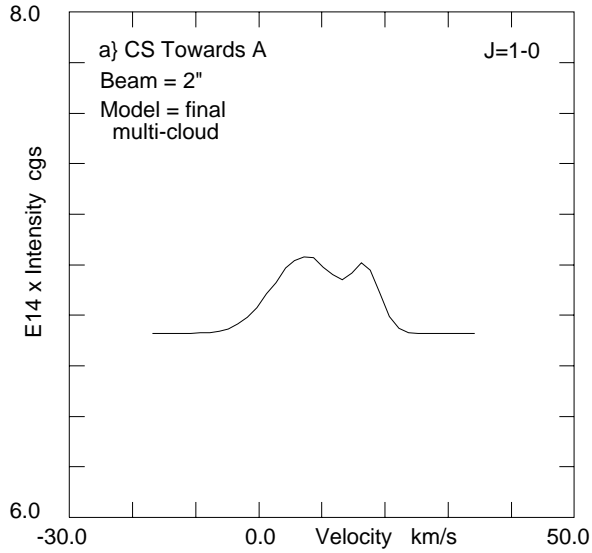


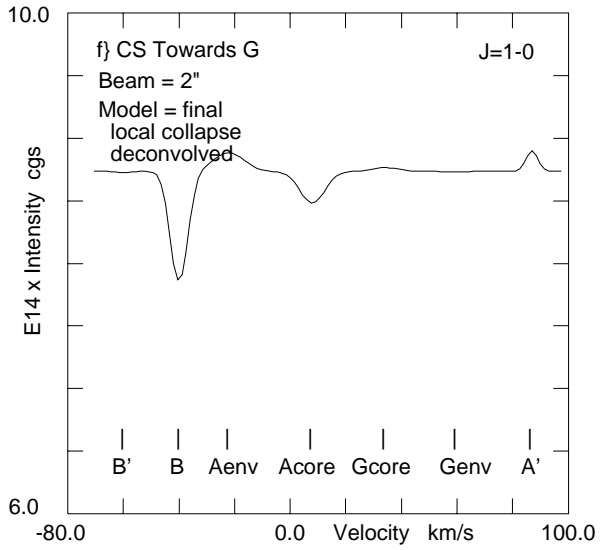
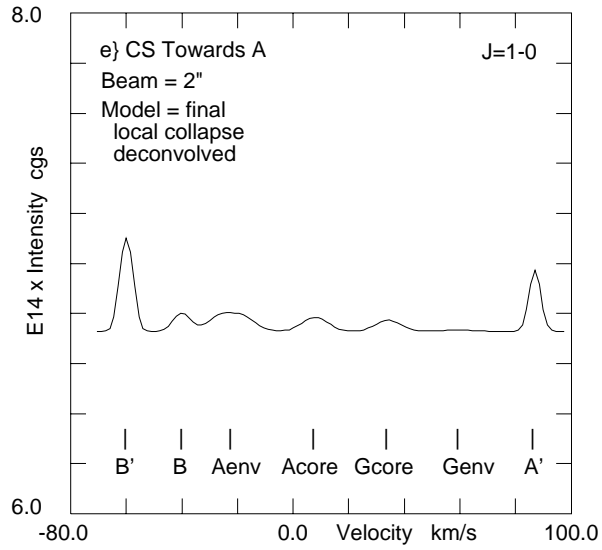
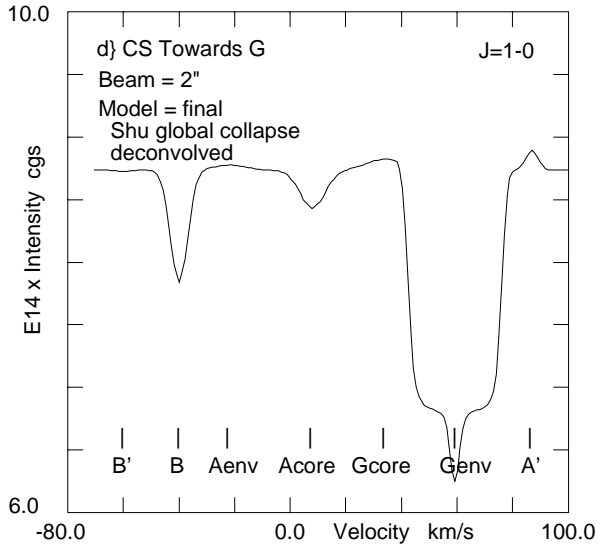
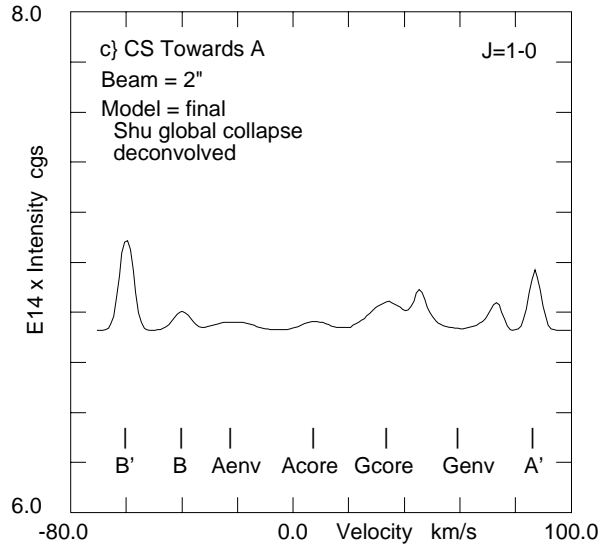
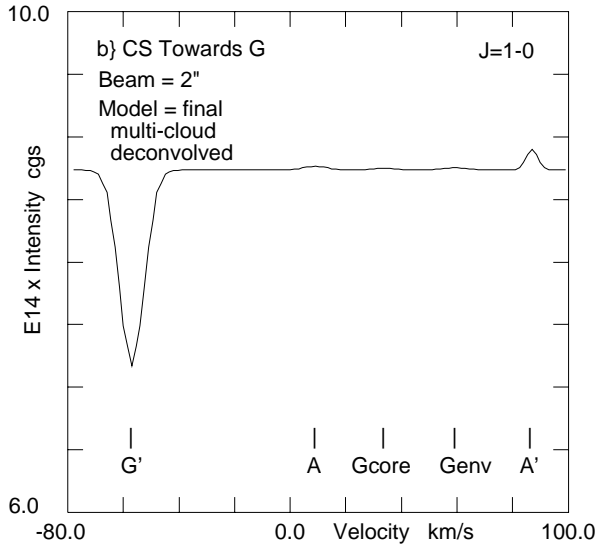
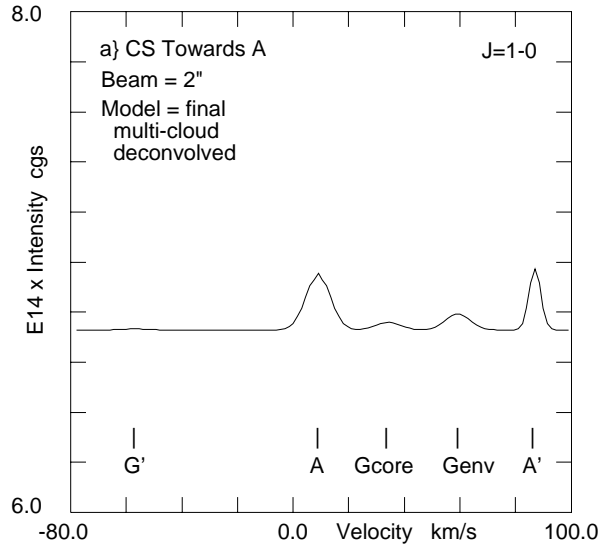


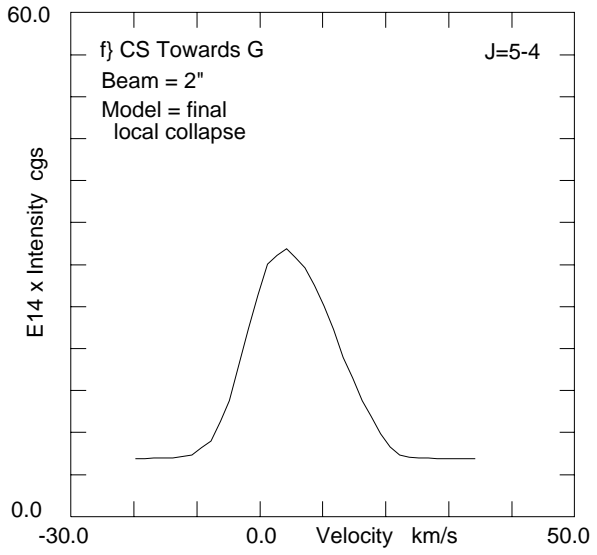
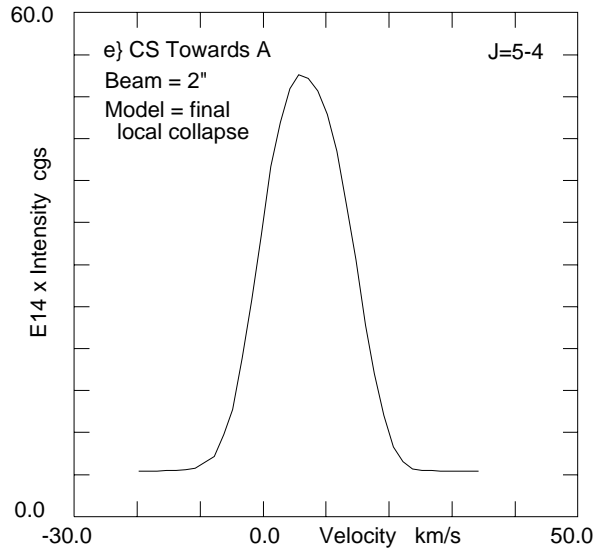
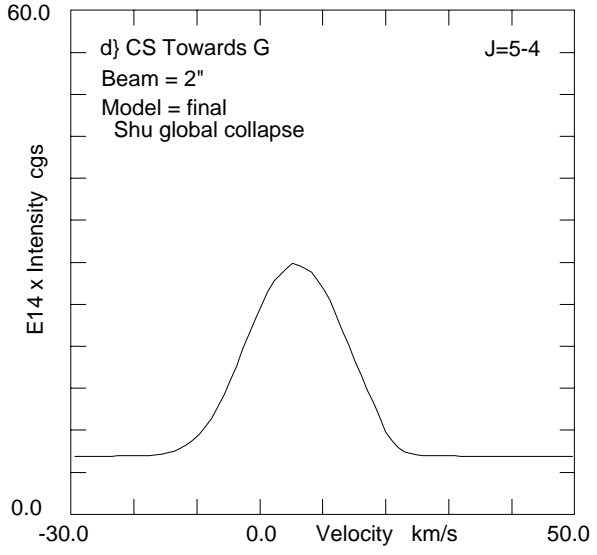
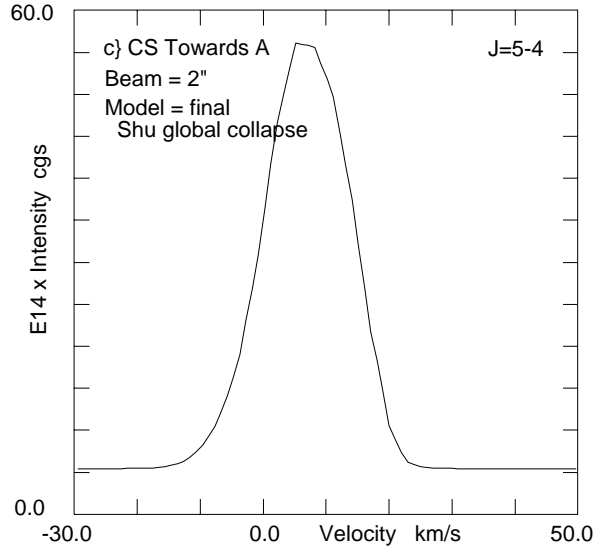
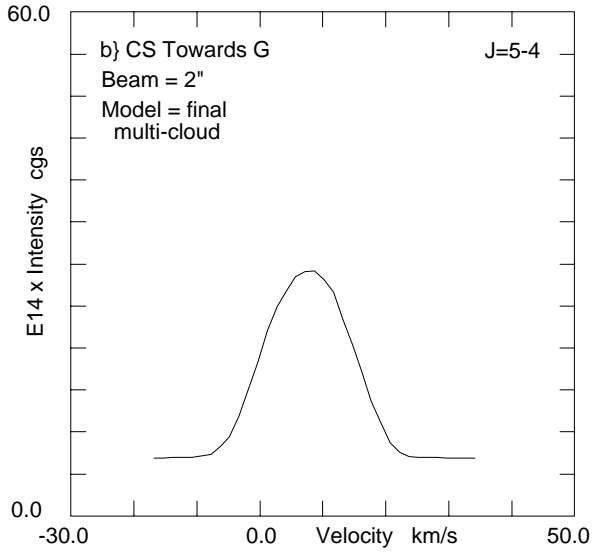
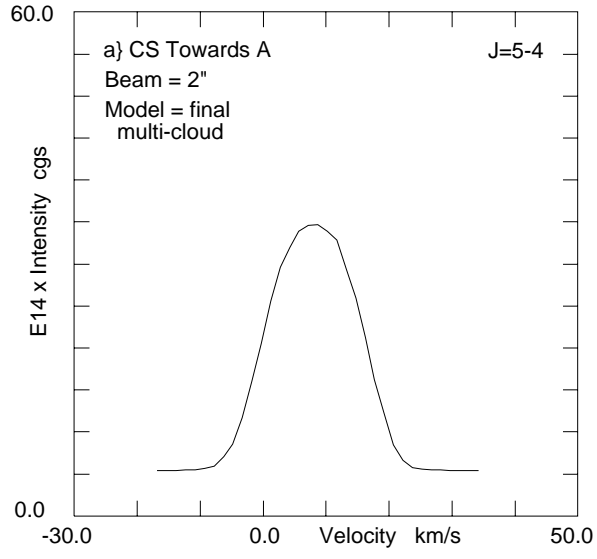


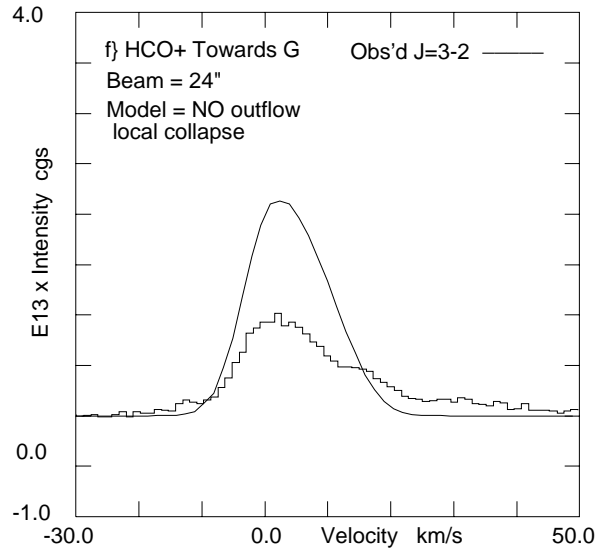
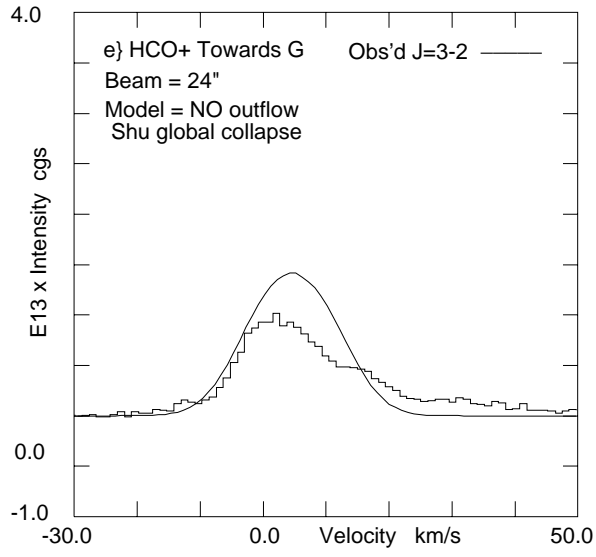
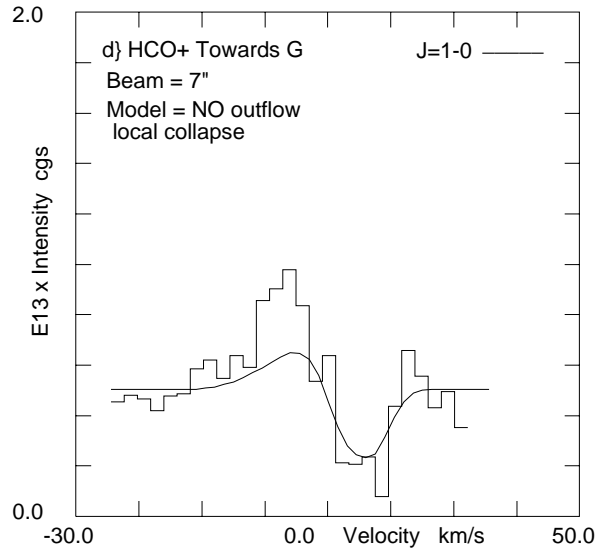
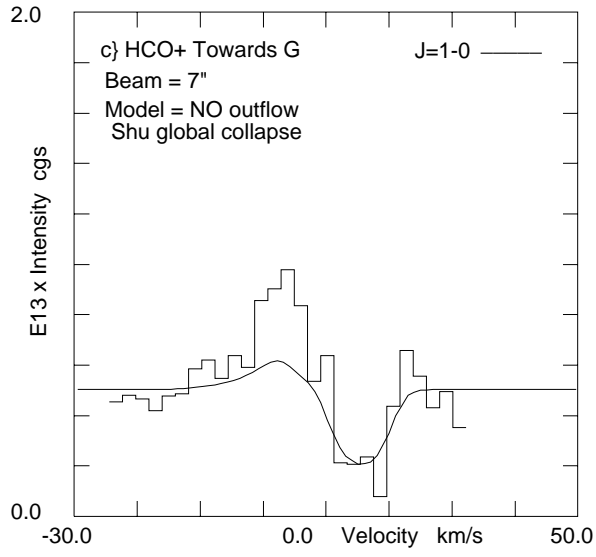
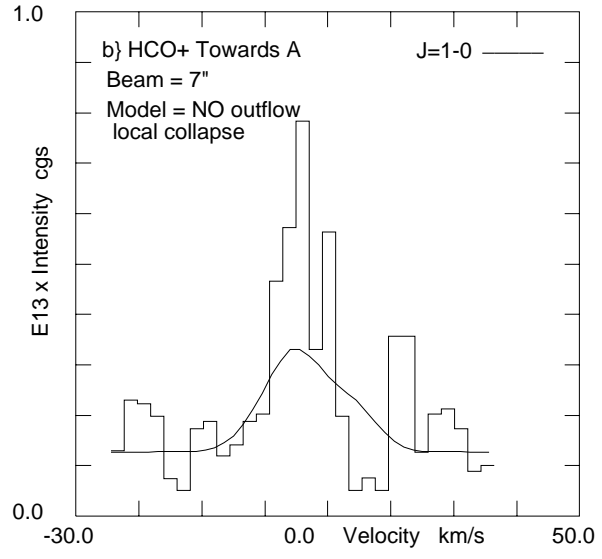
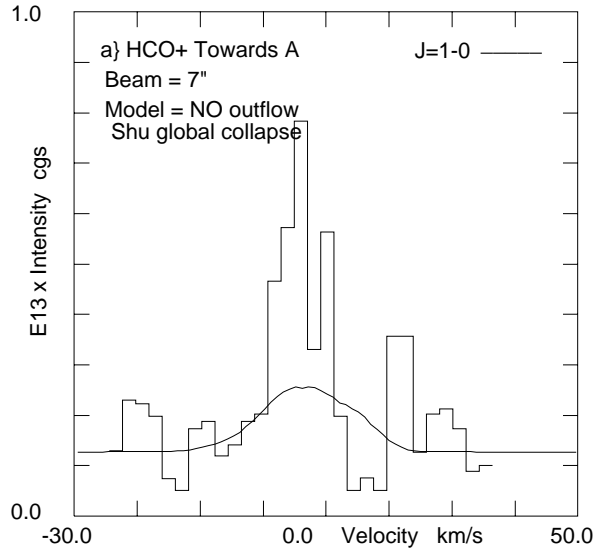


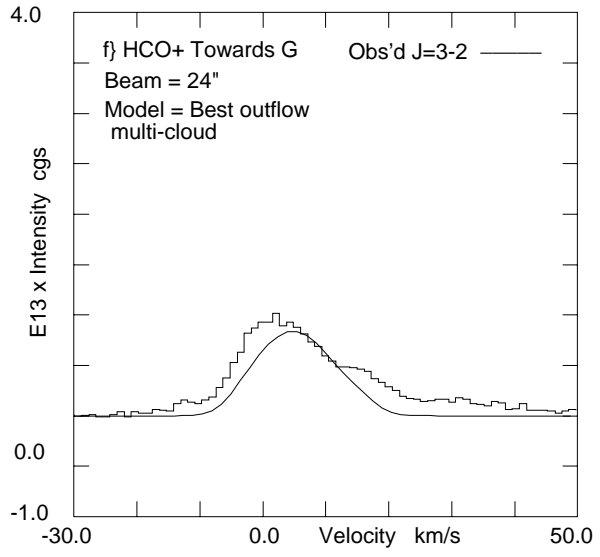
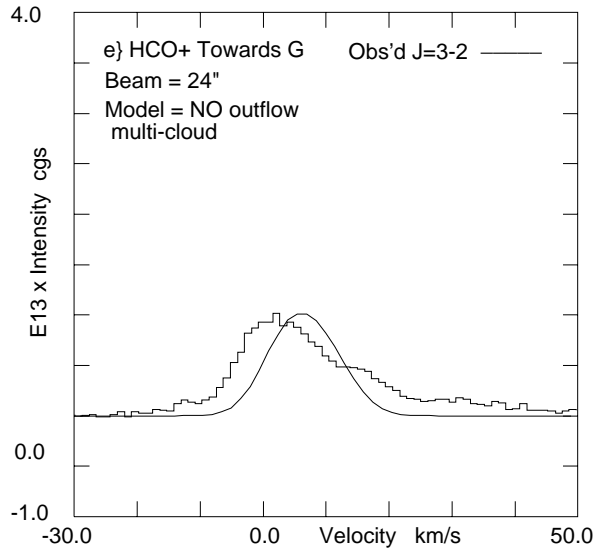
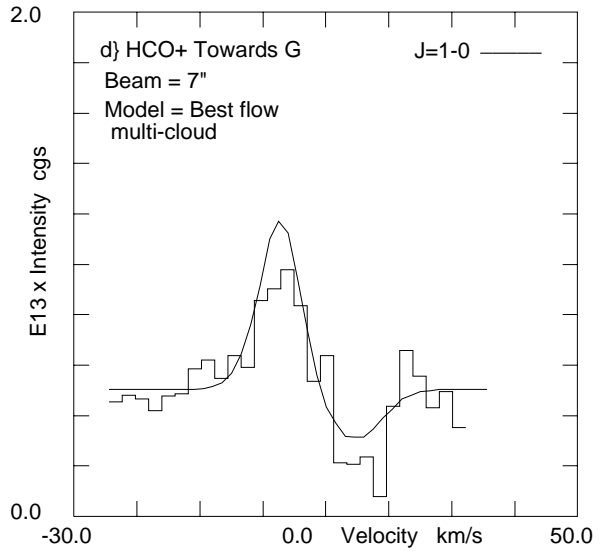
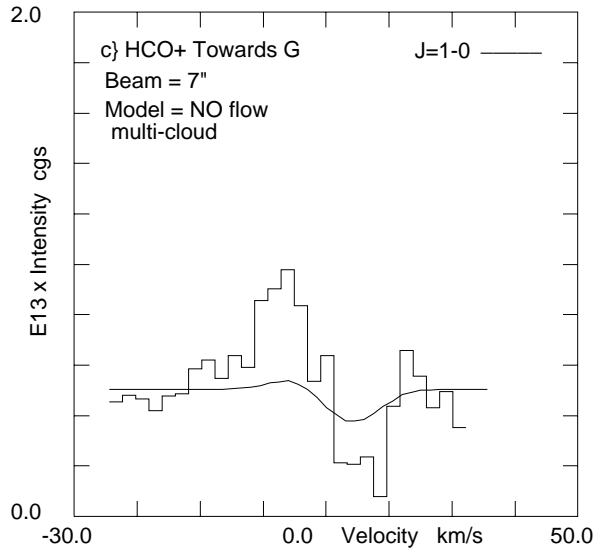
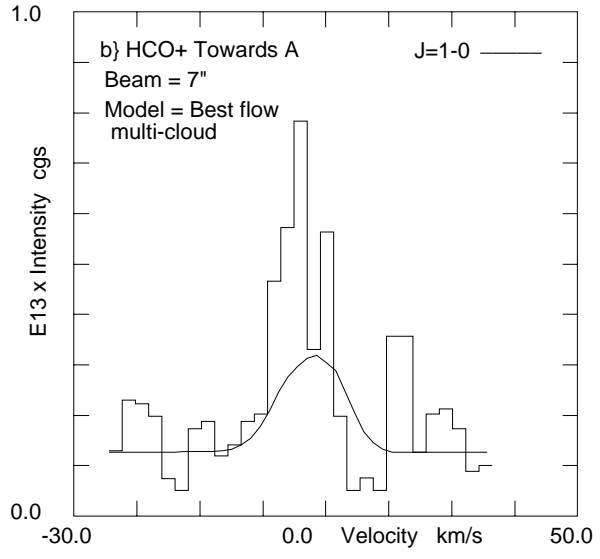
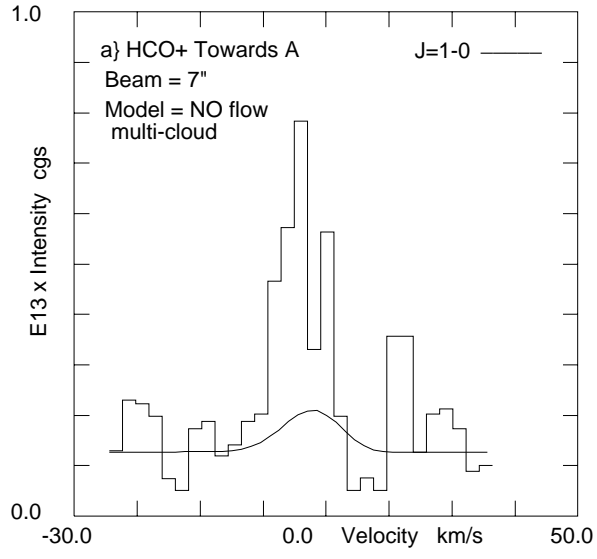


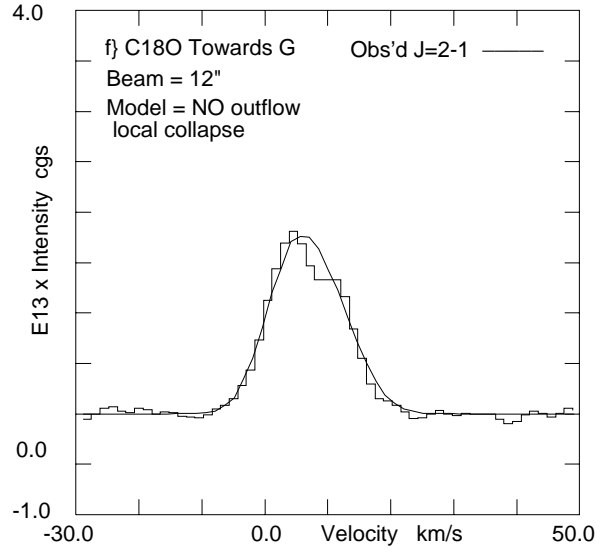
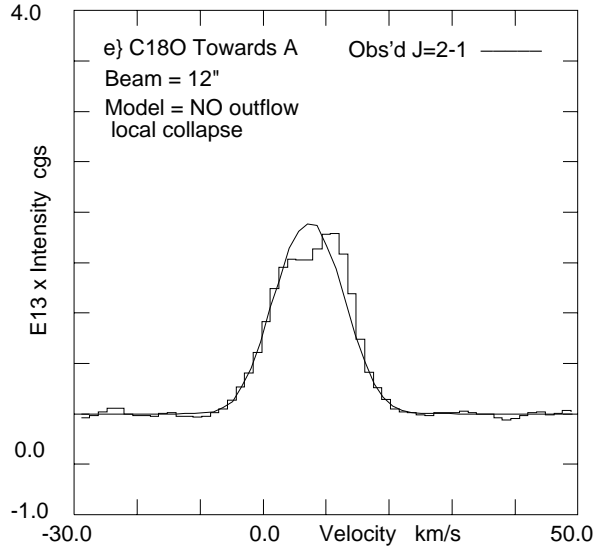
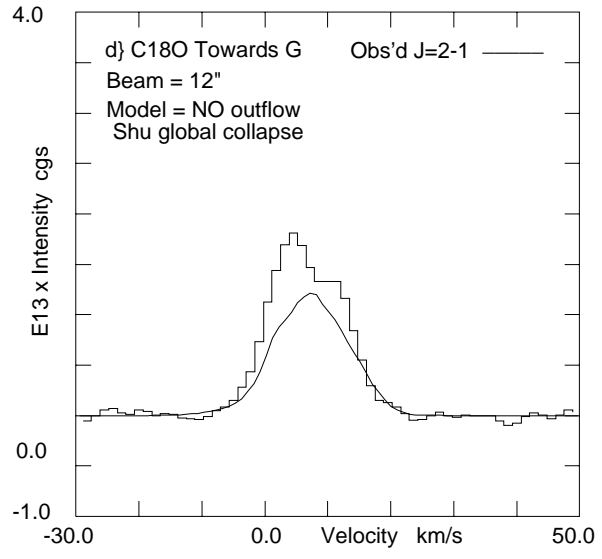
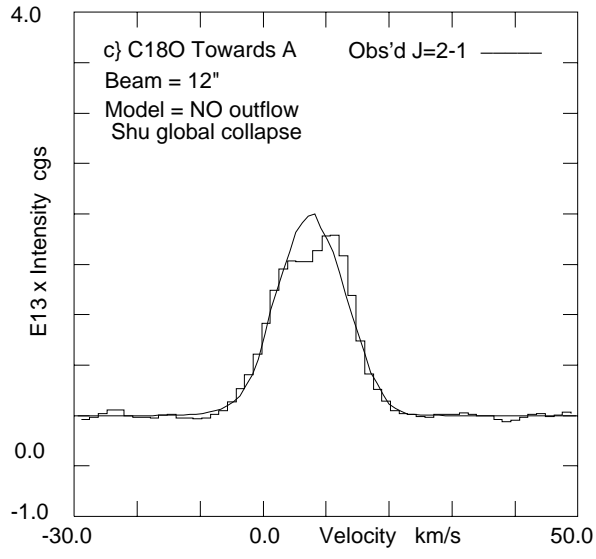
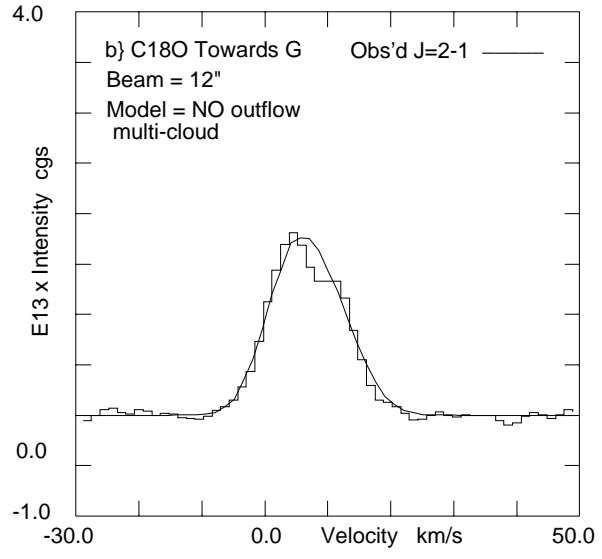
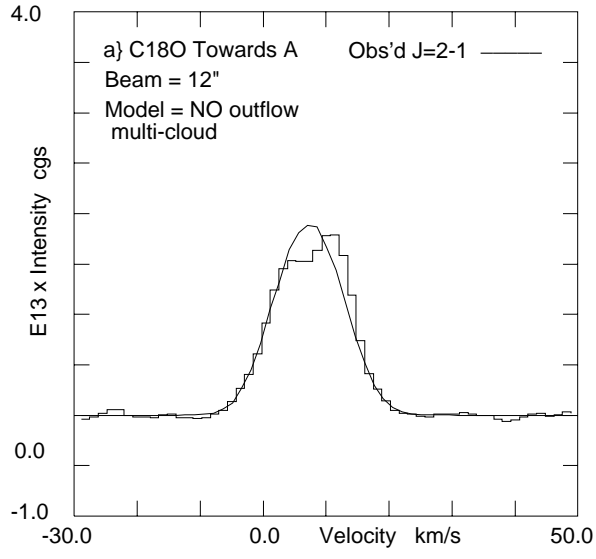


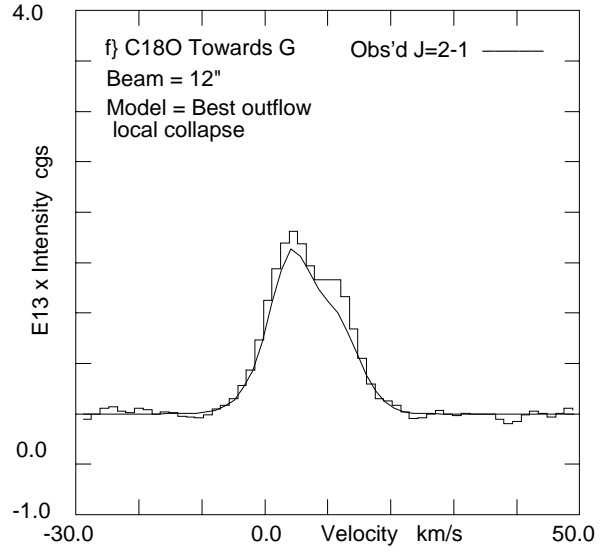
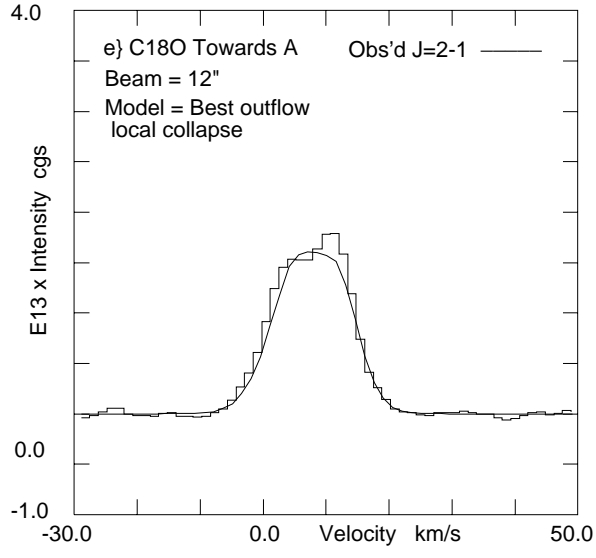
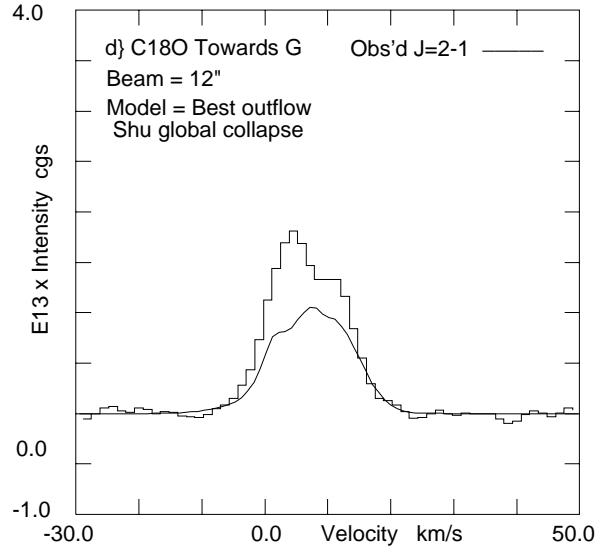
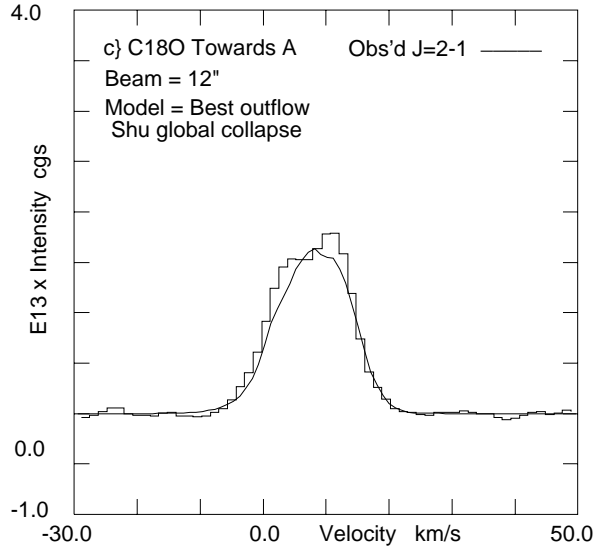
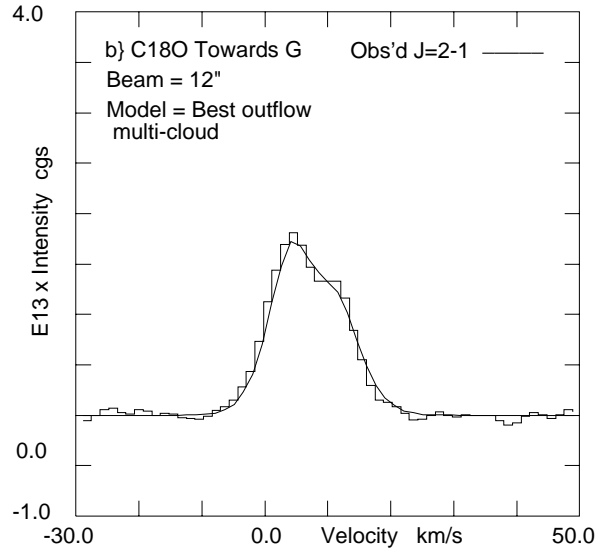
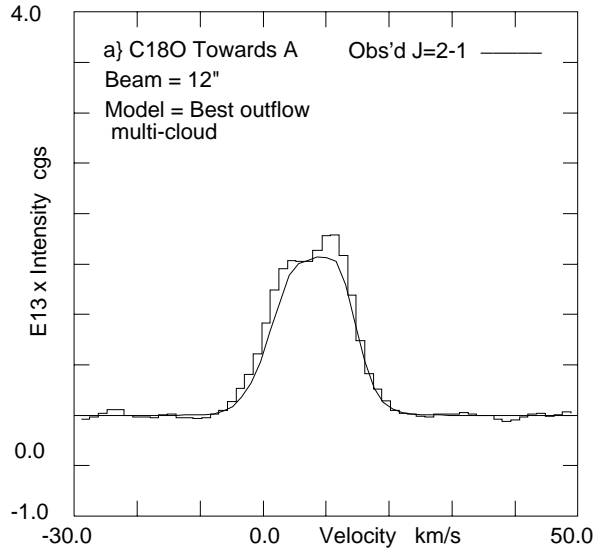












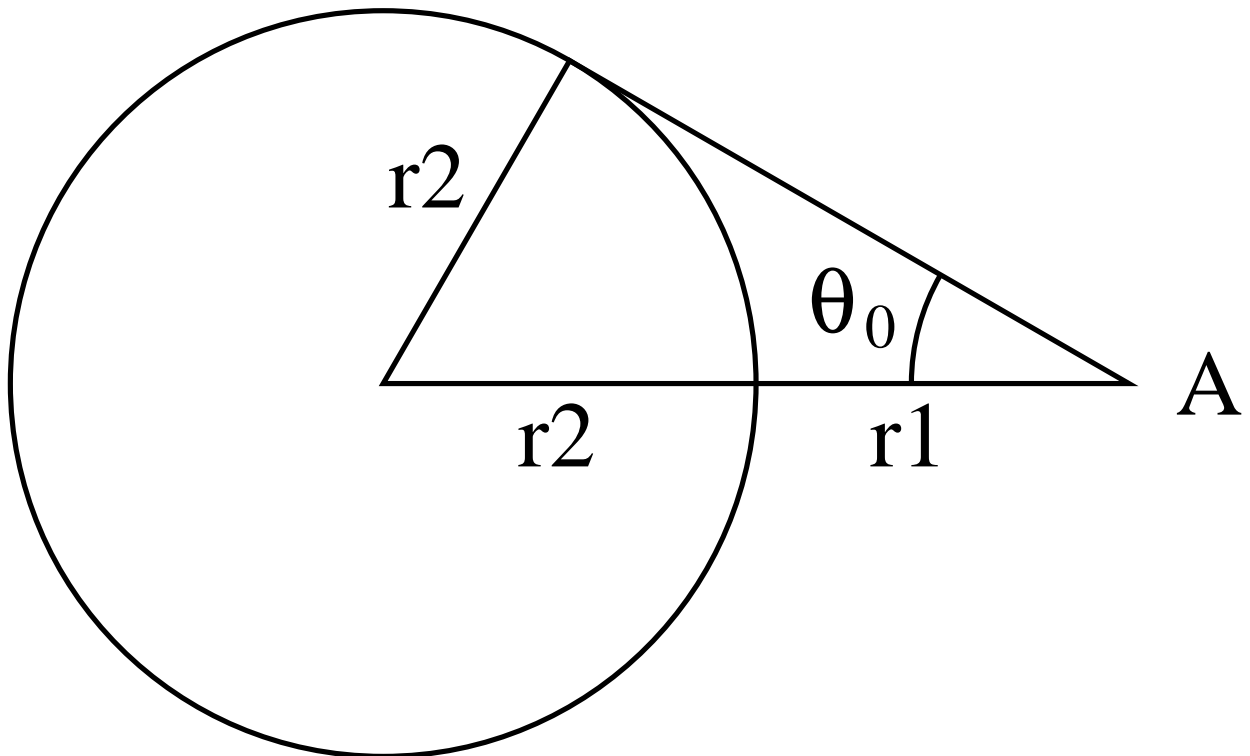


Table 1. Conversion Factor $C(\nu)$ between T_B (K) and $10^{14} I$ (cgs)

Species	Transitions			
	J=2-1	J=3-2	J=5-4	J=7-6
CS	3.39	1.51	0.543	0.277
$C^{34}S$	3.50	1.56	0.560	0.286

Table 2. Preliminary Multi-cloud Model

Parameter	A ^a	G'	G	B H II	G H II	A'
v_{lsr} (km s ⁻¹)	9.0	13.0	4.2	0.0 ^b	0.0 ^b	17.0
$r(\text{H II})$ (pc)	0.04	0.01 ^c	0.01 ^c	0.02	0.17	0.04 ^c
n_e (cm ⁻³)	8.6×10^4	0.10 ^c	0.10 ^c	2.0×10^5	2.2×10^4	0.10 ^c
T_e (K)	10^4	10^4	10^4	10^4	10^4	10^4
r_{max} (pc)	0.60	0.75	1.43	0.05	0.33	0.60
v (km s ⁻¹)	0.0	0.0	0.0	0.0	0.0	0.0
v_{turb} (km s ⁻¹)	6.0	6.0	6.0	4.2	4.2	3.0
T_k (K)	50.0	50.0	50.0	50.0	50.0	50.0
$n(\text{H}_2)$ (cm ⁻³)	1.3×10^6	2.0×10^4	1.2×10^6	2.0×10^4	2.0×10^6	2.0×10^5
$n(\text{CS})$ (cm ⁻³)	3.4×10^{-4}	3.2×10^{-5}	6.1×10^{-5}	1.0×10^{-7}	1.0×10^{-7}	5.2×10^{-5}
mass ($10^5 M_\odot$) ^d	0.8	0.0	10.2	0.0	0.2	0.1

^aH II region A is in the center of cloud A.

^bA value of zero is used for the LSR velocities of H II regions and the envelopes around them that do not contribute to the molecular intensities. These velocities are not meant to imply the actual velocities of the H II regions.

^cFor clouds without H II regions, very low values of $r(\text{H II})$ and n_e are used in the calculations since the rt program requires clouds to have H II regions in their centers.

^dThe total mass for this model is $11.3 \times 10^5 M_\odot$. The masses include contributions from helium assuming that the number of helium atoms is one-tenth the number of hydrogen atoms.

Table 3. Clouds in Common for the Final Models

Parameter ^b	B'	B ^a		A'
		coef	β	
v_{lsr} (km s ⁻¹)	10.0	15.0		17.0
$r(\text{H II})$ (pc)	0.01	0.02		0.04
n_e (cm ⁻³)	0.10	2.0×10^5		0.10
T_e (K)	10^4	10^4		10^4
r_{max} (pc)	0.22	0.48		0.60
v (km s ⁻¹)	0.0	-5.0	-0.5	0.0
v_{turb} (km s ⁻¹)	3.0	4.0	0.0	3.0
T_k (K)	50.0	100.0	-0.4	50.0
$n(\text{H}_2)$ (cm ⁻³)	2.0×10^4	1.0×10^6	-1.5	2.0×10^5
$n(\text{CS})$ (cm ⁻³)	3.2×10^{-4}	1.0×10^{-3}	-1.5	5.2×10^{-5}
mass ($10^5 M_\odot$)	0.0	0.0		0.1

^aH II region B is at the center of cloud B.

^bSome of the parameters have gradients in the form of power laws, where β is the exponent in coefficient $\times (r/r(\text{H II}))^\beta$. If β for the core is zero in core-envelope models, then the expression is coefficient $\times (r/r_{max})^\beta$, where r_{max} is the radius of the core.

Table 4. Final Multi-cloud Model^a

Parameter	A ^b	G'	G	G env	B H II	G H II
v_{lsr} (km s ⁻¹)	9.0	13.0	4.2		0.0 ^c	0.0 ^c
$r(\text{H II})$ (pc)	0.04	0.01 ^d	0.01 ^d		0.02	0.17
n_e (cm ⁻³)	8.6×10^4	0.10 ^d	0.10 ^d		2.0×10^5	2.2×10^4
T_e (K)	10^4	10^4	10^4		10^4	10^4
r_{max} (pc)	0.60	0.75	1.01	1.43	0.05	0.33
v (km s ⁻¹)	0.0	0.0	0.0	0.0	0.0	0.0
v_{turb} (km s ⁻¹)	6.0	6.0	6.0	6.0	4.2	4.2
T_k (K)	50.0	50.0	100.0	50.0	50.0	50.0
$n(\text{H}_2)$ (cm ⁻³)	1.3×10^6	2.0×10^4	6.0×10^6	1.2×10^6	2.0×10^4	2.0×10^6
$n(\text{CS})$ (cm ⁻³)	3.4×10^{-4}	3.2×10^{-5}	6.1×10^{-5}	6.1×10^{-5}	1.0×10^{-7}	1.0×10^{-7}
mass ($10^5 M_\odot$) ^e	0.8	0.0	17.9	6.6	0.0	0.2

^aIn addition to the clouds in this table, the final multi-cloud model includes cloud A' from Table 3 after cloud G H II.

^bH II region A is in the center of cloud A.

^cA value of zero is used for the LSR velocities of H II regions and the envelopes around them that do not contribute to the molecular intensities. These velocities are not meant to imply the actual velocities of the H II regions.

^dFor clouds without H II regions, very low values of $r(\text{H II})$ and n_e are used in the calculations since the rt program requires clouds to have H II regions in their centers.

^eThe total mass for this model is $25.6 \times 10^5 M_\odot$. The masses include contributions from helium assuming that the number of helium atoms is one-tenth the number of hydrogen atoms.

Table 5. Final Global Collapse Model ^a

Parameter ^c	A core ^b		A env		G core ^b		G env	
	coef	β	coef	β	coef	β	coef	β
v_{lsr} (km s ⁻¹)	8.0				4.2			
$r(\text{H II})$ (pc)	0.04				0.17			
n_e (cm ⁻³)	8.6×10^4				2.2×10^4			
T_e (K)	10^4				10^4			
r_{max} (pc)	0.48		0.96		0.81		4.97	
v (km s ⁻¹)	0.0	0.0	-5.0	-0.5	0.0	0.0	-22.5	-0.5
v_{turb} (km s ⁻¹)	6.0	0.0	6.0	0.0	9.0	0.0	2.0	0.0
T_k (K)	100.0	-0.4	100.0	-0.4	100.0	-0.4	100.0	-0.4
$n(\text{H}_2)$ (cm ⁻³)	8.0×10^6	0.0	8.0×10^5	-1.5	1.5×10^6	0.0	1.5×10^3	-1.5
$n(\text{CS})$ (cm ⁻³)	7.0×10^{-4}	0.0	7.0×10^{-5}	-1.5	1.6×10^{-4}	0.0	1.6×10^{-5}	-1.5
mass ($10^5 M_\odot$) ^d	2.6		0.9		2.3		0.0	

^aIn addition to the clouds in this table, the final global collapse model includes clouds B', B, and A' from Table 3. Clouds B' and B are between clouds A and G, and cloud A' is behind cloud G.

^bH II region A is in the center of cloud A, and H II region G is in the center of cloud G.

^cSome of the parameters have gradients in the form of power laws, where β is the exponent in coefficient $\times (r/r(\text{H II}))^\beta$. If β for the core is zero in core-envelope models, then the expression is coefficient $\times (r/r_{max})^\beta$, where r_{max} is the radius of the core.

^dThe total mass for this model is $5.9 \times 10^5 M_\odot$. The masses include contributions from helium assuming that the number of helium atoms is one-tenth the number of hydrogen atoms.

Table 6. Final Local Collapse Model ^a

Parameter ^c	A core ^b		A env		G core ^b		G env	
	coef	β	coef	β	coef	β	coef	β
v_{lsr} (km s ⁻¹)	8.0				4.2			
$r(\text{H II})$ (pc)	0.04				0.17			
n_e (cm ⁻³)	8.6×10^4				2.2×10^4			
T_e (K)	10^4				10^4			
r_{max} (pc)	0.48		0.96		0.52		0.79	
v (km s ⁻¹)	0.0	0.0	-5.0	-0.5	0.0	0.0	-5.0	-0.5
v_{turb} (km s ⁻¹)	6.0	0.0	6.0	0.0	6.0	0.0	6.0	0.0
T_k (K)	100.0	-0.4	100.0	-0.4	100.0	-0.4	100.0	-0.4
$n(\text{H}_2)$ (cm ⁻³)	5.0×10^6	0.0	5.0×10^5	-1.5	5.0×10^6	0.0	5.0×10^6	-1.5
$n(\text{CS})$ (cm ⁻³)	6.0×10^{-4}	0.0	6.0×10^{-5}	-1.5	1.8×10^{-4}	0.0	1.8×10^{-4}	-1.5
mass ($10^5 M_\odot$) ^d	1.6		0.6		2.0		3.5	

^aIn addition to the clouds in this table, the final local collapse model includes clouds B', B, and A' from Table 3. Clouds B' and B are between clouds A and G, and cloud A' is behind cloud G.

^bH II region A is in the center of cloud A, and H II region G is in the center of cloud G.

^cSome of the parameters have gradients in the form of power laws, where β is the exponent in coefficient $\times (r/r(\text{H II}))^\beta$. If β for the core is zero in core-envelope models, then the expression is coefficient $\times (r/r_{max})^\beta$, where r_{max} is the radius of the core.

^dThe total mass for this model is $7.8 \times 10^5 M_\odot$. The masses include contributions from helium assuming that the number of helium atoms is one-tenth the number of hydrogen atoms.

Table 7. The RMS Differences Between Model Profiles and Observed Profiles

Region	Resolution	Transition	σ_{base}^a	Pre-M-C ^b $\sigma_{line}/\sigma_{base}$	Multi-Cloud $\sigma_{line}/\sigma_{base}$	Global Collapse $\sigma_{line}/\sigma_{base}$	Local Collapse $\sigma_{line}/\sigma_{base}$
A	5	2-1	4.1	1.0	1.2	1.6	1.4
G	5	2-1	4.1	1.5	1.7	1.7	1.5
B	5	2-1	4.1	1.9	2.0	1.7	1.5
A	20	2-1	0.8	3.4	4.1	4.4	6.1
G	20	2-1	0.8	3.2	5.3	4.3	6.5
A	20	3-2	1.2	9.3	7.5	6.9	5.3
G	20	3-2	1.2	5.6	4.3	4.8	7.3
A	20	5-4	6.5	2.0	3.2	4.5	3.7
G	20	5-4	6.5	1.9	3.4	4.1	3.1
A	20	7-6	11	7.1	2.4	3.3	2.5
G	20	7-6	11	7.6	2.7	3.4	3.7
average				4.0	3.4	3.7	3.9

Note. — All σ values are times 10^{-15} erg s $^{-1}$ cm $^{-2}$ Hz $^{-1}$ sr $^{-1}$

^arms variations of the observations of the line-free baseline or continuum.

^bPreliminary Multi-Cloud Model

Table 8. Percent of the Celestial Sphere Covered

r^a	θ (radians)	θ (degrees)	Percent of Celestial Sphere Covered by External Cloud
0	0	0	0
0.1	0.091	5.2	0.2
0.5	0.340	19.5	2.9
1.0	0.524	30.0	6.7
2.0	0.730	41.8	12.7
10.0	1.141	65.4	29.2
∞	1.571	90.0	50.0

^a $r = r_2/r_1$ where r_1 is the distance from a point within one cloud to the outer edge of a second, external cloud whose radius is r_2 . (See Figure 27).